8 Mountings and Interfaces

D. F. Gluck* and V. Baturkin†

Introduction

This chapter deals with the thermal design, analysis, and performance of a wide variety of spacecraft mechanical interfaces, as well as thermal predictive methods for use with those interfaces. Heat removal from electronic units is a foremost spacecraft concern, and thus the problem of developing an optimal conductive interface between unit baseplate and spacecraft mounting is critical. The elements of this very difficult problem must be addressed sequentially at increasingly higher levels of complexity: the engineer needs to consider the effects of uniform pressure between plates in vacuum, the use of bolts or screws to join plates, the effects of fluid in the gap between plates, and the use of interface fillers. The interface problem is compounded by structural and thermal hardware, including honeycomb mounting panels, heat pipes, and thermal doublers. For problems such as this, combined thermal and structural analysis is an important design and evaluation tool. Some thermal interfaces must be compliant rather than rigid; others must reduce and minimize rather than enhance heat transfer. Still others involve composite or polymer materials. In addition, some interfaces must transfer heat across mobile bearings. All of these issues are addressed in this chapter, with the object of providing practical design and analysis aids, performance predictions, and guidance to the practicing spacecraft thermal engineer. Chapter 16 contains a more detailed discussion of the theoretical models of thermal contact resistance and supporting experimental work.

Unit Conduction Cooling

Unit Mounting

In most cases, an electronic unit is designed so that the power dissipated within it is transported as heat to the unit's mounting surface (baseplate). This heat is transferred by conduction to a section of the spacecraft structure (here called the mounting plate) and thence by a variety of methods and paths to the space sink. A smaller number of units are cooled partially (sometimes largely) by radiation. Such units are designed so that heat can be radiated from various unit surfaces, but usually not the mounting surface, to the surrounding space-vehicle enclosure or directly to space. The spacecraft's mounting plate is dealt with here, as is the predominant heat-transport method, conduction cooling from the unit's baseplate to the spacecraft's mounting plate.

The temperature rise across the mounting interface should be small; this requirement is important, because each part and device within the unit is subject to this

*DFG Engineering, Albuquerque, New Mexico.
†National Technical University of Ukraine (formerly Kyiv Polytechnic Institute), Kyiv, Ukraine.

temperature rise. Reliability and, possibly, functional performance are adversely affected by high temperature.

Most space-vehicle electronics boxes have baseplates ranging in size from 100 by 150 mm to 450 by 600 mm, with power levels sometimes exceeding 1000 W. Mounting is typically done by bolts set in a pattern along the baseplate perimeter, as shown schematically in Fig. 8.1. Flange mounting is convenient, because it makes bolts or screws accessible and enables the application of torque from above. When electronics boxes are built up from "slices" or modules (Fig. 8.2), the bolts are arranged along two opposed sides of the baseplate. Where power dissipation or local power per unit area is large, additional screws in the inboard regions of the unit are used. These secure from below, extending from the spacecraft mounting plate to the unit baseplate (Figs. 8.3 and 8.4). Because these screws must be inserted from below, their use complicates the assembly process. However, they increase the conductance from baseplate to mounting surface.

Conductance for Surfaces under Uniform Pressure

Possible modes of heat transfer from the unit baseplate to the space-vehicle mounting surface are convection, radiation, and conduction. However, because of the vacuum condition of space, essentially no convection occurs at the interface.

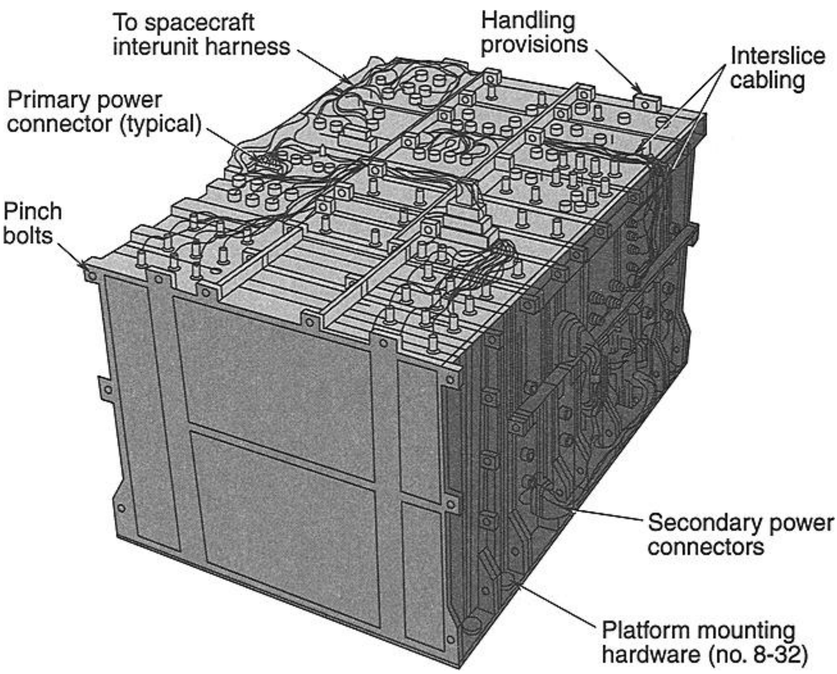

Fig. 8.1. Mounting of electronics box by a bolt pattern along perimeter of baseplate.

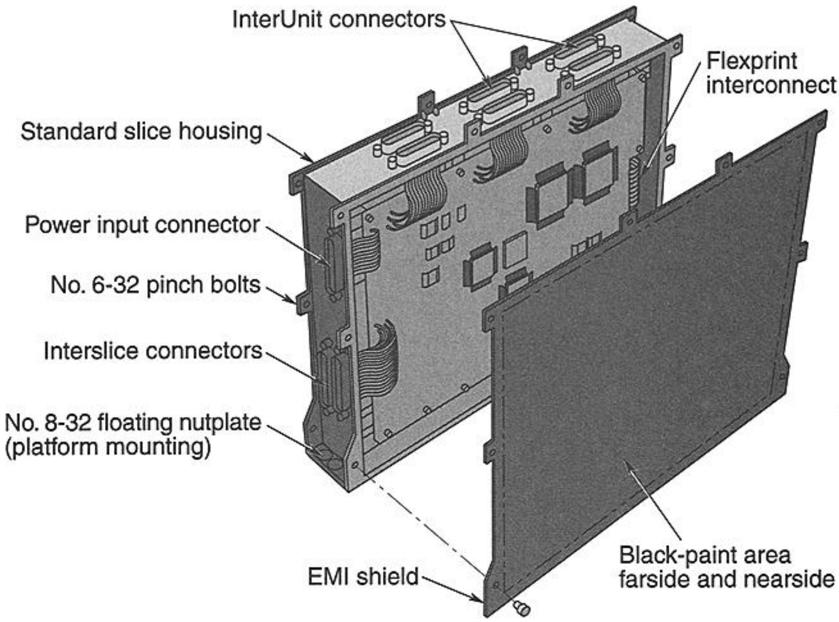

Fig. 8.2. Electronics boxes built up from modules.

Moreover, for the relevant temperature range, –50 to 110°C, the amount of heat transferred via radiation is generally very small compared to the amount transferred by conduction.

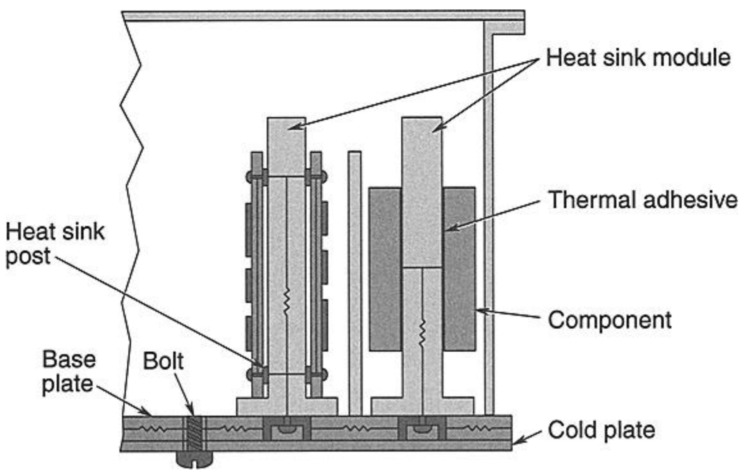

Fig. 8.3. Schematic showing bolt inserted from mounting-plate side.

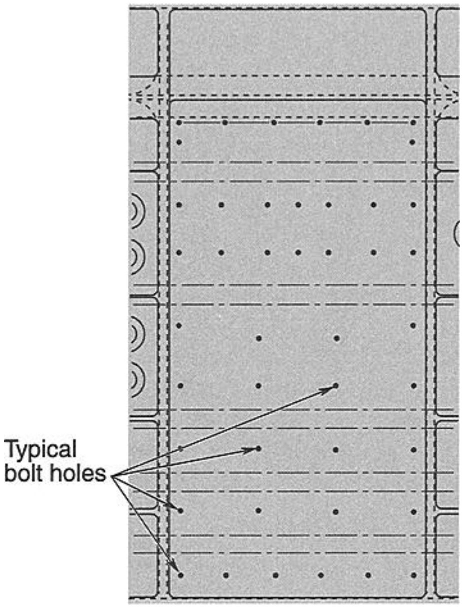

Fig. 8.4. Unit mounting footprint showing bolt holes.

Conduction taking place from one surface to another is called contact conductance. The problem of how to predict heat transfer in contact conductance has been studied widely for the case of two surfaces pressed together under uniform pressure. The corresponding problem for two surfaces that are bolted together and therefore experience a nonuniform pressure profile is considerably more complex; it is discussed in a subsequent section. In what follows here, the measurement of contact-conductance heat flow is characterized by the "heat-transfer coefficient," h, expressed in units of $W/m^2{\cdot}K$. In keeping with spacecraft thermal-control usage, the term "conductance," denoted by C, will be reserved for the product of the heat-transfer coefficient and the area, hA, expressed in units of W/K.

Introduction

Figure 8.5[8.1] shows small- and large-scale imperfections of machined surfaces: roughness and waviness. Roughness typically results from the action of the cutting tool, extrusion die, casting mold, or grinding abrasive.[8.2] Contact resulting from roughness is small-scale contact (microcontact). Waviness can result from vibration or gaps in the machining equipment, or heat treatment.[8.3] Contact resulting from waviness is larger-scale contact (macrocontact).

Flat, Rough Surfaces in Vacuum

Rough-surface contact actually occurs over only a small fraction of the apparent contact area. At each microcontact, heat flow constricts (Fig. 8.6).[8.3] Mikic and coworkers[8.4–8.6] have made some important contributions to the theory of contact

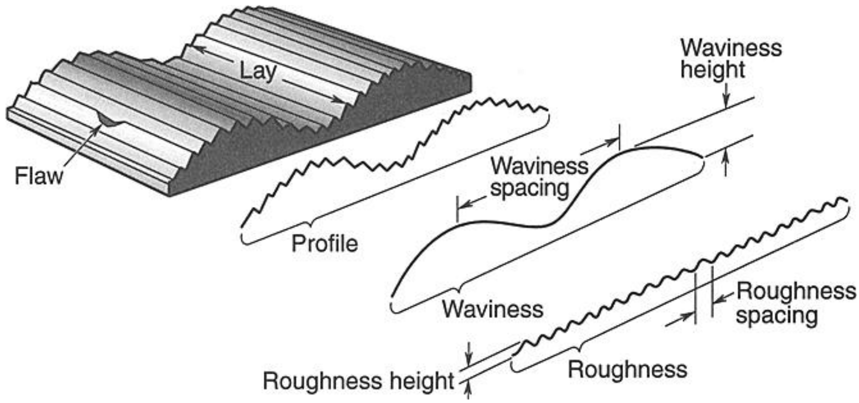

Fig. 8.5. Surface profile showing waviness and roughness.

conductance of flat, rough surfaces. They assumed that the asperity heights can be characterized by a random process that is stationary and for which the distribution of heights is Gaussian above a mean plane. The surfaces' combined profile can then be characterized by the standard deviation of profile height, σ, and the mean of the absolute value of the slope, m. Here $\sigma = (\sigma_1^2 + \sigma_2^2)^{1/2}$, where the subscripts denote the two surfaces. The variable σ is also the root-mean-square (rms) roughness. Typical values of σ_1 and σ_2 are 0.2 to 3.5 µm, although much larger and smaller values are possible (Table 8.1, from *Machinery's Handbook*). If both slopes are normally distributed, then $m = (m_1^2 + m_2^2)^{1/2}$. Slope has been correlated to roughness[8.7] by the equation $m_{1 \text{ or } 2} = 0.076(\sigma_{1 \text{ or } 2} \times 10^6)^{0.52}$ with m sometimes assumed to be in the range 0.10 to 0.15.

The uniform or apparent pressure applied to the surfaces results in much higher pressure on the asperities in contact. When this pressure is sufficiently great that the yield strength is exceeded, elastic deformation transitions to plastic deformation. Because both types of deformation are possible, Mikic developed predictive equations for heat-transfer coefficients for both of them:

$$h_e = 1.55(k_h m/\sigma)(2^{1/2}P/E'm)^{0.94} \qquad \text{(elastic)} \qquad (8.1)$$

and

$$h_p = 1.13(k_h m/\sigma)(P/H_C)^{0.94} \qquad \text{(plastic).} \qquad (8.1)$$

According to Mikic, deformation is predominantly plastic or elastic if the group $\gamma = H_C/(E'm)$ is less than 0.33 or greater than 3.0, respectively. Here k_h is the harmonic-mean thermal conductivity, P is the apparent loading pressure (i.e., the pressure calculated by dividing force by nominal flat surface area), H_C is the contact microhardness of the softer of the two surface materials, and E' is determined by the following equation:

Table 8.1. Surface Roughness Produced by Common Production Methods[a]

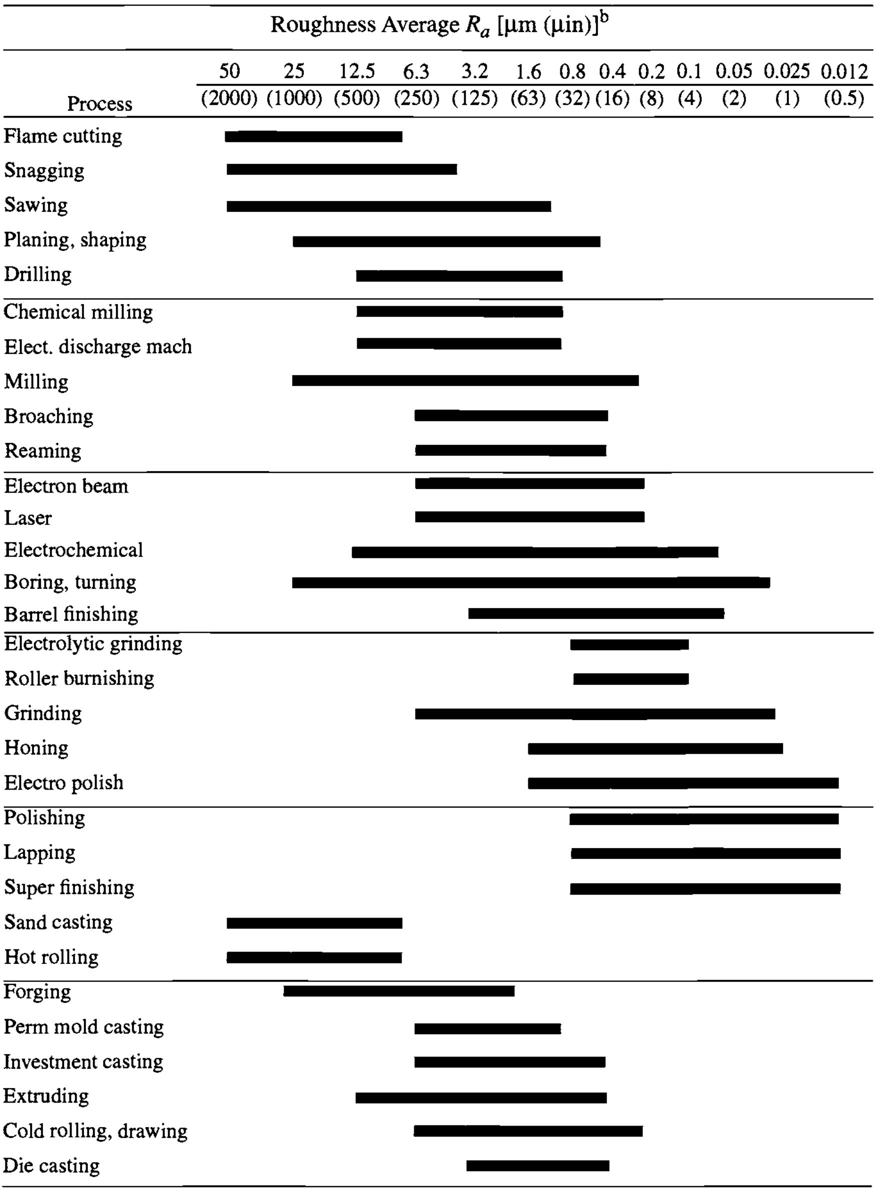

[a]*Machinery's Handbook*, Industrial Press

[b]The ranges shown are typical of the processes listed. Higher or lower values may be obtained under special conditions.

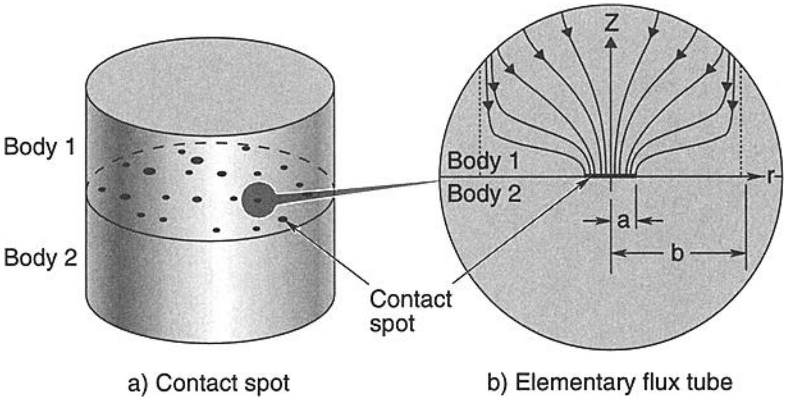

Fig. 8.6. Microcontacts and constricted heat flow. (Courtesy F. Milanez)

$$E' = \{[(1 - \upsilon_1^2)/E_1] + [(1 - \upsilon_2^2)/E_2]\}^{-1}. \qquad (8.2)$$

Lambert and Fletcher[8.7] and Mantelli and Yovanovich[8.3] point out that contact microhardness is significantly greater than bulk hardness, H, or macrohardness, H_L. This difference is the result of the work-hardening of metallic surfaces during machining and further the result of indentor penetration during hardness measurement. Formulas for contact microhardness developed by Hegazy[8.8] and Song and Yovanovich[8.9] are reported to be essentially the same[8.7] and are provided in review papers[8.3,8.7] that discuss deviations from Eqs. (8.1) and (8.2) resulting from anisotropy and heat-flux direction.[8.7] More recently, Sridhas and Yovanovich[8.10] have developed a single elastoplastic model for flat, rough plates. It models and specifies bounds for three regimes: elastic, elastoplastic, and plastic. This model predicts heat-transfer coefficients through an iterative process.[8.3]

Wavy, Rough Surfaces in Vacuum

Clausing and Chao[8.11] modeled surface waviness with spherical crowns (Fig. 8.7). They determined the macrocontact radius a_L from the Hertz model[8.12] for elastic, smooth spheres. From the ratio a_L/b_L the macroconstriction and macrothermal resistance were determined in a manner analogous to that used by Mikic for the determination of microconstriction and microthermal resistance for flat, rough surfaces. This determination assumes that the waviness length, $d_1 + d_2$, is much greater than the roughness, σ, and therefore the asperities do not increase a_L and affect contact pressure distribution. The predictive equations developed by Clausing and Chao for micro and macro heat-transfer coefficients are reported by Mantelli and Yovanovich.[8.3] Total thermal resistance is the series sum of the macro and micro resistances. Lambert and Fletcher[8.7] review numerous expansions of and improvements to the Clausing and Chao theory.

A typical flatness specification for mounting plates calls for flatness less than 0.001 cm/cm and total included reading (TIR) less than 0.5 mm for the footprint. Significant waviness or bowing can be analyzed only with difficulty[8.13,8.14] and must be avoided in practice.

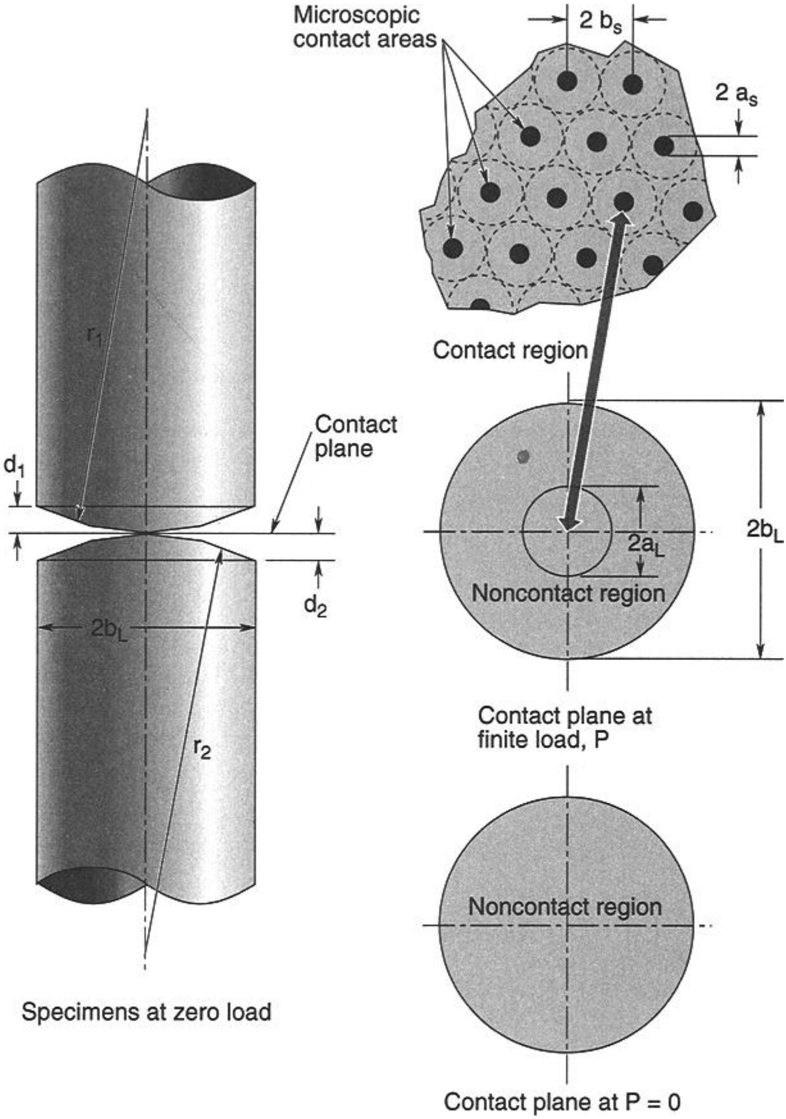

Fig. 8.7. Clausing and Chao[8.11] model for spherical contact.

Effect of Gap Fluid

Before on-orbit use, electronic units are often subjected to thermal tests at ambient pressure. To characterize heat transfer in such ground testing, comparing temperatures reached with those expected in space, is a useful, sometimes necessary, practice. For plates in contact, such heat transfer involves gap conductance in combination with contact conductance.

The initial stage of the analysis considers two noncontacting smooth plates in parallel separated by a gas-filled gap with a width of distance d. Conductive heat transfer through such a gas layer is commonly classified into four heat-flow regimes with distinct ranges of the Knudsen (Kn) number: continuum ($Kn < 0.01$), temperature-jump ($0.01 < Kn < 0.1$), transition ($0.1 < Kn < 1.0$), and free-molecular ($Kn > 10$).[8.15] The Knudsen number is defined as:

$$Kn = (\Lambda/d), \tag{8.3}$$

where Λ is the molecular mean free path and d is the distance separating the plates. In the temperature-jump regime the energy exchange between gas molecules and the plate is incomplete, resulting in a temperature discontinuity at the gas-plate interface.

For the continuum regime the gap heat-transfer coefficient is given by:

$$h_g = k_g/d, \tag{8.4}$$

where k_g is the thermal conductivity of the gas filling the gap. For the temperature-jump, transition, and free-molecular regimes, gas conduction is retarded by rarefaction effects. This retardation is often modeled as a distance serially added to the heat-flow path, with Eq. (8.5) becoming:

$$h_g = k_g/(d + M), \tag{8.5}$$

where $M = [(2 - TAC_1)/TAC_1 + (2 - TAC_2)/TAC_2] \times [2\gamma/(\gamma + 1)](1/Pr)\Lambda$; TAC_1 and TAC_2 are thermal-accommodation coefficients corresponding to the gas-solid combination of surface 1 and 2, respectively; γ is the ratio of specific heats; and Pr is the Prandtl number.

In the more complex case of two plates in contact under pressure, plate separation, d, is replaced by Y, the effective gap thickness. The value of Y depends on plate material(s), pressure, and roughness—and is generally unknown. For the limiting case of low contact pressure, Song *et al.*[8.16] take Y to be R_p, the maximum peak height of the rougher surface of the plates in contact. Further, for very low contact pressure Song and Yovanovich[8.17] provide a semi-empirical, dimensionless equation for predicting h_g:

$$G = f + M^*, \tag{8.6}$$

where $G = k_g/h_g R_p$; $f = 1 + 0.304/[(R_p/\sigma)(1 + M/R_p)] - 2.29/[(R_p/\sigma)(1 + M/R_p)]^2$; $M^* = M/R_p$; and $TAC = 0.55$ (helium), 0.90 (argon), or 0.78 (nitrogen).

Over a fairly wide range of parameters (Table 8.2), for the case of low contact pressure (0.38 to 0.60 MPa), predicted values for the gap heat-transfer coefficient agreed well with experimental results (e.g., Fig. 8.8). More generally, at increased contact pressure, the effective gap thickness is reduced. Prediction of the gap heat-transfer coefficient for this more general case is difficult. While no general predictive method or correlation is available, Song *et al.*[8.18] can provide useful guidance.

Table 8.2. Range of Parameters for Light-Load Gas-Gap Experiments[a]

Parameters	Experiment 1	Experiment 2	Experiment 3	Experiment 4
Specimens	SS 304	SS 304	Ni 200	Ni 200
Gap gases	He, Ar, N_2	He, Ar, N_2	He, Ar, N_2	He, Ar, N_2
σ(μm)	1.53	4.83	2.32	11.8
R_p (μm)	5.55	14.7	8.61	30.6
R_p/σ	3.63	3.04	3.71	2.59
h_c (W/m^2·°C)	452 ± 25	241 ± 3	1130 ± 30	725 ± 30
h_g (W/m^2·°C)	711 to 9660	460 to 5150	625 to 17,900	417 to 7830
h_c/h_g	1.57 to 21.4	1.91 to 21.4	0.553 to 15.8	0.575 to 10.8
P_g (torr)	9.4 to 711	9.5 to 665	9.6 to 698	9.4 to 700
Kn	0.019 to 4.2	0.0078 to 1.6	0.013 to 2.6	0.0034 to 0.76
P (MPa)	0.60 ± 0.02	0.47 ± 0.02	0.52 ± 0.02	0.38 ± 0.01
T_c (°C)	172 ± 4	168 ± 4	170 ± 3	172 ± 4
ΔT (°C)	5.8 to 85.5	6.7 to 105.9	5.5 to 39.9	12.2 to 63.8
q (kW/m^2)	27.7 to 58.7	34.4 to 55.5	52.7 to 104.9	55.9 to 104.1

[a]Song and Yovanovich

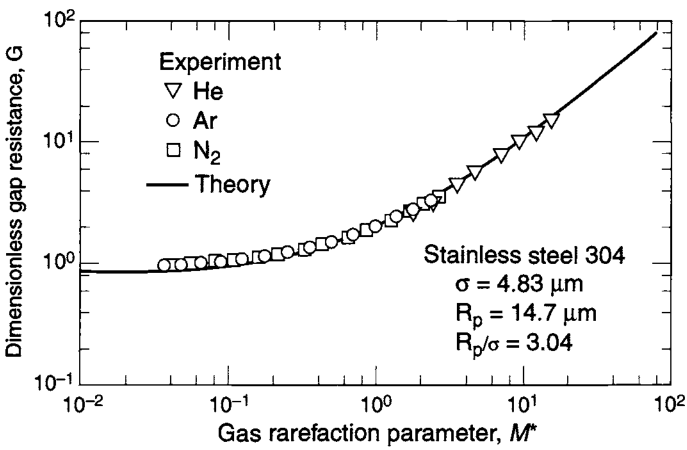

Fig. 8.8. Gap resistance for lightly loaded plates: Comparison of theory and experiments.[8.17]

Data and Correlations

Schneider[8.19] presented heat-transfer coefficient/contact pressure data (Fig. 8.9, Table 8.3) from four sources.[8.20–8.23] These data apply to both vacuum and ambient-pressure cases, and in some cases they include the use of interface fillers. At low contact pressure the curve representing data in air flattens, showing that gap conductance is the primary mode of heat transfer. Swartz[8.24] replotted aluminum-plate data of Fried and Costello,[8.20] Fried and Kelley,[8.25] and Fried and Atkin[8.26] (Fig. 8.10) to obtain continuous curves of heat-transfer coefficient versus apparent contact pressure in vacuum (Fig. 8.11).

Real data are often not well represented by either the early Mikic models [Eqs. (8.1) and (8.2)], the Sridhas and Yovanovich[8.10] elastoplastic model, or the Clausing and Chao[8.11] spherical-crown model. These models represent geometric extremes: Eqs. (8.1) and (8.2) and the Sridhas and Yovanovich model are for flat, rough surfaces, while the Clausing and Chao model is for wavy (nonflat) surfaces where roughness is not accounted for in determining pressure distribution and macrocontact area. Lambert and Fletcher[8.7] point out that the models for flat, rough surfaces usually predict the slope of the line in the graph of heat-transfer coefficient versus apparent pressure to be 0.94 to 0.99, whereas the slope predicted by the Hertz[8.12] theory for smooth spheres is 0.333. Moreover, the correlations for four independent investigations for nominally flat surfaces had slopes that varied from 0.56 to 0.74.[8.7] Thus it appears that many surfaces considered to be flat are indeed not so.

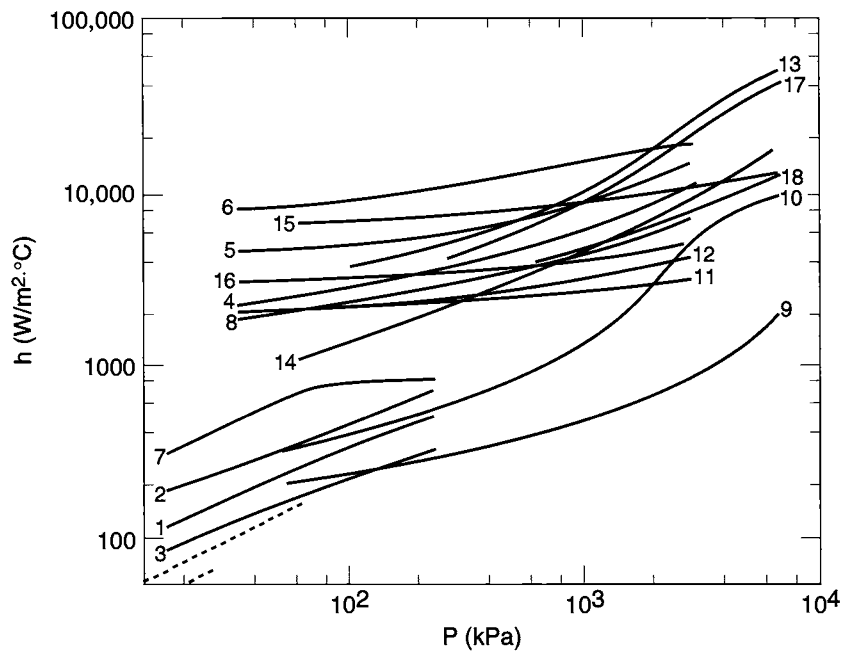

Fig. 8.9. Interface heat-transfer coefficients.[8.19]

Table 8.3. Interface Conditions for Conductance Data in Fig. 8.9

Curve	Material Pair	RMS Surface Finish (μm)	Gap Material	Mean Contact Temp. (°C)
1	Aluminum (2024-T3)	1.2–1.6	Vacuum (10^{-4} mm Hg)	43
2	Aluminum (2024-T3)	0.2–0.5	Vacuum (10^{-4} mm Hg)	43
3	Aluminum (2024-T3)	0.2–0.5 (wavy)	Vacuum (10^{-4} mm Hg)	43
4	Aluminum (75S-T6)	3.0	Air	93
5	Aluminum (75S-T6)	1.6	Air	93
6	Aluminum (75S-T6)	0.3	Air	93
7	Aluminum (2024-T3)	0.2 (wavy)	Lead foil (8 mil)	43
8	Aluminum (75S-T6)	3.0	Brass foil (1 mil)	93
9	Stainless (304)	1.1–1.5	Vacuum (10^{-4} mm Hg)	29
10	Stainless (304)	0.3–0.4	Vacuum (10^{-4} mm Hg)	29
11	Stainless (416)	2.5	Air	93
12	Stainless (416)	2.5	Brass foil (1 mil)	93
13	Magnesium (AZ-31B)	1.3–1.5 (oxidized)	Vacuum (10^{-4} mm Hg)	29
14	Magnesium (AZ-31B)	0.2–0.4 (oxidized)	Vacuum (10^{-4} mm Hg)	29
15	Copper (OFHC)	0.2	Vacuum (10^{-4} mm Hg)	46
16	Stainless/Aluminum	0.8/1.6	Air	93
17	Iron/Aluminum	—	Air	27
18	Tungsten/Graphite	—	Air	132

Lambert and Fletcher[8.7] review models for the thermal contact conductance of metals and provide a methodology for calculating the heat-transfer coefficients.[8.13,8.14] They show that the models of Mikic and Yovanovich overpredict heat-transfer coefficients not only for nonflat surfaces (as is expected for these models, whose basic premise requires flat, rough surfaces), but also for flat surfaces with very small roughness (0.14 to 0.16 μm).[8.13] On the other hand, the Clausing and Chao model generally underpredicts heat-transfer coefficients, perhaps because it does not account for the increased macrocontact area resulting from roughness. The Lambert and Fletcher methodology is the only one known that appears to accurately predict heat-transfer coefficients for nonflat surfaces of any radius of curvature and roughness. It requires the use of several equations and five design charts. It uses the concept of TIR to characterize the flatness deviation

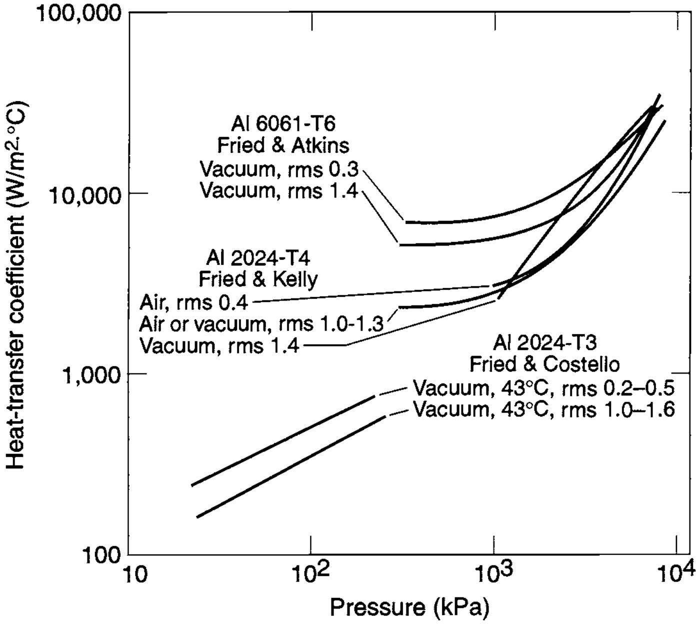

Fig. 8.10. Heat-transfer coefficient vs. pressure for aluminum in vacuum (rms in μm).[8.24]

of two components in contact. It is self-sufficient in that it provides all of the needed relationships or curves, save for the theoretical Hertz radius for smooth spheres, which can be found in the source manuscript[8.12] or in Timoshenko and Goodier.[8.27]

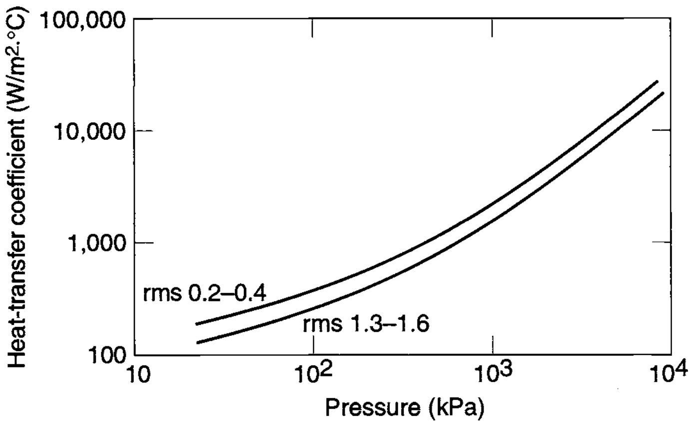

Fig. 8.11. Generalized heat-transfer coefficient vs. pressure for aluminum in vacuum.[8.24]

Bolted-Joint Conductance without Interface Filler

Theory

At the macroscopic level, bolted plates deform elastically, as in Fig. 8.12. Separation of plates, though exaggerated in the figure, does occur, and at relatively small distances from the bolt. In its most basic statement, the bolted-joint problem can be considered the contact-conductance problem for a nonuniform interface pressure. Figure 8.13(a) shows schematics of an interfacial pressure profile with ($\sigma >$ 0) and without ($\sigma = 0$) roughness.

An excellent theoretical treatment of this subject has been provided by Roca and Mikic[8.28,8.29] for plates that are nominally flat when unstressed. Roca and Mikic extended the theory beyond the single-plate midplane work of Fernlund[8.30] and others to two plates with surface roughness. The biharmonic equation was used to characterize the elastic deformation of the plates. Their method assumed that deformation of the plates is elastic, asperity height above a mean plane is Gaussian, and asperity contact is normal with no tangential component. Both plastic and elastic asperity deformation were treated. The structural model used is shown in Fig. 8.13(b), and typical calculated results obtained using an iterative method are shown in Fig. 8.13(c).

The thermal model used by Roca and Mikic is shown in Fig. 8.14(a) for the upper plate. Heat enters around the perimeter, flows radially inward, and then passes from one plate to the other in the contact region. Boundary conditions are:

$$k\frac{\partial T}{\partial Z} = h_C(r)(T - T_i) \qquad \text{at } Z = 0,$$

$$k\frac{\partial T}{\partial Z} = 0 \qquad Z = t,$$

$$k\frac{\partial T}{\partial Z} = 0 \qquad r = D_S/2,$$

and

$$k\frac{\partial T}{\partial r} = q/A \qquad r = R.$$

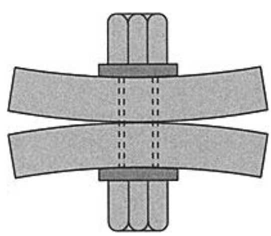

Fig. 8.12. Bolted interface.

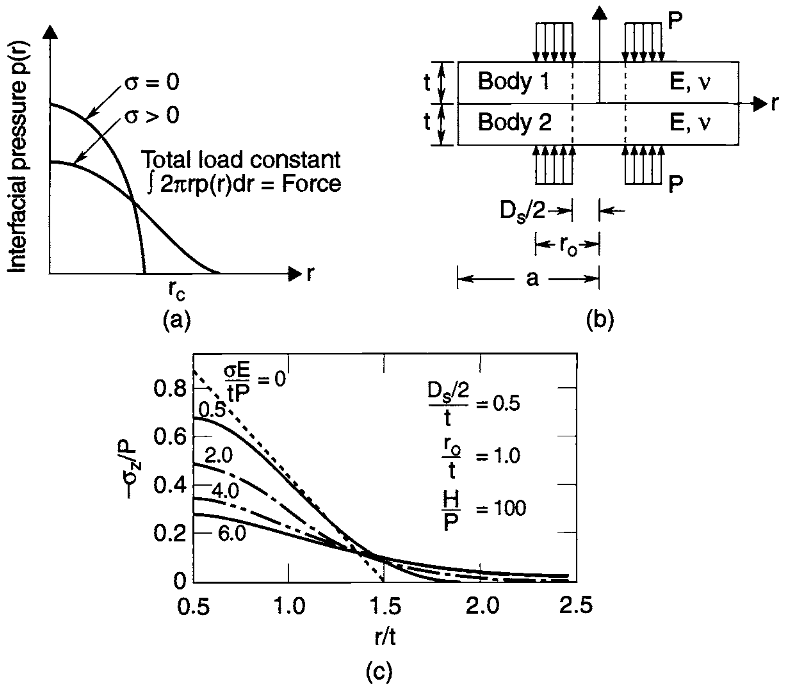

Fig. 8.13. (a) Schematic showing interfacial pressure profiles with and without roughness.[8.28,8.29] (b) Model used by Roca and Mikic[8.28,8.29] for bolted joint. (c) Typical interfacial pressure profiles predicted by Roca and Mikic.[8.28,8.29]

The heat-transfer coefficient in the contact region, h_c, is a function of local pressure, $P(r)$, and is given by

$$h_C = 1.45(km/\sigma)[P(r)/H_C]^{0.985}, \tag{8.7}$$

which is similar to Eq. (8.2). Here, H_C is the lesser of $H_{C,1}$ and $H_{C,2}$.

Roca and Mikic define an overall resistance from the perimeter to a constant-temperature (T_i) region on the other side of the interface:

$$R = [T(r = R, Z = t/2) - T_i]/q/A. \tag{8.8}$$

Their results are shown in Figs. 8.14(b), (c), and (d). Overall thermal resistances vary with roughness (with the group $\sigma E/tP$) in a complex way. The greater the roughness, s, the longer the constricted conduction path from surface to surface, and hence the greater contact resistance. However, as roughness increases, the contact radius increases by virtue of increased interference. This condition tends

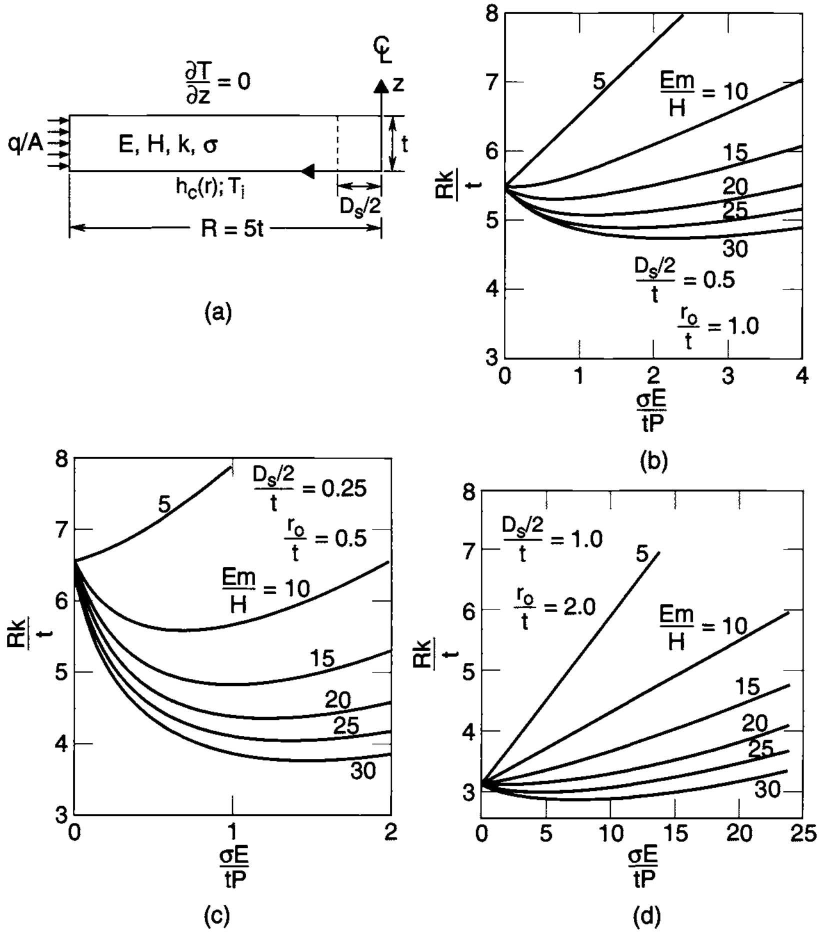

Fig. 8.14. Overall interface resistance from Roca and Mikic.[8.28,8.29] (a) Model used in heat-transfer example. (b), (c), (d) Changes in thermal resistance with roughness.

to decrease the overall thermal resistance by allowing the radial heat inflow to turn downward toward the other plate at a greater radius, decreasing the average heat flux in the contact region. The group *Em/H* in Fig. 8.14 is the inverse of the group γ previously encountered for surfaces under uniform pressure, and it characterizes the propensity for deformation of the asperities to be plastic or elastic.

Roca and Mikic show that, with region size increasing as roughness increases, no simple representation for contact region is possible. Yet rules of thumb have come into use. These rules are generally consistent with elastic analysis of loaded plates with no roughness and with experimental measurements. A popular form is:

$$r_c/t = r_o/t + N. \tag{8.9}$$

The value of N is given by, or can be extracted from, various sources as follows: 1.05 (Fernlund),[8.30] 1.0 (Greenwood),[8.31] 1.3 (Coker and Filon),[8.32] 1.7 (Aron and Columbo),[8.33] and 0.5 (Gould and Mikic).[8.34] For bolted joints, in engineering practice r_C is sometimes taken as $1.5D_S$.

Although it facilitates understanding, the theoretical treatment of Roca and Mikic is not particularly practical. Use of overall resistance commingles contact resistance and plate-constriction resistance, providing many pages of graphical results but few design and analysis aids for the engineer. Bevans *et al.*[8.35] use a simpler model (Fig. 8.15). In it, two plates are bolted together with a contact region A_b with radius R_o. A uniform heat flux, F, is incident on the top plate and exits the bottom plate. Heat flows radially inward in the top plate (the constriction flow) until the contact region is reached. Heat flows from the top plate to the bottom plate in this region. Heat flow in the bottom plate is the reverse of that in the top plate. (Resistors are shown by jagged lines.)

The steady-state heat-conduction equation for a differential element in the region between R and R_o for the top plate can be written

$$q_{\text{out}} - q_{\text{in}} = q_{\text{absorbed}} \tag{8.10}$$

or

$$2\pi krt(dT/dr) - \{2\pi krt(dT/dr) + 2\pi krt[d/dr(rdT/dr)dr]\} = F2\pi rdr \tag{8.11}$$

with the following boundary conditions:

$$\text{At } r = R,\ dT/dr = 0.$$

$$\text{At } r = R_O,\ T = T_O.$$

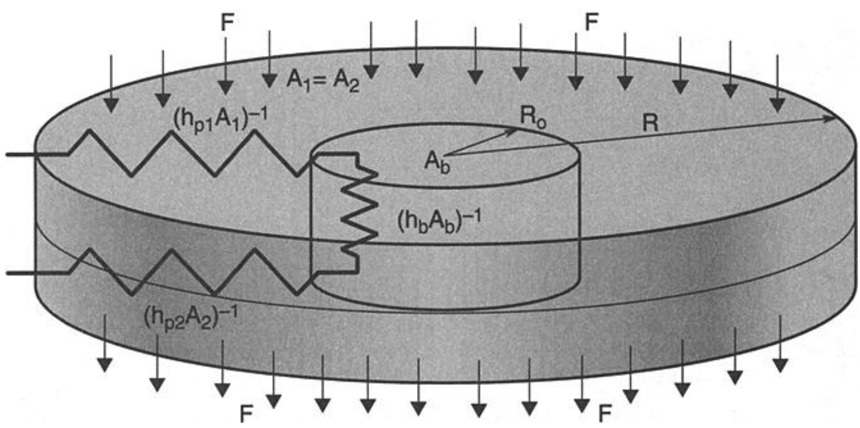

Fig. 8.15. Bolted interface model from Bevans *et al.*[8.35]

Equation (8.12) can be integrated and solved for the temperature distribution across the plate in the region between the edge and the outer radius of bolt contact, yielding

$$T_O - T = (FR^2/kt)\{1/4(\eta^2 - \eta_O^2) + 1/2[\ln(\eta_O/\eta)]\}. \qquad (8.12)$$

In accord with the work of Bevans, the conduction equation can be recast in integral form as

$$Q = h_P \int_{Ro}^{R} (T - T_O)dA, \qquad (8.13)$$

where h_p can be considered a "heat-transfer coefficient" for the region between R and R_o. Noting that $Q = F\pi(R^2 - R_o{}^2)$, one obtains

$$h_P = F\pi(R^2 - R_O^2)/[\int_{Ro}^{R} (T - T_O)2\pi r dr]. \qquad (8.14)$$

Substituting Eq. (8.8) into Eq. (8.10) and integrating, one finds that the heat-transfer coefficient in the plate region from R to R_o becomes

$$h_P = [2k(R^2 - R_O^2)]/\{R^4[\eta_O^2 - (\eta_O^4/4) - \ln(\eta_O) - 3/4]\}. \qquad (8.15)$$

This heat-transfer coefficient is fictitious, as heat does not flow from the top to bottom plate in the region $R > R_o$. More properly, this is the coefficient that would exist if the uniform heat flux F flowed from the top to bottom plate by virtue of the temperature profile of Eq. (8.13).

The overall resistance of the configuration in Fig. 8.15 is given by the equation

$$1/(hA) = 1/(h_{P,1}A_1) + 1/(h_b A_b) + 1/(h_{P,2}A_2), \qquad (8.16)$$

where the subscripts 1 and 2 refer to the top and bottom plates, respectively. After replacing $h_{p,1}$ and $h_{p,2}$ with Eq. (8.16), and noting that $A_1 = A_2$, one finds that the overall heat-transfer coefficient of the approximated bolted joint becomes

$$h = 1/\{\{A R^4[\eta_O^2 - (\eta_O^4/4) - (ln(\eta_O)) - 3/4]/[2A_1(R^2 - R_O^2)]\} \times [1/(k_1 t_1) + (1/(k_2 t_2))] + A/(h_b A_b)\}. \qquad (8.17)$$

If both plates are of the same material, $k_1 = k_2$; using $A = \pi R^2$, one finds

$$A_1 = \pi(R^2 - R_o^2),\ A_b = \pi R_o^2, \text{ and } I = \eta_o^2 - 0.25(\eta_o^4) - ln(\eta_o) - 0.75;$$

results in:

$$h = 1/\{[R^6 I(t_1 + t_2)]/[2(R^2 - R_O^2)^2(kt_1t_2)] + R^2/(h_b R_O^2)\}. \qquad (8.18)$$

The terms in this equation that are not known are R_o and h_b.

Application of Theory: Contact Region

TRW Inc.[8.36] has provided nominal values of thermal resistance across screwed/bolted joints (Table 8.4). The company allows that these values can be increased or decreased depending on such parameters as screw torque, materials, surface finish, and flatness. Recommendations for bolt maximum thermal resistance have been obtained from Lockheed-Martin Inc. (Table 8.5).[8.37] The TRW and Lockheed-Martin results are presented in terms of resistance in consistent units in Table 8.6.

These results are useful for many engineering purposes; however, such results often combine the contact region with a small constriction region near the bolt. This small constriction region, as it is near the centerline, towards which heat fluxes are converging, can have a resistance that is large compared to that of the contact region. A study was therefore conducted to obtain conductances of the contact region per se. Existing data in the literature was reviewed to find studies that contained credible contact-region data. Among other requirements, either the thermocouples had to be located very close to the bolt or, if they were located at some distance, the plate thickness and thermal conductivity had to be sufficiently great that constriction resistance was small compared to contact resistance.

A few suitable studies were found.[8.33,8.35,8.38–8.41] In these, both plates of the surface pair were aluminum alloy save for one test where the surface pair was telluride copper and aluminum alloy. The alloys were not specified in every case; where specified they were usually Al 6061-T6, with Al 6063-T6 used by one investigator. The bolts were all of stainless steel. The range of test parameters is given in Table 8.7. Flatness deviation in terms of TIR is included in the table, although it was not given in all the investigations. From these studies both a dimensional and a dimensionless correlation were developed. The former is shown in Fig. 8.16. Here contact region or bolted-joint conductance in units of W/K is plotted against a corrected torque parameter with units of N·m. Correlation is achieved by the dimensional equation as

$$C_b = 503[\tau(\alpha_{al} - \alpha_{ss})(T_p - 200)]^{0.775} \tag{8.19}$$

Table 8.4. Thermal Conductance Design Guideline from TRW

	Conductances (W/K)	
Screw Size	Small Stiff Surfaces	Large Thin Surfaces
2–56	0.21	0.105
4–40	0.26	0.132
6–32	0.42	0.176
8–32	0.80	0.264
10–32	1.32	0.527
1/4–28	3.51	1.054

Table 8.5. Bolt Thermal Resistance Estimate

Maximum Resistance versus Bolt Size and Plate Thickness (°C/W bolt)[a]					
Steel Bolt					
Size	Shaft Diam (mm)	1.57 mm Aluminum	3.18 mm Aluminum	6.35 mm Aluminum	9.53 mm Aluminum
NC 4-40	2.84	12.6	—	—	—
NC 6-32	3.51	6.6	2.2	—	—
NC 8-32	4.17	4.5	1.5	0.75	—
NF 10-32	4.83	3.0	1.0	0.50	0.30
NF 1/4-28	6.35	2.1	0.7	0.19	0.23
NF 5/16-24	7.92	1.5	0.5	0.25	0.17
NF 3/8-24	9.53	—	0.4	0.19	0.13
NF 7/16-20	11.10	—	—	0.16	0.11
NF 1/2-20	12.70	—	—	—	0.09

[a]Assumptions:
- Typical spacecraft bolted aluminum interface in vacuum
- Bare clean mill rolled surface finish
- Standard steel bolts torqued to specification
- Primary heat transfer through compressed area near bolt

Note: Confirmation measurements suggested for thermal-design purposes
Reference: NASA CR119933 June 1971 and other limited measurements

Table 8.6. TRW and Lockheed Martin Bolted-Joint Resistance Data

		Resistance Values from Several Sources (°C/W)[a]					
		TRW Large Thin	LM Plate Thickness (mm)[c]				TRW Small Stiff
Bolt	Diam (mm)	Surfaces[b]	(1.57)	(3.18)	(6.35)	(9.53)	Surfaces[b]
2-56	—	9.48	—	—	—	—	4.74
NC 4-40	2.8	7.59	12.6	—	—	—	3.79
NC 6-32	3.5	5.69	6.61	2.2	—	—	2.37
NC 8-32	4.2	3.79	4.5	1.5	0.75	—	1.25
NF 10-32	4.8	1.90	3.0	1.0	0.5	0.333	0.76
NF 1/4-28	6.4	0.95	2.1	0.7	0.35	0.233	0.28
NF 5/16-24	7.9	—	1.5	0.5	0.25	0.167	—
NF 3/8-24	9.5	—	—	0.39	0.194	0.128	—
NF 7/16-20	11.1	—	—	—	0.16	0.106	—
NF 1/2-20	12.7	—	—	—	—	0.089	—

[a]Bolted aluminum interface in vacuum, bare clean mill rolled surface finish (LM), standard steel bolts torque to specification (LM), primary heat transfer through compressed area near bolt (LM).
[b]TRW, March 1984.
[c]LM, George D. Rhoads, 20 July 1988.

Table 8.7. Bolted-Joint Correlation: Range of Test Parameters

Range	Bolt Size	Bolt Shaft Diam (mm)	Torque (N·m)	Plate Thickness (mm)	Roughness σ (m/m/K)	Flatness TIR (m)	Plate Temp. (°C)	Conductance (W/K)
Minimum	6–32	3.51	0.34	1.02	6.26×10^{-7}	1.02×10^{-5}	19.3	0.41
Maximum	1/4–20	6.35	9.39	12.70	2.26×10^{-6}	1.27×10^{-4}	127.3	13.8

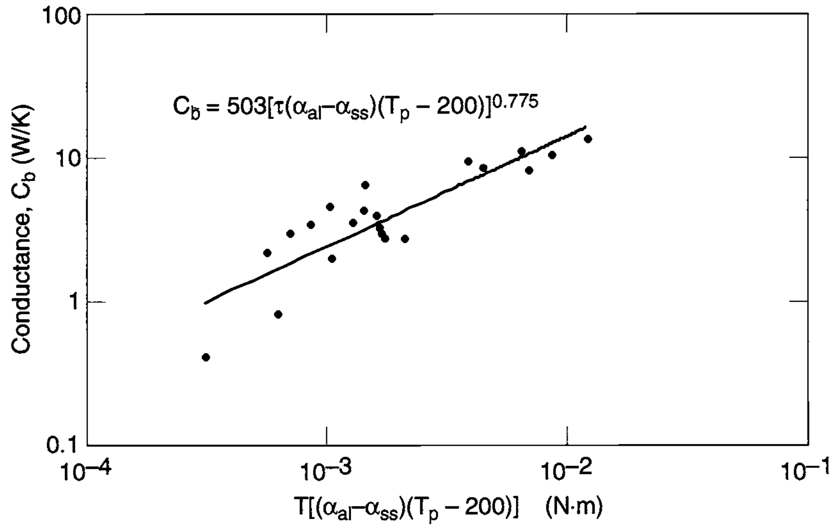

Fig. 8.16. Dimensional correlation of bolted-joint conductance.

with an R^2 value of 0.75. Observation has shown, for the aluminum plate–stainless steel bolt combination, that differential expansion and contraction affect the torque.[8.42,8.43] Hence the applied torque, τ, is multiplied by the correction factor $(\alpha_{al} - \alpha_{ss})(T_p - 200)$. The first term in parentheses is the difference in the coefficients of thermal expansion for aluminum and stainless steel. The second term is the plate temperature minus a lower-limit temperature, 200 K. Observation has shown that as temperature is reduced, at some point torque decreases rapidly.[8.43] That lower limit is taken here as 200 K.

The dimensionless correlation obtained is shown in Fig. 8.17. The resulting equation is

$$C_b/(k_h\sigma) = 1.06 \times 10^9\{[\tau(\alpha_{al} - \alpha_{ss})(T_p - 200)]/(E'\sigma^{2.5}D_S^{0.5})\}^{0.652} \qquad (8.20)$$

with an R^2 value of 0.76. The conductance, C_b, is normalized by dividing by the harmonic-mean thermal conductivity, k_h, and the combined rms roughness, σ. The

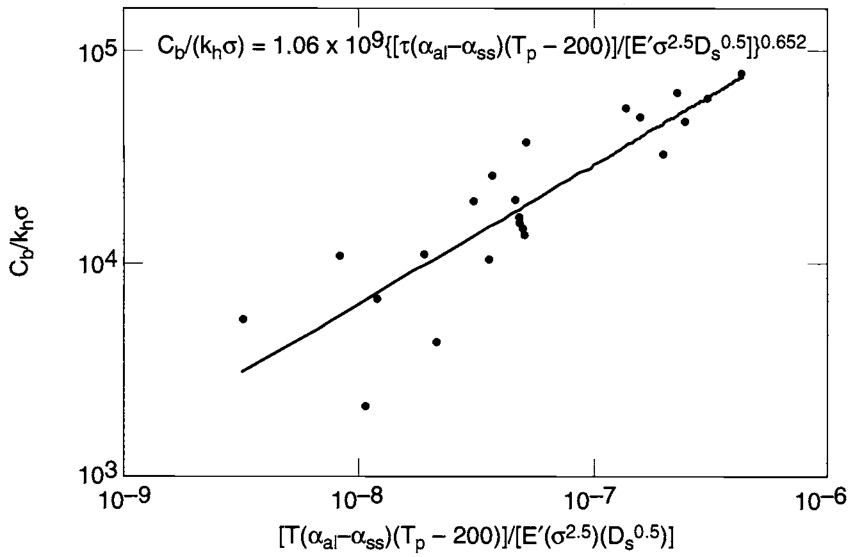

Fig. 8.17. Dimensionless correlation of bolted-joint conductance.

numerator of the ordinate of Eq. (8.21) is the ordinate of Eq. (8.20). The denominator is the product $E'\sigma^{2.5}D_S^{0.5}$. The term E', the effective modulus as defined by Eq. (8.3), was used in the correlation rather than microhardness, H_C, as the latter is a more complex term, itself a function of the unknown applied pressure. The term D_S is the diameter of the bolt shaft. Flatness deviation, TIR, could not be included in the correlation as it was not provided by all the investigators. Roughness, σ, while provided by all the investigators, was not always measured in a consistent manner, and slope, m, was not measured by any investigator. Plate thickness was found to be a poor correlation parameter. The slopes of Eqs. (8.20) and (8.21) are lower than that of Eq. (8.1) for flat surfaces subjected to uniformly applied pressure. This may be a characteristic of torque-applied pressure as well as a result of the (largely unknown) flatness deviation of the surfaces tested. The conductances given by Eqs. (8.20) and (8.21) are a few times greater than those recommended in Tables 8.4 through 8.6. This is believed a consequence of near elimination of constriction effects in the selected tests. To convert these conductances to heat-transfer coefficients, h_b, as used in Eqs. (8.17) through (8.19), the relations $h_b = C_b/\pi\, r_C^2$ and $r_C = 1.5D_S$ should be used.

Application of Theory: Overall Conductances

The correlations of Eq. (8.20) and (8.21) apply only to the bolt or screw contact region and do not characterize the constriction conductances within the two plates. Overall conductances include both the bolt and the constriction terms. For axisymmetric heat flow to the bolt region, overall conductance is given by Eq. (8.18) or (8.19).

Perimeter Bolt Pattern

For configurations where a perimeter bolt pattern is used, the analysis method of Bevans *et al.*[8.35] is recommended. The plate is divided into sectors (Fig. 8.18) with Eqs. (8.10) to (8.19) applicable. As an example Fig. 8.19 shows a 90-deg segment where radius R_o is equal to r_C of Eq. (8.10). For more complex shapes or for cases where thickness is not constant, the overall thermal network can be modeled using finite-difference or finite-element methods. Bolt-region conductances from Tables 8.4 through 8.6 or Eqs. (8.20) and (8.21) can be used in such models.

Where the perimeter bolt pattern employs bolts on two opposed flanges, a rectangular version of Bevans's equation can be used. In this case a strip between two bolts is subjected to a uniform flux, F (Fig. 8.20). Following Bevans for a half-slice leads to

$$T - T_O = (F/2kt)(L^2 - x^2) \tag{8.21}$$

$$h_P = FWL/[\int_0^L (T - T_O)w\,dx]. \tag{8.22}$$

Substituting Eq. (8.22) into Eq. (8.23) and integrating, one finds

$$h_P = 3kt/L^2. \tag{8.23}$$

Plate conductance is

$$C_P = h_P A_P = (3kt/L^2)WL = 3ktW/L. \tag{8.24}$$

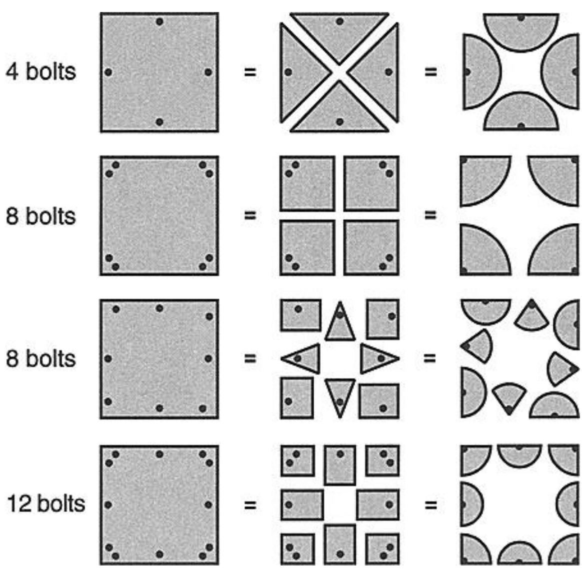

Fig. 8.18. Division of plates with perimeter bolt mounting from Bevans *et al.*[8.35]

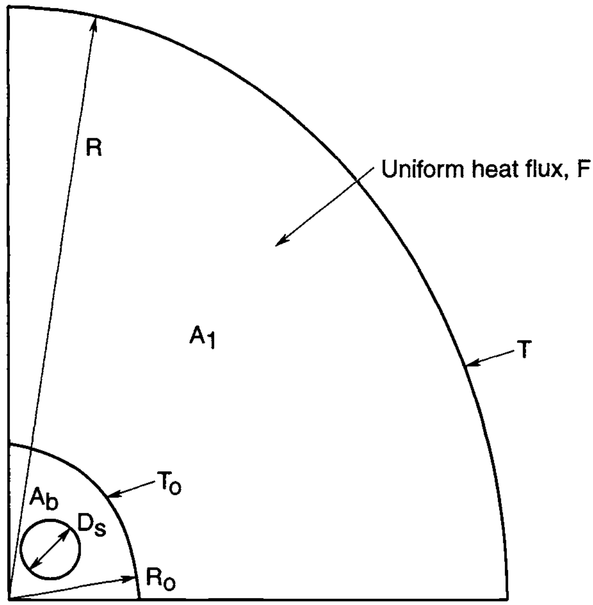

Fig. 8.19. Elementary conduction element, four bolts, perimeter-mounted.

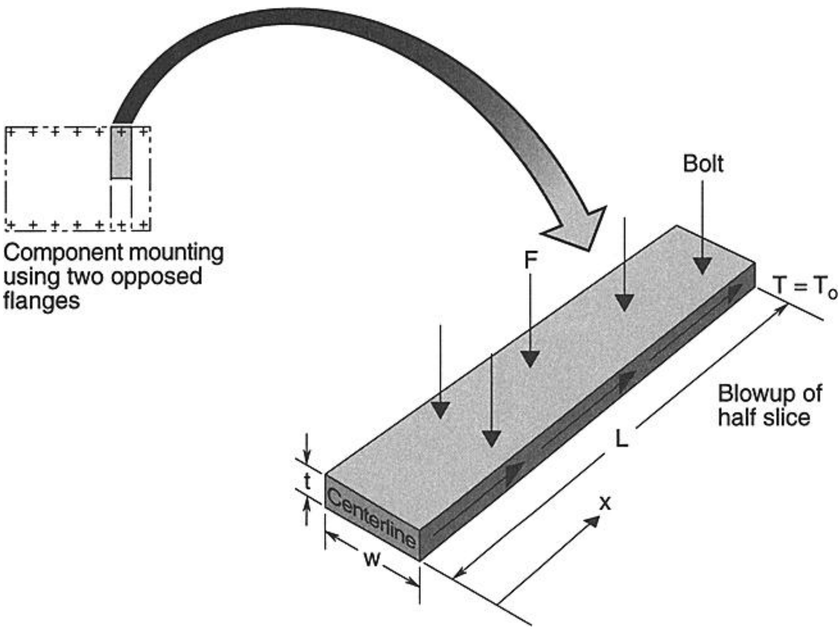

Fig. 8.20. Model of conduction heat flowing in a slice.

If heat entered the half-slice entirely at the centerline end, the conductance would be

$$C_P = ktW/L, \tag{8.25}$$

which is one-third the conductance for the uniform-heat-flux case. Equation (8.24) or (8.25) can be used with the bolt-region heat-transfer coefficient or conductance to obtain the overall heat-transfer coefficient [Eqs. (8.17) through (8.19)] or overall conductance.

A design recommendation is available from TRW Inc.[8.36] for average overall heat-transfer coefficients for perimeter bolt patterns (Fig. 8.21). This recommendation derives from the work of Bevans *et al.*[8.35] for the configurations of Fig. 8.22. Plates are relatively thin, with $t_m = (1.59 + 3.17)/2 = 2.38$ mm. Results are characterized by inverse screw density (in cm^2 per screw). Heat-transfer coefficients for the bare interface are small, generally below 115 $W/m^2 \cdot K$; this condition is a consequence of the constriction-plate resistances for the long spans between bolts, i.e., bolt-contact-region conductances are relatively high compared to the constriction-plate conductances.

This information is verified and supplemented by the work of Welch and Ruttner.[8.41] The configuration they studied is shown in Fig. 8.23 with Al 6063-T6 plates that were each 7.94 mm thick. The 279-mm-by-152-mm plates were fastened by 16 No. 8-32 stainless-steel screws. Torques were 1.13 and 2.26 N·m. Average heat-transfer coefficients for the entire plate, provided by the authors, are given in Table 8.8.

The Welch and Ruttner screw-spacing results in 26.6 cm^2/screw, which for the Bevans configuration yields a heat-transfer coefficient of about 90.8 $W/m^2 \cdot K$. The Welch coefficients are a factor of three to four greater than those of Bevans. This difference is explained to a large degree by the ratio of the arithmetic-mean plate thicknesses for the two investigators:

$$\frac{t_{m,\mathrm{Welch}}}{t_{m,\mathrm{Bevans}}} = \frac{7.94}{0.5(1.59 + 3.17)} = 3.34 \tag{8.26}$$

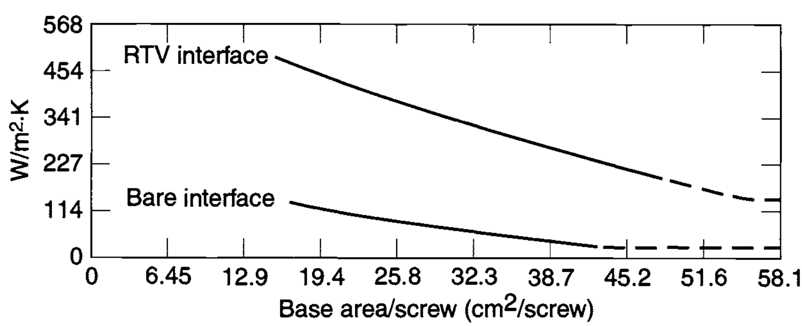

Fig. 8.21. Recommended overall heat-transfer coefficients for perimeter bolt pattern from TRW Inc.[8.36]

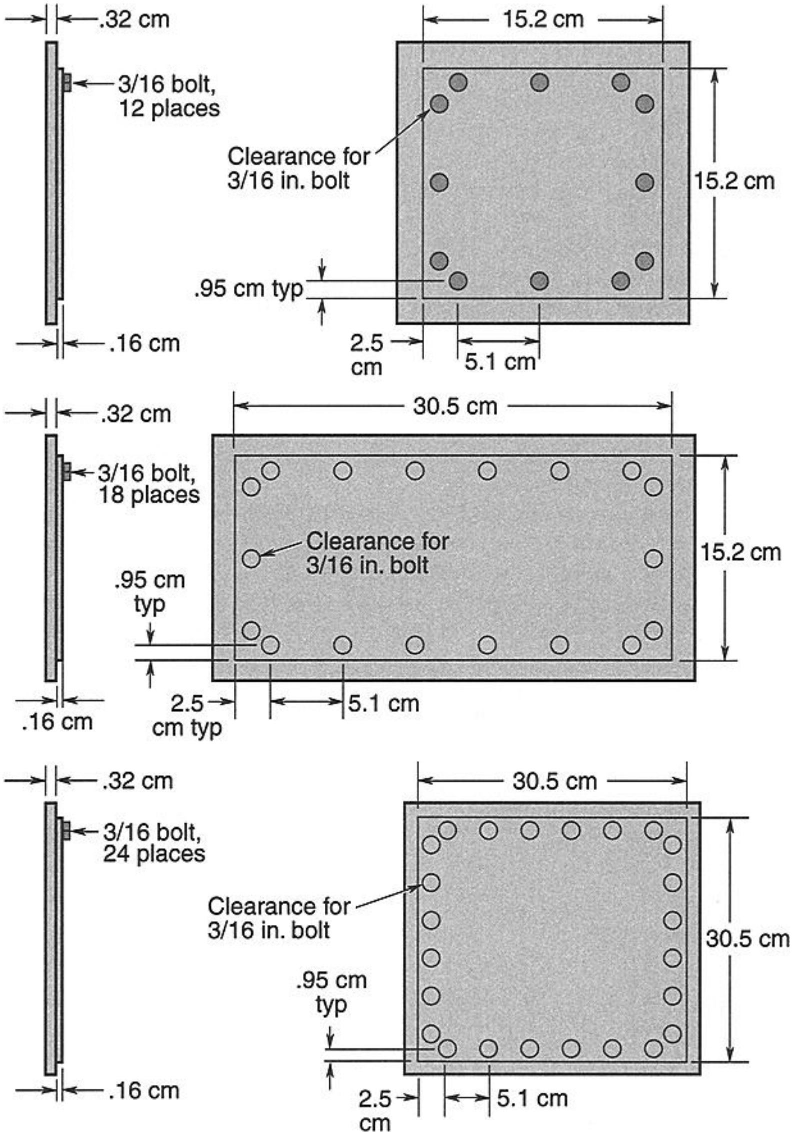

Fig. 8.22. Bolted-joint configurations tested by Bevans *et al.*[8.35]

Therefore, for perimeter-bolt-pattern fastening of an electronics unit to a mounting plate, the bare interface curve of Fig. 8.21 should be used for mean plate thickness of about 2.5 mm. Table 8.8 should be used for plates with thickness closer to 7.5 mm. Results obtained this way can be cross-checked by computing overall heat-transfer coefficients using one of the geometries of Fig. 8.18 and Eqs. (8.18) or (8.19), or by using a finite-difference or finite-element thermal model. Contact

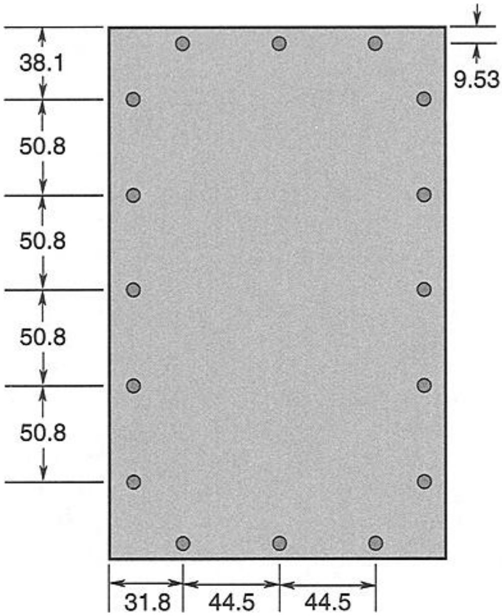

Fig. 8.23. Bolted-joint configuration tested by Welch and Ruttner (dimensions in mm).[8.41]

Table 8.8. Welch and Ruttner Bare Interface Results Summary

Torque (N·m)	Temperature (°C)	Average Heat-Transfer Coefficients (W/m^2·K)
1.13	–34	284
1.13	71	369
2.26	–34	329
2.26	71	397

(bolt) region conductances are to be obtained for either approach from the "Application of Theory: Contact Region" section.

Nonperimeter Bolt Patterns

Figure 8.4 shows a bolt pattern that combines perimeter and inboard bolts as described in the "Conduction Cooling" section. For the configuration of this figure and other configurations encountered in practice, a number of the bolts are in a uniform or near-uniform pattern. These bolts could be analyzed individually using the plate-division method of Fig. 8.18 and the analytic techniques given above. However, such analysis can be time-consuming and, moreover, heat flows through parallel bolts were found not to be independent for at least one case with $d^* = 5$.[8.44] Here $d^* = d/(2r_O)$, where d is the distance between bolt centers and r_O

is the radius of the applied load. Therefore a simpler, approximate method was developed to predict an overall heat-transfer coefficient for uniform bolt spacing. The result, a dimensional correlation,

$$ht_t/k_h = 54.7[A_N/(t_t^3\tau^{0.5})]^{-0.764}, \tag{8.27}$$

is shown in Fig. 8.24. Here ht_t/k is dimensionless; h is the overall heat-transfer coefficient, t_t is the thinnest of the two plates in contact, and k_h is the harmonic-mean thermal conductivity. The term $A_N/(t_t^3\,\tau^{0.5})$ has dimensions $[m(m-N)^{0.5}]^{-1}$, where A_N is the area per bolt or screw, t_t is the thickness of the thinnest of the two plates in contact, and τ is the torque. Data came from General Electric Inc. reports and from six TRW Inc. reports (the latter supplied by H. A. Pudewa). The correlation has an R^2 value of 0.93 and includes data with the following ranges: plate thickness from 1.59 to 25.4 mm, torque from 0.037 to 9.48 N·m, bolts from 0-80 to 1/4-20, bolt area per screw of 0.272 to 19.4 cm^2, with screw patterns ranging from a single screw to 5 by 2. The screws were all stainless steel, and all the plates were aluminum alloys save for a set where one plate was copper.

Honeycomb Mounting Plates

Often the spacecraft side of the interface is of honeycomb/facesheet construction (Fig. 8.25). Threaded inserts must be embedded in the honeycomb to receive the screws. Such construction provides high ratios of stiffness and strength to weight. However, facesheet thickness for practical applications can be well below 1.0 cm, typically 0.4 to 1.2 mm. Honeycomb facesheets tend to be less flat, but stiffer, than thin metal plates—resulting in counterbalancing effects on overall conductance.

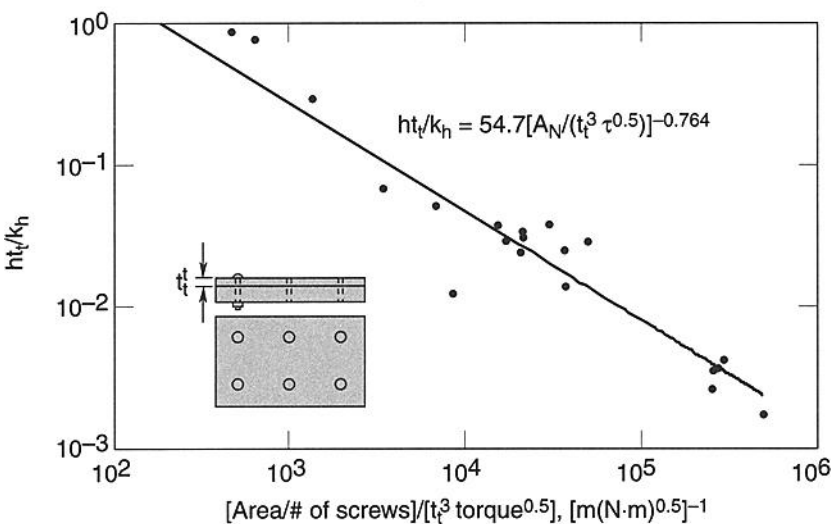

Fig. 8.24. Dimensional correlation for overall heat-transfer coefficient for a uniform bolt pattern.

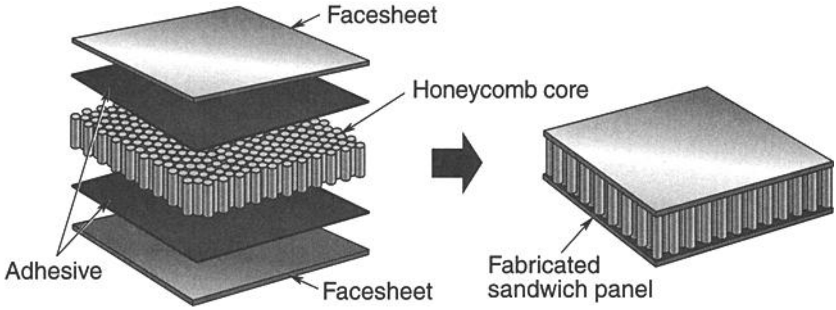

Fig. 8.25. Honeycomb/facesheet mounting panel.

Because the facesheets are thin, constriction resistance is relatively high. Few experimental data are available on conductances where honeycomb-mounting-panel construction is used, either in the contact region or for the entire mounting region. Unless data are available, overall conductance values no higher than those for the bare interface in Fig. 8.21 should be used.

If heat pipes are embedded in the honeycomb below the unit, overall conductance tends to increase. This is especially so if the heat pipes bridge from facesheet to facesheet. General results are not available. However, the problem can be treated by developing thermal math models (TMMs) that account for the various conduction paths.

Bolted-Joint Conductance with Interface Filler

Contact conductance can be improved through the use of appropriate filler materials between the two plates. Such materials fill the microscale voids present because of surface roughness, and some materials can also fill the macroscale voids resulting from flatness deviation. For the microscale voids, because the dimensions are small, even a low-conductivity material, if thin enough, may provide an improvement over the radiative heat transfer that existed before filling. However, care must be exercised in the use of fillers. Fletcher *et al.*[8.45] show in Fig. 8.26 that a wide variety of fillers have a lower heat-transfer coefficient than an unfilled bare aluminum joint. Such fillers are thermal insulators and may be useful for applications where thermal isolation is required. As a rule of thumb, for a given thickness, filler thermal performance is proportional to thermal conductivity divided by hardness. For convenience, fillers can be divided into three classes: greases, gaskets, and cured-in-place room-temperature-vulcanized (RTV) silicone compounds. Greases and gaskets are available from many suppliers in a wide variety of materials, and the offerings are summarized in Appendix C, "Summary of Thermally Conductive Filler Materials and Suppliers."

Use of fillers can create problems not present with bare interfaces. These include interference with unit grounding, inability to remove a unit for rework (or difficulty in doing so), structural loads, contamination, and outgassing—the last two problems being particularly important in spacecraft applications. Other considerations in the use of fillers are: electrical isolation as evidenced by high dielectric strength and breakdown voltage; mechanical properties such as compressive

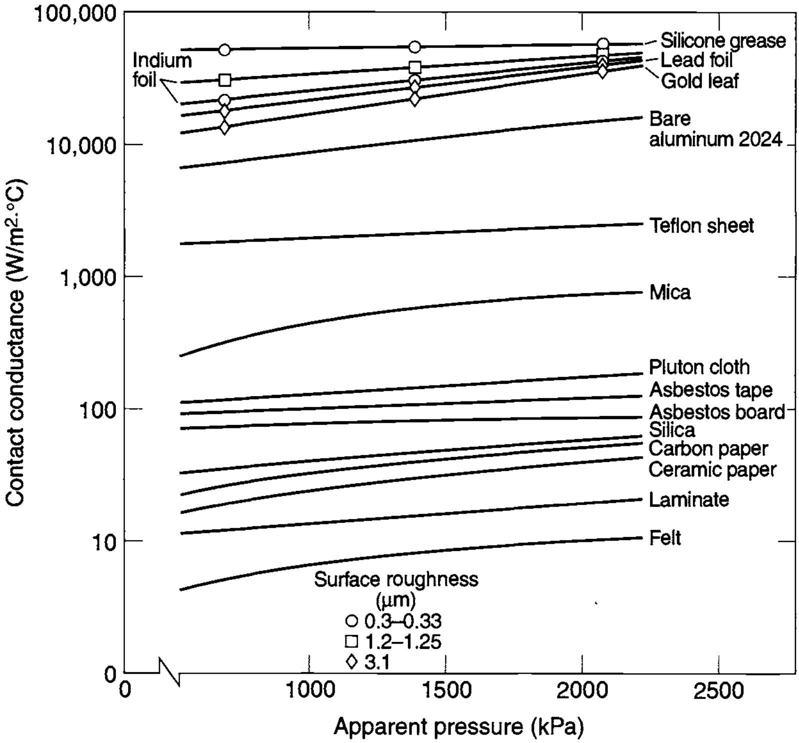

Fig. 8.26. Heat-transfer coefficients of selected interstitial materials.[8.45]

deflection, stress relaxation, and compressive set; and chemical and heat resistance. Silicone grease has superior thermal performance (Fig. 8.26) but may be a source of contamination. Greases without silicone mitigate this problem and are seeing some usage in small, less-expensive spacecraft. However, for the vast majority of spacecraft applications, thermal gaskets and cured-in-place RTV silicone compounds are the fillers of choice.

Thermal Gaskets

A variety of thermal gaskets are available for use with bolted joints. Application of such gaskets is shown in Fig. 8.27. To provide the desired thermal performance, some of these gaskets must be subjected to high pressure (Fig. 8.28). This creates structural loads and can cause bowing of the mounting panel. Moreover, separation (zero pressure) may occur at some distance from the bolt (Fig. 8.29). These conditions typically limit use of thermal gaskets to applications where the span between bolt centerlines is not large.

The Chomerics Division of Parker Hannifin Corporation provides a variety of thermal gaskets under the trade name CHO-THERM (Table 8.9). They are often thermally conductive but electrically isolating materials loaded with thermally conductive particles (aluminum oxide, magnesium oxide, boron nitride) within an

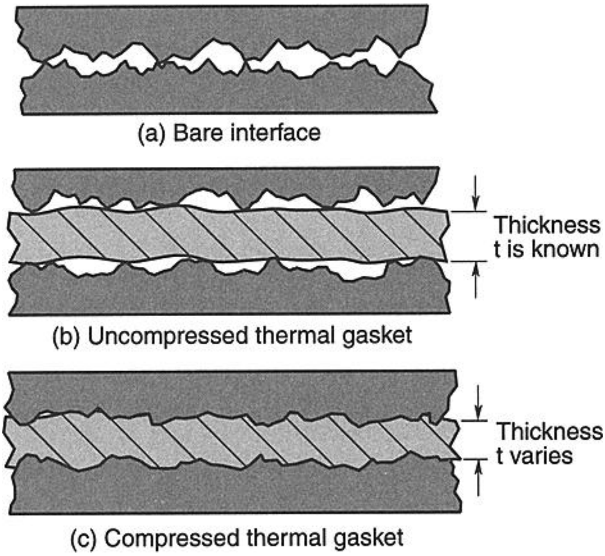

Fig. 8.27. Use of thermal gaskets as an interface filler.

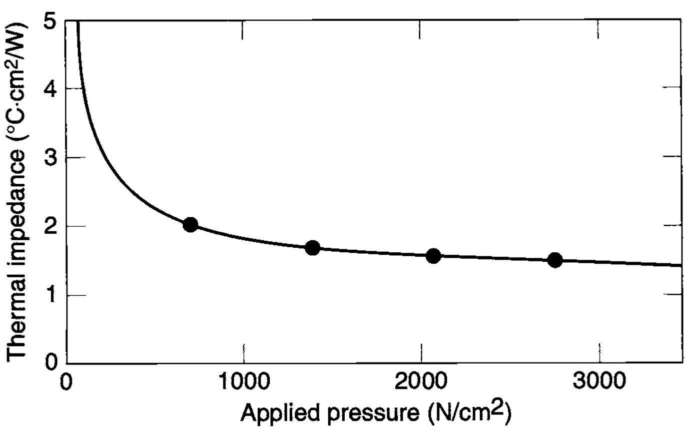

Fig. 8.28. Thermal impedance vs. pressure for CHO-THERM 1671 material.

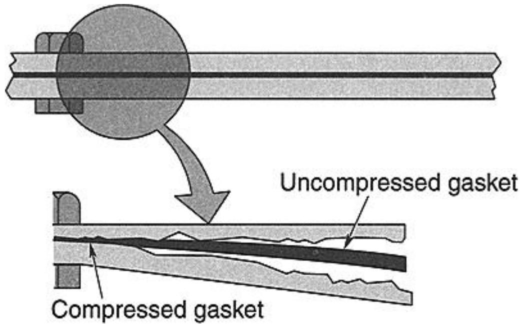

Fig. 8.29. Bolted-joint configuration with gasket.

elastomeric binder (silicone, fluorosilicone, urethane). These gaskets are tailored to provide a variety of special capabilities: dielectric strength; EMI shielding; ability to conform well to surface irregularities; solvent, temperature, and cut-through resistance. Table 8.10 provides properties for a number of CHO-THERMs.

While suitable for many applications, CHO-THERM has a limitation when used as a thermal gasket for unit mounting: It has an extremely high electrical resistivity, on the order of 10^{14} to 10^{15} Ω cm. The use of a continuous sheet may preclude meeting unit electrical-grounding requirements. A typical requirement is that the electrical resistance from unit to mounting be less than 2.5 mOhm. Therefore, if CHO-THERM is used, an auxiliary grounding method should be considered. This could be the use of gasket cutouts in the bolt region where compressible wire-grounding mesh is installed, or it could be the use of grounding straps.

Polycarbon, Inc., a member of the SIGRI Group, provides a flexible graphite gasket, Calgraph. Its typical properties are given in Table 8.11. Comparing this information with the CHO-THERM information in Table 8.10, one finds the Calgraph thermal conductivity normal to the surface two or three times greater than that for CHO-THERM, and the thermal conductivity parallel to the surface 59 to 150 times greater. Electrical resistivity is 15 to 18 orders of magnitude less. That is, Calgraph is a sufficiently good electrical conductor that it can, perhaps, be used as a continuous gasket and still meet unit-grounding requirements. Alfatec GmbH offers KERATHERM graphite gaskets in either a blank version or in electrically insulated versions laminated with wax or filled adhesive. The wax laminate incorporates a phase-change material. Unlaminated graphite gaskets should be used with caution in joints that may be disassembled, because electrically conductive carbon fibers and particles can be generated as the material shreds when the surfaces are separated. Processes must be in place to ensure that all conductive particles are contained so that they cannot find their way into electrical connectors or moving mechanical assemblies and cause shorts or jamming.

Table 8.9. CHO-THERM Properties and Features[a]

Compound	Properties						Features						
	Thermal Impedance[a]	Dielectric Strength[a]	Fiberglass-Reinforced	Polyimide - Reinforced	Polyester-Reinforced	Aluminum-Reinforced	No Mounting Pressure Required	Contains No Silicone	Continuous Rolls for Automation	Custom-Molded Pads	Thermal Adhesive	Resists Petrochemcals and Hydrocarbons	NASA Outgassing Approved
1679 Boron nitride, silicone	L	M	•										•
1671 Boron nitride, silicone	L	M	•										•
1661 Boron nitride, silicone	L	M											•
1678 Boron nitride, silicone	L	M	•										
1674 Aluminum oxide, silicone	M	M	•						•				
1677 Boron nitride, fluorosilicone	M	M	•									•	•
1682 Magnesium oxide, urethane	M	M			•			•	•				
1684 Magnesium oxide, urethane	M	H						•	•				
1688 Boron nitride, urethane	L	H		•				•	•				
1694 Magnesium oxide, silicone	M	H		•					•				
1698 Boron nitride, silicone	L	H		•					•				
1680 Boron nitride, Kapton,[b] silicone	M	H		•			•		•				
1646 Boron nitride, silicone	L	None		•		•			•				
T274 Aluminum oxide, silicone	M	H	•							•			
1641 Aluminum oxide, silicone	M	M									•		
1642 Aluminum oxide, silicone	M	M									•		

[a]L = Low; M = Moderate; H = High.
[b]Trade name

Table 8.10. CHO-THERM Typical Properties

Typical Properties	1679	1671	1677	1674	1678	1661	Test Method
Binder	Silicone	Silicone	Fluorosilicone	Silicone	Silicone	Silicone	—
Filler	Boron nitride	Boron nitride	Boron nitride	Aluminum oxide	Boron nitride	Boron nitride	—
Color	Yellow	White	White	Blue	Red	White	—
Thermal conductivity (W/m·°C)	2.7	2.4	2.1	1.2	1.9	3.8	Chomerics Test Method No. 28
Thermal impedance $\left(\frac{°C \cdot cm^2}{W}\right)$	.97–1.16	1.16–1.42	2.45–2.71	1.94–2.19	1.42–1.55	1.55–1.81	Typical flat plate test values
Voltage breakdown rating (VAC)	4000	4000	4000	2500	2500	4000	ASTM D149
Outgassing (% TML) (% CVCM[a])	0.40 0.10	0.76 0.07	0.57 0.01	0.45 0.20	0.55 0.12	0.76 0.08	ASTM E 595-77
Thickness (mils)	10±2	15±2[b]	20±4	10±2	10±2	20±3[c]	—
Tensile strength (kPa)	6900	6900	2800	10,300	6900	1400	ASTM D412
Tear strength (kg/cm)	18	18	11	18	18	1.8	ASTM D624
Elongation (%)	10	2	10	2	10	2	ASTM D412
Hardness (Shore A)	95	90	85	90	90	90	ASTM D2240
Specific gravity	1.55	1.55	1.70	2.20	1.60	1.60	ASTM D792
Maximum use temperature (°C)	–60 to 200	–60 to 200	–60 to 200	–60 to 200	–60 to 200	–60 to 200	—
Volume resistivity (Ωcm)	10×10^{14}	10×10^{14}	10×10^{14}	2×10^{14}	10×10^{14}	10×10^{14}	ASTM D257

[a]Collected volatile condensable materials (0–10% acceptable).
[b]CHO-THERM 1671 is available up to 35 mils on custom orders.
[c]CHO-THERM 1661 is available up to 100 mils on custom orders.

Table 8.11. Calgraph Properties

Property	Units	Value
Electrical Resistivity		
"a" direction (parallel to surface)	Ohm-cm	0.0010
"c" direction (normal to surface)	Ohm-cm	0.064
Bulk Density	g/cm^3	1.1
Thermal Conductivity		
"a" direction (parallel to surface)	W/m·K	220
"c" direction (normal to surface)	W/m·K	6.9
Thermal Expansion		
21–980 °C		
(bulk density 1.7–1.9 g/cm^3)	10^{-6}/°C	5.0–7.9
Hardness (Shore Scleroscope)		
At 1.0 g/cm^3	—	30
At 1.3 g/cm^3	—	40
Tensile Strength		
At 1.0 g/cc and 0.015-in. foil	kPa	4800
Permeability		
Air	cm^2/g	<0.00001
Emissivity		
At 500°C	—	0.4
Sublimation Temperature		
(does not melt)	°C	3600
Temperature limit (in air)	°C	540

Welch and Ruttner[8.41] conducted a study to determine if Calgraph was a suitable interface filler for perimeter-mounted electronic units as large as 279 mm by 152 mm (Fig. 8.23). They divided the test plate into four regions as shown in Fig. 8.30. Using a TMM of the test setup and correlating test results to math-model predictions, they determined local heat fluxes and heat-transfer coefficients. A comparison of local heat-transfer coefficients so calculated for bare and Calgraph-filled interfaces at a torque of 2.26 N·m is shown in Table 8.12. Results are shown for cold plates at –34 and 71°C. Use of Calgraph improved heat-transfer coefficients in all regions except the center region. In that region, separation clearly has occurred, and pressure is essentially zero with or without the Calgraph. The largest improvement is seen in the screw region, where enhancement of a factor of 2.8 to 3.1 was observed. In the region between the screws and in the center-loop

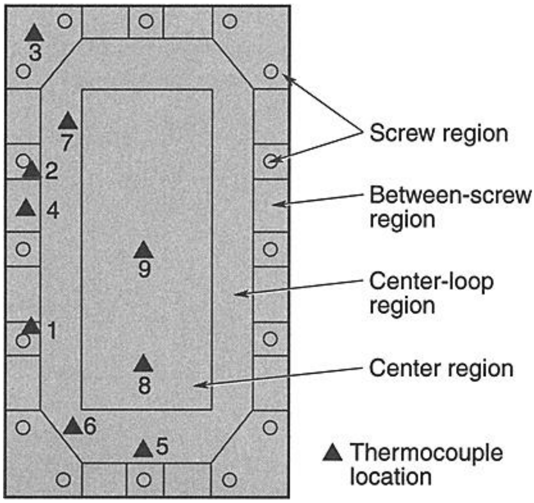

Fig. 8.30. Test plate showing thermocouple and region locations.[8.41]

Table 8.12. Local Heat-Flux Heat-Transfer Coefficients (W/m²·K) that Match Experimental Data for the 2.26 N·m Test

	Interface			
	Bare		Calgraph	
	Temperature (°C)		Temperature (°C)	
Region	–34	71	–34	71
Screw region	1420	2560	3980	7960
Between screws	850	850	1420	1135
Center loop	570	570	1135	1135
Center region	0.6	5.7	2.8	34

region, enhancement varied from 1.33 to 2.0, and in the large center region no enhancement was observed. Most investigators do not use TMMs, and they present their results as average heat-transfer coefficients based on an assumed uniform heat flux from top to bottom plate (e.g., Bevans *et al.*[8.35]). Therefore, Welch and Ruttner presented results in this form (Table 8.13). On this basis, enhancement by a factor of 1.5 to 1.9 was observed. Calgraph was also tested by Taylor on a small, stiff configuration.[8.40] An aluminum block 51 by 192 by 38 mm high was mounted to a 12.7-mm-thick aluminum plate by four No. 8-32 screws. Average heat-transfer coefficients reported were 14,800 W/m²·K and 4980 W/m²·K, with and without Calgraph, an improvement by a factor of three. This is the magnitude of improvement seen by Welch and Ruttner in the screw region.

Table 8.13. Area-Averaged Heat-Transfer Coefficients ($W/m^2 \cdot K$) Based on Uniform Heat-Flux Assumption

	Screw Torque (N·m)			
	1.13		2.26	
	Temperature (°C)		Temperature (°C)	
Region	–34	71	–34	71
Bare	284	369	330	398
Calgraph	511	705	506	705

Cured-in-Place RTV Silicone Compounds

Thermal gaskets provide a factor of 1.5 to 1.9 improvement on an overall basis for 7.94-mm-thick plates for a typical perimeter-mounting configuration, with the largest improvement in the region of the bolts. No improvement is found in the center region, a consequence of bowing of the plates. To avoid this problem and provide near-continuous contact between the two plates, cured-in-place RTV silicone compounds are widely used in the industry. A process specification kindly provided by TRW Inc. calls for surface cleaning and drying, use of primer (on both surfaces) or mold-release compound (on at least one surface), installation of a stainless-steel mesh screen with gold-plate finish (for grounding) to be engaged by the mounting hardware, application of torque, extrusion of filler material from at least 75% of the periphery of the mating surfaces (for coverage), and cure-in-place. Belleville washers can be used at each screw instead of the wire mesh to achieve grounding. Some contractors forgo the use of a primer to allow easy removal of the electronic unit.

Use of RTV compounds creates a mold that conforms to the profile of the cavity created between unit baseplate and mounting plate resulting from the action of bolt torque. Centerline gap caused by bowing can be on the order of 10 to 20 mils. A variety of RTV compounds are used. Choice depends on properties such as cure time, viscosity (low viscosity aids filler extrusion from between mating surfaces), and low volatility. A typical material is an RTV566 kit consisting of RTV566A and RTV566B, supplied by General Electric. Some contractors in their spacecraft applications use RTV compounds filled with thermally conductive particles.

For a small stiff configuration, Taylor[8.40] reported an average heat-transfer coefficient with RTV filler of 15,250 $W/m^2 \cdot K$, a factor of three greater than that for a bare interface. Bevans *et al.*[8.35] reported factors of four to six improvement for an average heat-transfer coefficient using RTV-11 for the configurations of Fig. 8.22. These results have been used by TRW in establishing the upper curve of Fig. 8.21. Overall, heat-transfer coefficients are in the range of 150 to 480 $W/m^2 \cdot K$.

Usage Recommendation for Filled Interfaces

For filled interfaces, a practice similar to that used for bare interfaces is recommended. Separate treatment should be used for the region near the bolt and for the plate. Near the bolt or for small stiff plates, as studied by Taylor, a factor of 2.5 to 3 improvement in heat-transfer coefficient over bare-interface values is justified for thermal gasket[8.40,8.41] and RTV filler[8.40] interfaces. Overall heat-transfer coefficients for large, thin plates with a perimeter-bolt pattern are considerably less for thermal-gasket filler than for RTV filler. This is a consequence of bowing and lack of gasket contact in the center region. For thin plates or honeycomb panels with thin facesheets, use of RTV filler is recommended—with the upper curve of Fig. 8.21 recommended for predictive purposes.

For thick plates with a perimeter bolt pattern, the data of Welch and Ruttner[8.41] can be used to determine heat-transfer coefficients for bare interfaces and those with a flexible graphite thermal gasket. On an overall basis the values in Table 8.13 can be used. In conjunction with a TMM analysis, the local values from Table 8.12 can be used. For thick plates employing RTV filler, a TMM analysis should be conducted using the Welch and Ruttner[8.41] Calgraph data of Table 8.12, except the center-region coefficients should be between 250 and 400 $W/m^2 \cdot K$.

Complex Configurations and Special Topics

Heat-Pipe Interfaces

Heat pipes are fluid-filled, wicked heat-transport components often used in spacecraft thermal control. They utilize capillary forces and latent heat in their operation, and their mechanical and thermal interfaces are an important input to the thermal design. They are discussed in more detail in Chapter 14.

Typical Interfaces

Typical heat pipe–payload integrations are shown in Figs. 8.31 through 8.33. Figs. 8.31 and 8.32 show schematics of heat pipes embedded into honeycomb panels. Such panels are constructed of high-thermal-conductivity facesheets and stiff honeycomb core. They can be utilized in the spacecraft interior or as direct radiators on the exterior. The facesheets withstand the bending loads and act as lateral conductance fins for the mounted unit (Fig. 8.31), while the core resists shear loads, provides stiffness, retains the component fastener, and provides low-level transverse conductance. The heat pipes are bonded to the interior surfaces of the

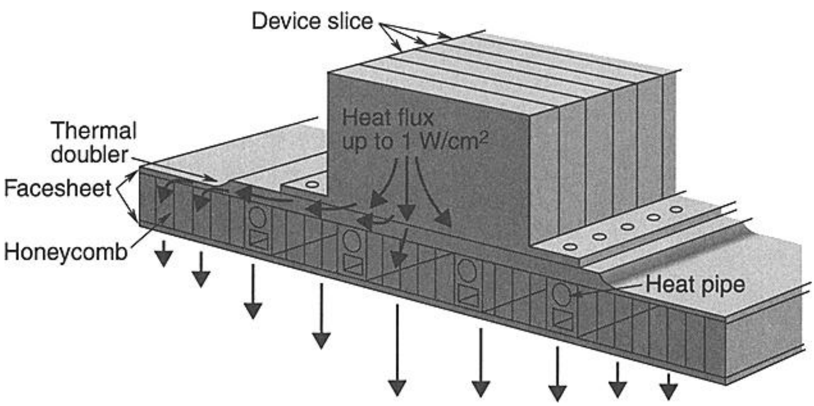

Fig. 8.31. Electronic unit mounted to honeycomb/facesheet panel with embedded heat pipes.

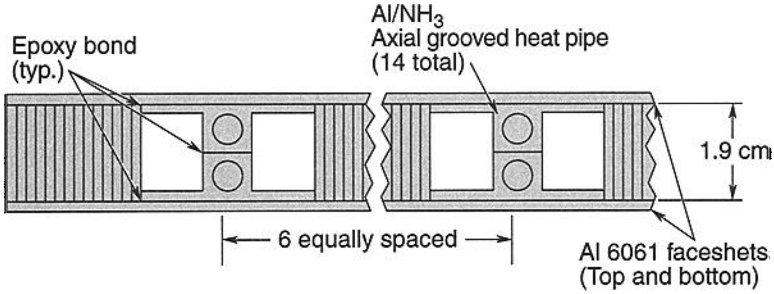

Fig. 8.32. Honeycomb/facesheet panel with embedded heat pipes.

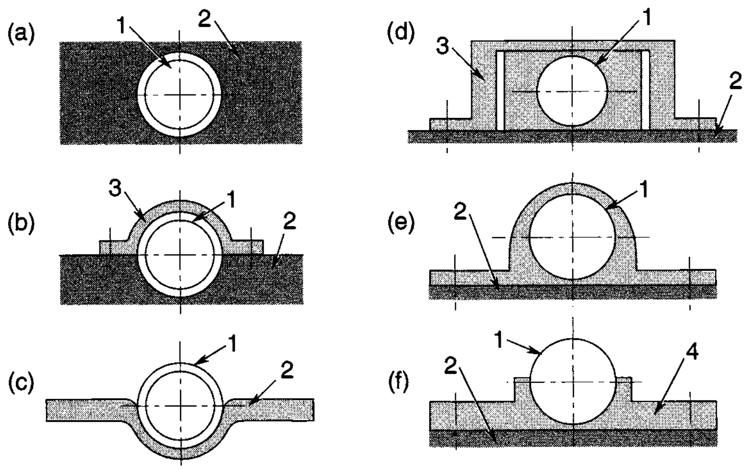

Fig. 8.33. Heat-pipe integration. 1: heat-pipe casing; 2: mounting surface of payload device; 3: saddles; 4: thick flange.[8.46]

facesheets; they provide lateral thermal conductance and, in some configurations (Fig. 8.32), transverse conductance by virtue of the casing. The heat pipes of Fig. 8.32 are bonded together and provide one-for-one redundancy.

Figure 8.33 shows six heat-pipe integration configurations. Configuration (a) is "buried" within the mounting. Mechanically the heat pipe is attached by threading or by virtue of a tapered casing (in detachable designs), glue, or low-temperature solder (in nondetachable designs). Configuration (b) uses a bolted saddle, while in configuration (c) the mounting is shaped to allow heat-pipe bonding. Configuration (d) shows an extruded rectangular-section heat pipe affixed by a saddle. Saddles for configurations (b) and (d) may be one continuous piece or multiple interrupted segments. Configuration (e) shows an aluminum heat-pipe extrusion with two integral flange ribs for mounting. Configuration (f) shows a stainless-steel or copper-casing heat pipe joined by low-temperature solder to a thick aluminum (sometimes copper) flange.

Design Guidelines

Each of the proposed heat-pipe interfaces of Fig 8.33 has its own thermal efficiency, which depends on flange thickness and layout of screws. Flange design may include thin flange ribs (thickness 1 to 2 mm) with M2.5 to M4 screws spaced from 12 to 40 mm, or thick ones (thickness 4 to 8 mm) with M4 to M8 screws or bolts spaced from 40 to 90 mm. Here European/metric screws are designated where, for example, M2.5 denotes a nominal 2.5-mm shaft diameter. The average area per bolt varies—for the first case 2 to 15 cm^2, for the second 10 to 40 cm^2. Sometimes the screw layout is nonuniform; screws can be allocated in groups of two or three with the closest possible spacing. The distance between such groups is two to four times greater than when uniform screw spacing is used. The thin-ribs flange design is more attractive for low heat density (up to ~0.5 to 1 W/cm^2), especially where such sources are distributed and nonuniform. The thick-ribs flange design is more reasonable for high-heat-density components (more than 1 W/cm^2) with linear extent greater than 10 cm. Stainless-steel bolts or screws are used as a rule for flange and payload-device connection. Contact conductance between flange and device can be estimated from recommendations made in the "Application of Theory: Contact Region" section.

Some Hardware Configurations

Examples of heat-pipe flange design are presented in Figs. 8.34 to 8.36. Figure 8.34 shows an extruded aluminum heat-pipe attachment to a spacecraft payload platform. The length of the flange is 325 mm, width 30 mm, and thickness 1.2 mm, with 42 M3 screws used. Maximum power transferred is 90 W.[8.47,8.48] Figure 8.35 shows a heat-pipe condenser-zone attachment to a device mounting plate. The heat pipe is made of copper with the device housing made of nickel-coated aluminum. The flange thickness is 10 mm with M8 bolts used. Nominal power transferred is 160 W.[8.49] Figure 8.36 shows two heat-pipe flanges for attachment to a device mounting plate. The heat pipes are made of stainless steel, the flange aluminum, coated with nickel. Flange lengths are 85 and 120 mm, and thicknesses are 2.2 and 3 mm, respectively. M3 screws are used and nominal power is 10 W.[8.50]

The heat pipe transports heat from the device, and a device heat-collecting zone must be part of the design as well. The most common way to collect and transport distributed heat is to exploit the thermal conductance of the device's structural elements. A heat-pipe variant that realizes this is presented in Fig. 8.37, a heat-pipe-device/spacecraft interface using a carbon-fiber, carbon-matrix (carbon-carbon, or

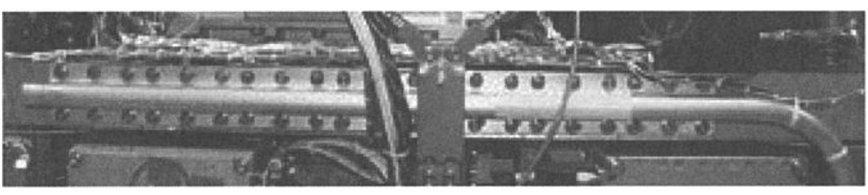

Fig. 8.34. Extruded aluminum heat-pipe attachment to payload platform.[8.47,8.48] (Courtesy of National Technical University of Ukraine NTUU, formerly Kyiv Polytechnic Institute)

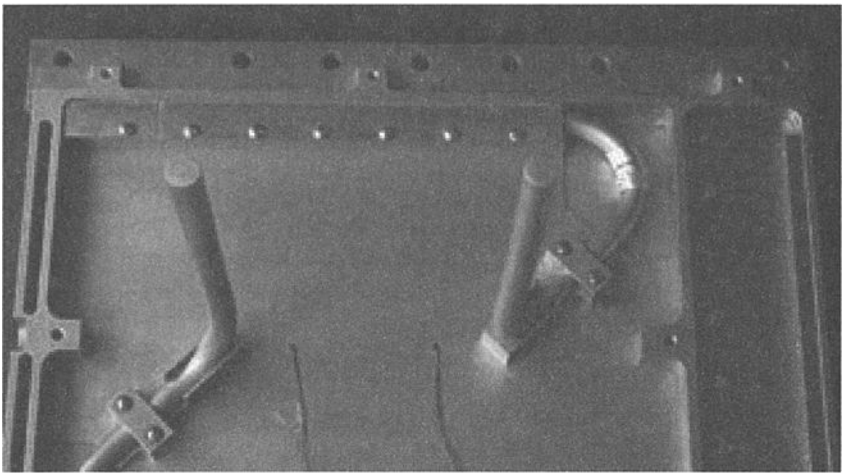

Fig. 8.35. Heat-pipe condenser zone attachment to device mounting plate.[8.49] (Courtesy of National Technical University of Ukraine NTUU, formerly Kyiv Polytechnic Institute)

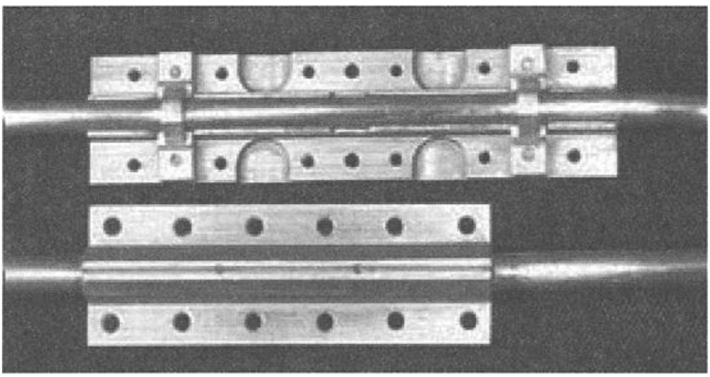

Fig. 8.36. Heat-pipe condenser zone attachment to device mounting plate.[8.50] (Courtesy of National Technical University of Ukraine NTUU, formerly Kyiv Polytechnic Institute)

CC) high-conductance layer as well as carbon-fiber/honeycomb (CF/HC) panels. Its size in-plane is 500 mm.[8.51]

Thermal Modeling Example

Temperature gradients and nonuniform heat flow are seen at the heat-pipe flange because of the discrete increments between heat pipes and the heat-flow processes in the heat-pipe casing. The influence of this temperature nonuniformity should be estimated beforehand numerically or analytically.[8.46,8.52,8.53] Finite-element software has been used for analysis of temperature gradients and heat flows for heat

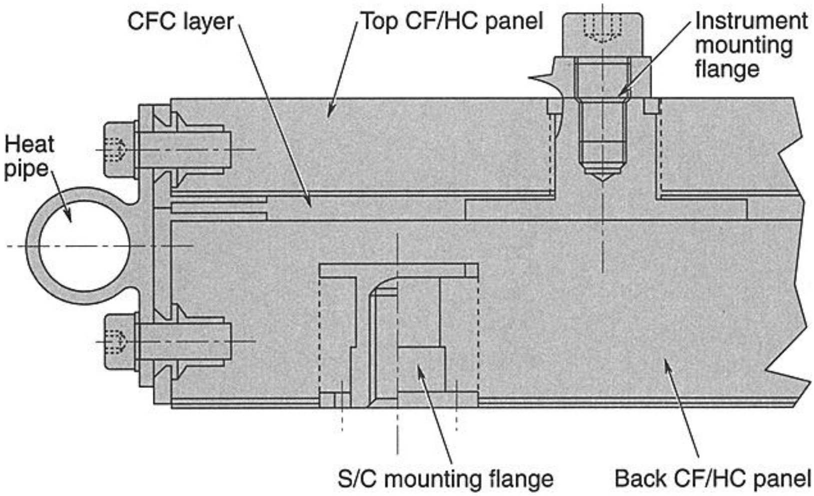

Fig. 8.37. Heat pipe–device interface showing usage of carbon-fiber, carbon-matrix (CFC) high-conductance layer.[8.51] (Reprinted with permission from SAE Paper No. 981639 ©1998 Society of Automotive Engineers, Inc.)

pipe–flange designs, and for heat-pipe integration into honeycomb panels.[8.53] As an example, the assembly shown in Fig. 8.38 was analyzed. A constant heat flux was applied to the aluminum doubler. Contact interfaces are located between the

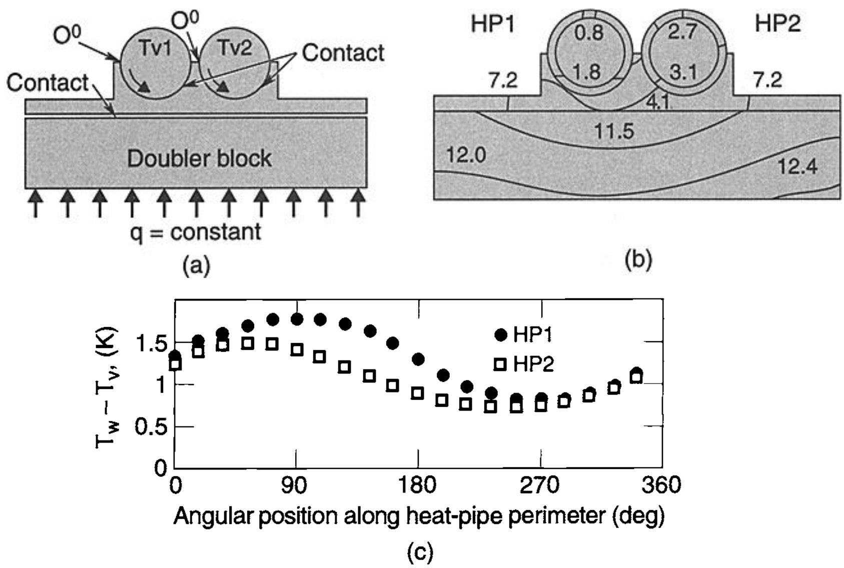

Fig. 8.38. Example of heat-pipe-assembly thermal prediction by finite-element method: (a) configuration and boundary condition; (b) temperature profiles; (c) wall-vapor temperature difference along heat-pipe perimeter.

doubler and the aluminum flange, and between the flange and the two copper heat pipes. The leftmost heat pipe, HP1, has an inner heat-transfer coefficient of 10,000 $W/m^2 \cdot K$ and vapor temperature of 0°C compared with 7000 $W/m^2 \cdot K$ and +2°C for HP2. Figure 8.38 shows temperature profiles in the heat-pipe assembly as determined by the finite-element analysis. In the figure the difference "wall temperature minus vapor temperature" is plotted as a function of angle along the perimeter of each heat pipe; here the angle is measured counterclockwise from the 0-deg locations shown in Fig. 8.38. Maximum temperature occurs along the bottom of the heat pipes in the region centered over the flange. The locations of minimal and maximal values are nonsymmetrical, as the heat flow to the pipes is unequal. Heat accepted by each heat pipe can be calculated by integration of temperature difference "heat pipe wall minus vapor" with respect to individual transfer coefficient. By dividing total heat to the bottom surface of the doubler by the difference in average temperature between this surface and that of the heat-pipe vapor, the conductance of the assembly as a whole is determined.

Special Configuration: Saddle with Two-Step Assembly

A novel saddle design by C. Gerhart[8.54] is shown in Fig. 8.39. This design allows independent assembly of the saddle to the heat pipe and then the saddle/heat-pipe assembly to the mounting plate. The two-step bolting/assembly process, intrinsic to this design, provides the potential for better fit, and higher and more uniform clamping pressure.

Compound-Cylinder Interface

In some engineering applications, the requirement for a cylindrical interface as in Fig. 8.40 may arise. For example, an annular heat exchanger could be mounted concentrically to the condenser section of a heat pipe. Contact pressure, which was a key determinant of contact conductance for flat interfaces, can no longer be explicitly determined. This pressure depends on a number of parameters including

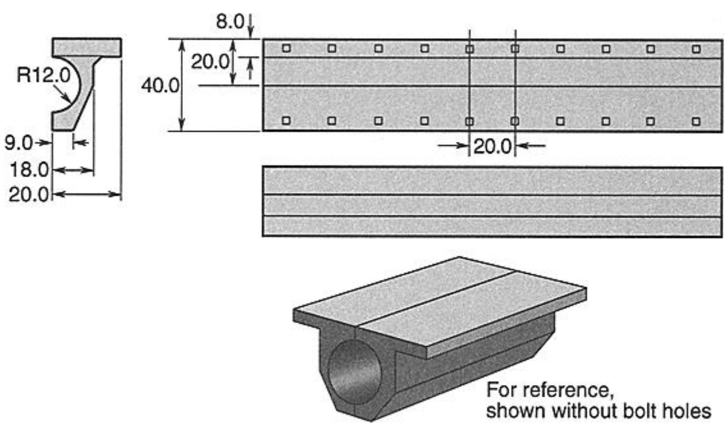

Fig. 8.39. Saddle with independent bolting to heat pipe and mounting (dimensions in mm).[8.54]

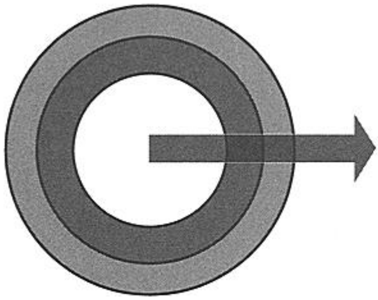

Fig. 8.40. Heat flow through a compound cylinder.

initial fit, differential expansion of the cylinders, and heat flux. In addition to these parameters, contact conductance depends on geometry, surface characteristics, interface medium, and thermomechanical properties of the cylindrical materials. Ayers *et al.*[8.55] have reviewed studies on this subject; they find the field to be in need of additional work. They provide an empirical correlation for eight different material/medium groupings—five in air and three in vacuum, including two where the inner cylinder is aluminum and the outer stainless steel:

$$h^* = 81.8(F^*)^{0.685} \tag{8.28}$$

where

$$h^* = h\sigma_E/k_E m_E \tag{8.29}$$

and

$$F^* = (F\alpha_E R_E/k_E)(E_E/H_E)(\alpha_i/\alpha_o)^3[0.5(1 + P_{amb}/P_{atm})]^2. \tag{8.30}$$

Ambiguity was present in the definition of mean or effective value as used by Ayers *et al.*[8.55] The roughness, σ_E, elasticity, E_E, and hardness, H_E, were called the "effective" value, but not explicitly defined. The asperity slope, m_E, thermal conductivity, k_E, and the coefficient of thermal expansion, α_E, were called the "effective (geometric mean)" value. The most likely meaning of the various terms is believed to be as follows: $\sigma_E = \sigma = (\sigma_i^2 + \sigma_o^2)^{1/2}$, where the subscripts denote the inner and outer surfaces; E_E is given by E' of Eq. (8.3); $H_E = H_C$, the microhardness of the softer of the two surfaces; $m = (m_i^2 + m_o^2)^{1/2}$; and $\alpha_E = (\alpha_i^2 + \alpha_o^2)^{1/2}$. While most probably $k_E = (k_i^2 + k_o^2)^{1/2}$, k_E is usually defined as the harmonic mean, i.e., $k_E = 2k_i k_o/(k_i + k_o)$. The term P_{atm} is sea-level atmospheric pressure, and P_{amb} is local ambient (e.g., vacuum) pressure.

Thermal Doublers

Introduction

For electronic units where power dissipation per unit surface area is large, excessive temperatures can occur if heat is directly conducted from the baseplate to the spacecraft mounting plate. This is especially likely if the thermal resistance between baseplate and mounting plate is large. Temperatures can be reduced if a high-conductivity heat spreader is used between the unit and the heat sink. Such spreaders, or thermal doublers, function by conducting heat laterally from high-power dissipation regions before final transport to the spacecraft mounting plate.

Analysis

Bobco and Starkovs[8.56] analyzed a rectangular doubler of uniform thickness (Fig. 8.41). Starkovs[8.57] expanded the analysis to include two heated footprints on a rectangular doubler (Fig. 8.42), while Bobco[8.58] analyzed various types of terraced doublers (Fig. 8.43). Bobco and Starkovs[8.56] developed and solved the equation

$$k\delta_o(\partial^2 T/\partial^2 x + \partial^2 T/\partial^2 y) - h(T - T_\infty) = -q(x, y), \tag{8.31}$$

which accompanies Fig. 8.41. The term T_∞ is the equivalent sink temperature of the environment about the baseplate, and h is the overall heat-transfer coefficient from the baseplate to the sink. In this formulation, the doubler is assumed to be sufficiently thin so that no temperature gradient exists in the z direction. Not included in the above three analyses is the additional contact interface associated with use of a doubler.

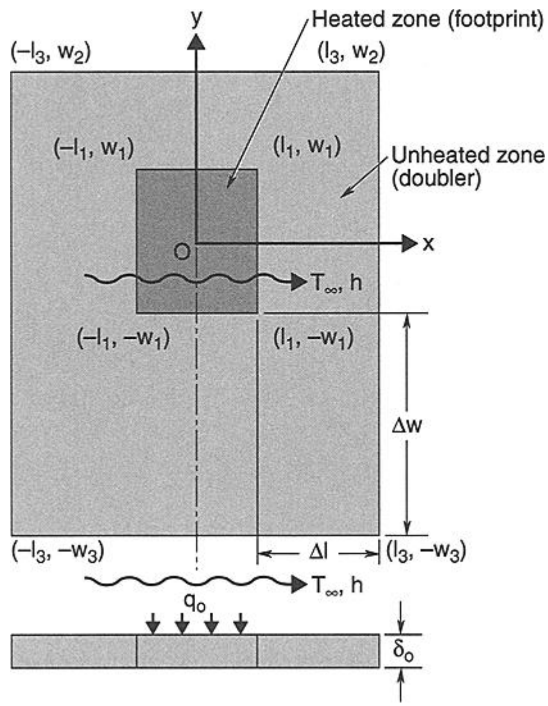

Fig. 8.41. Schematic of thermal doubler with single symmetry.[8.56]

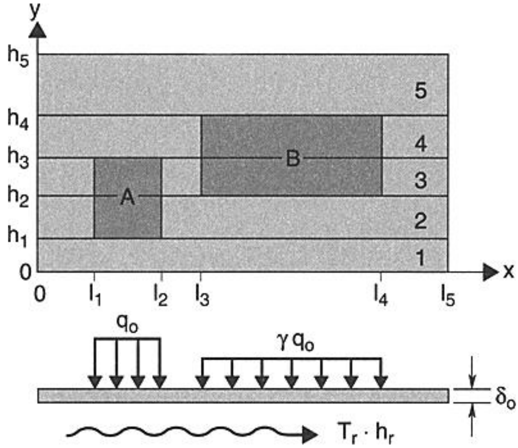

Fig. 8.42. Schematic of a rectangular doubler with two heated footprints.[8.57]

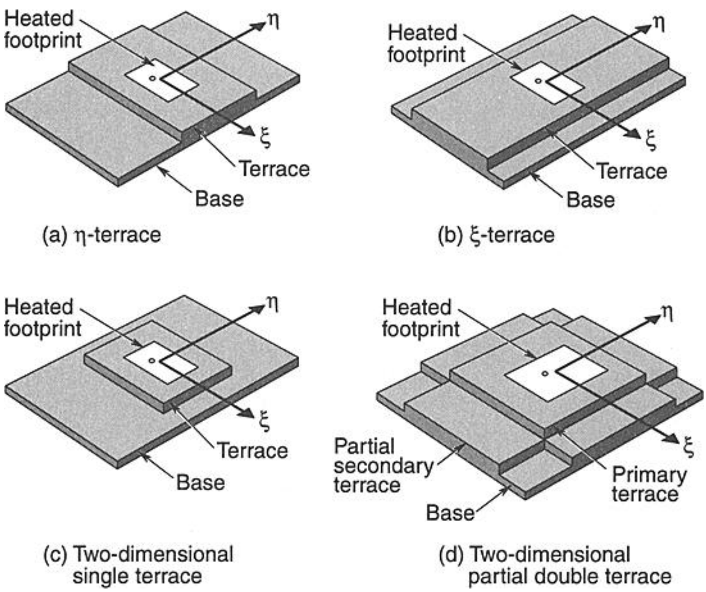

Fig. 8.43. Four terraced-doubler configurations that allow closed-form, separable solutions.[8.58]

Considerable analytic results were obtained in these three investigations. Typical results are shown in Figs. 8.44[8.56] and 8.45.[8.57] Bobco and Starkovs[8.56] point out that thermal-doubler design is an intricate task involving constraints of unit baseplate area, available mounting-plate area, and the surrounding environment.

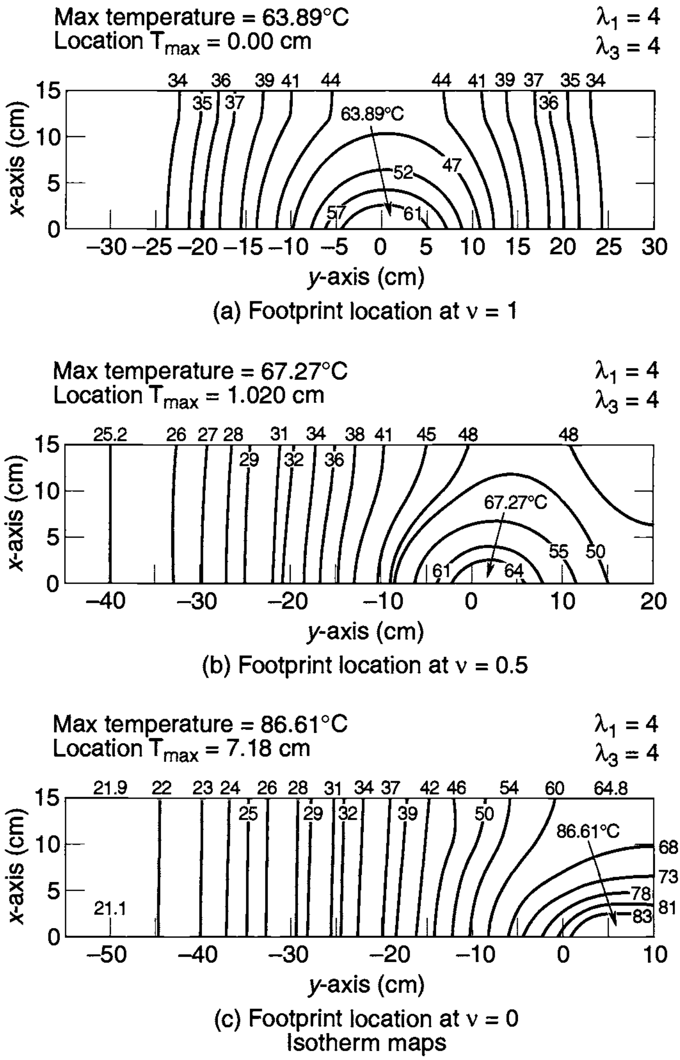

Fig. 8.44. Typical results for a single footprint.[8.56]

The intent is to provide the lightest-weight practical doubler design consistent with these constraints that satisfies the maximum-allowable unit-temperature requirement. Analytic solutions should be confirmed by finite-difference or finite-element TMM results.

For an axisymmetric doubler (Fig. 8.46), Gluck and Young[8.59] relieved the assumptions of no vertical temperature gradient in the doubler and no contact resistance between the doubler and baseplate. Here k is thermal conductivity, h is the contact heat-transfer coefficient, $f = T - T_o$, T is temperature within the doubler,

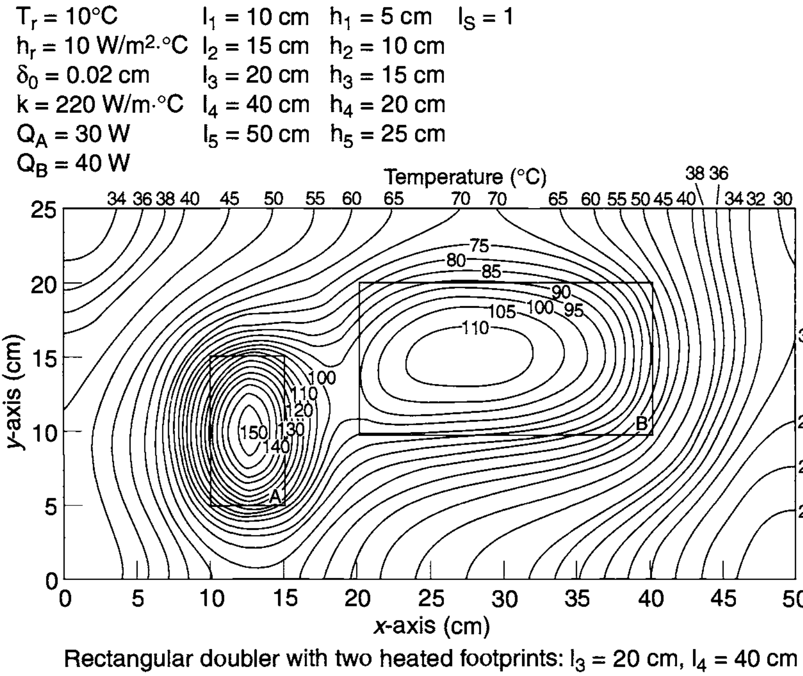

Fig. 8.45. Typical results for two footprints on a rectangular doubler.[8.57]

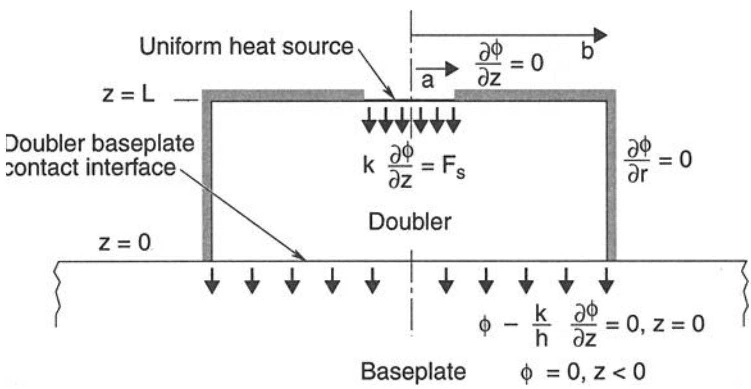

Fig. 8.46. Axisymmetric doubler model from Gluck and Young.[8.59]

and T_o is the baseplate (sink) temperature. For this problem, formulation of an optimum doubler thickness results, beyond which unit temperature increases (Fig. 8.47), where $\psi = k\phi/(2aF_S)$. This is a consequence of the combined effects of increased spreading (which reduces the temperature rise across contact interface)

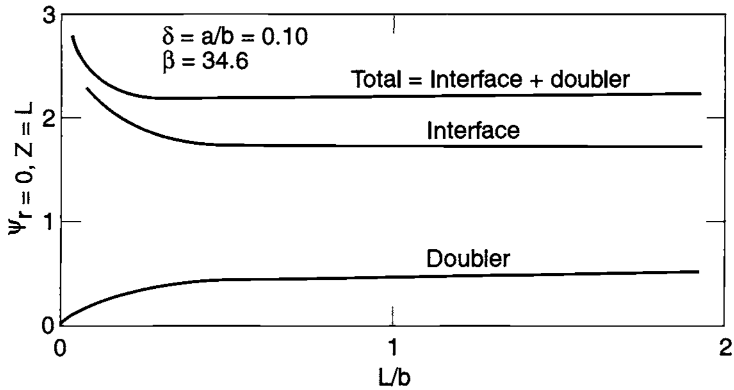

Fig. 8.47. Dimensionless centerline temperature rise at top of doubler vs. doubler height.[8.59]

and increased doubler thermal resistance with doubler thickness. Results are governed by an inverse Biot-like group, $\beta = k/hb$, as shown in Fig. 8.48(a). Here δ is a/b, the ratio of the heat-source radius to the doubler radius. For small values of β heat flow tends to be columnar (no spreading), and for large values heat flow diffuses radially (perfect spreading). The term F_o is the average heat flux across the cross section. Performance results are presented in Fig. 8.48(b), (c), and (d), where ϕ and ψ are the centerline values at $z = L$. For $L/b = 0.01$, columniation is noted for $\beta < 10^{-2}$, and nearly perfect diffusion is noted for $\beta > 10^2$. As L/b increases, the columnar region diminishes. At $L/b = 1.0$ columniation and diffusion are of the same order for $\beta < 10^{-2}$. Figure 8.48(e) and (f) present optimization results. The former presents a plot of the minimum value of $\psi_{r=0,\ z=L}$ versus β for eight values of δ. The latter presents the values of L/b that correspond to these minimum values.

Materials

Technological breakthroughs in the last decade have resulted in new composite materials with thermal conductivities several times higher than that of copper, together with low densities and coefficients of thermal expansion (CTEs) close to those of semiconductor electronic materials. These new materials can be divided into four classes:[8.60-8.63]

- polymer matrix composites (PMCs)
- metal matrix composites (MMCs)
- ceramic matrix composites (CMCs)
- carbon/carbon composites (CCCs)

Properties of some new composites are presented in Table 8.14 together with properties of commonly used materials. Because composite properties are usually anisotropic, values are given for the x, y (in the plane of the material), and z (through the thickness) directions. One figure of merit for these materials is the conductivity divided by the density, which gives an indication of relative weights of doublers that are made of different materials but provide the same overall

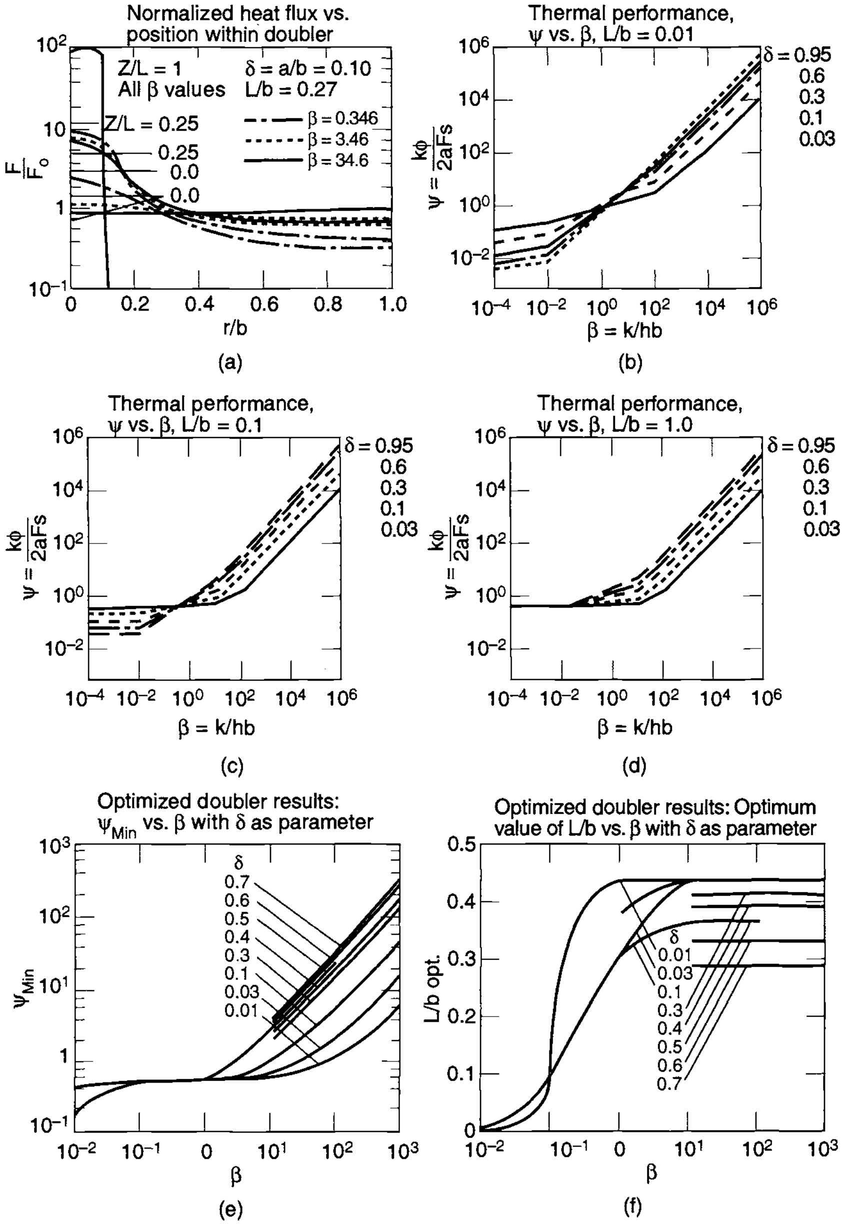

Fig. 8.48. Doubler performance.[8.59]

Table 8.14. Properties of Materials Used as Doublers and Heat Spreaders

Matrix	Reinforcement†	Thermal Conductivity	Density	Relative Performance[a]	CTE	Ref.
		Basic Materials				
Aluminum	none	230 (W/m·K)	2.9 (g/cm^3)	1.0	23 (ppm/K)	8.60
AlN	none	140–220	3.3	0.5–0.8	4.5	8.60
AlSiC	none	180		—		8.64
BeO	none	250	2.9	1.1	7.6	8.60
Silicon	none	150	2.3	0.8	4.1	8.61
Epoxy	none	1.7	1.2	0.02	54	8.61
Kovar	none	17	8.3	0.03	5.9	8.61
Copper	none	400	8.9	0.6	17	8.60
W-10Cu	none	167	16.6	0.1	6.5	8.60
Woven carbon fiber 1D 2D	none	350 (x) 175 (x/y)	<1.85	2.4 (x) 1.2 (x,y)		8.62
Pyrolytic graphite (material has minimal structural integrity)	none	1200 (x/y), 10(z)	2.2	6.9 (x,y), 0.06 (z)	−1.0(x/y); 20(z)	8.62
Annealed pyrolytic graphite	none	1700 (x,y), 10(z)		—		8.64
		Polymer Matrix Composites				
Epoxy	K1100 Carbon Fiber	300 (x/y)	1.8	2.1	−1.1	8.61
Polymer	K1100 Discontinuous Carbon Fiber	20 (x/y)	1.6	0.2	4–7	8.61
Polymer Matrix Composite (PMC) 1D 2D		600 (x) 300 (x/y)	1.65	4.6 2.3		8.62
		Metal Matrix Composites				
Aluminum	2D Fabric1	280 (x/y)	2.3	1.5	2.8	8.60
Aluminum	3D Fiber Mat1[b,c]	187 (x/y), 74 (z)	2.5	0.9 (x/y), 0.4 (z)	10.4	8.60

Table 8.14. Properties of Materials Used as Doublers and Heat Spreaders *(Continued)*

Matrix	Reinforcement†	Thermal Conductivity	Density	Relative Performance[a]	CTE	Ref.
Aluminum	3D Fiber Mat2[b,c]	226 (x/y), 178 (z)	2.3	1.2 (x/y), 1.0 (z)	5.5	8.60
Aluminum	MMCC 3D-2[b,c]	222 (x/y), 100 (z)	2.3	1.2 (x/y), 0.5 (z)	5.0	8.60
Aluminum	MMCC 3D-1[b,c]	189 (x/y), 136 (z)	3.1	0.8 (x/y), 0.6 (z)	6.0	8.60
Aluminum	K1100 Carbon Fiber	290 (x/y)	2.5	1.5 (x/y)	6.5	8.61
Aluminum	Si Particle	126-160(x,y,z)	1.9	0.8–1.1	6.5–13	8.61
Aluminum	SiC Particle	120-170(x,y,z)	3.0	0.5–0.7	6.2–7.3	8.61
Beryllium	Beryllia Particle	240(x,y,z)	2.6	3.0	6.1	8.61
Copper	+/–2^0SRG[b]	840(x), 96(y), 49(z)	3.1	3.4 (x), 0.4 (y), 0.2 (z)	–1.1(x) 15.5(y)	8.60
Copper	+/–11^0 SRG[b]	703(x), 91(y), 70(z)	3.1	2.9 (x), 0.4 (y), 0.3 (z)	-1.3(x) 15.5(y)	8.60
Copper	+/–45^0 SRG[b]	420(x), 373(y), 87(z)	3.1	1.7 (x), 1.5 (y), 0.4 (z)	1.2(x) 3.6(y)	8.60
Copper	0^0, 90, 0^0 [b]	415(x), 404(y), 37(z)	3.1	1.7 (x), 1.6 (y), 0.2 (z)	5.3(x) 5.4(y)	8.60
Copper	2D Fabric2	342(x), 335(y), 84(z)	5.6	0.8 (x), 0.8 (y), 0.2 (z)	2.7(x) 3.3(y)	8.60
Copper	K1100 Carbon Fiber	400 (x/y)	7.2	0.7 (x,y)	6.5	8.61
Tungsten	Copper	167 (x/y/z)	16.6	0.1	6.5	8.61
Molybdenum	Copper	184 (x/y/z)	10.0	0.2	7.0	8.61
Aluminum	Beryllium	210 (x/y/z)	2.1	1.3	13.9	8.61
Silver	Invar	153 (x/y/z)	8.8	0.2	6.5	8.61
		Carbon-Carbon Composites				
Carbon	K1100 Carbon Fiber	350 (x/y)	1.9	2.3 (x,y)	–1.0	8.61

Table 8.14. Properties of Materials Used as Doublers and Heat Spreaders *(Continued)*

Matrix	Reinforcement†	Thermal Conductivity	Density	Relative Performance[a]	CTE	Ref.
Carbon	Carbon Fibers (in x direction)	800 (x), 50(y/z)	1.85	5.5 (x), 0.3 (y/z)	–0.05 (x/y),	8.62
	Carbon Fiber (in x and y directions)	350 (x/y), 40(z)		2.4 (x,y), 0.3 (z)	5–7 (z)	
Carbon	Carbon Fibers (in x direction)	800(x), 50(z)	1.8	5.5 (x), 0.3 (z)	−1.5 (x/ y),	8.62
	Carbon Fiber (in x and y directions)	550(x/y), 40(z)		3.9 (x/y), 0.3 (z)	5–7(z)	

[a]Conductivity/density, relative to aluminum.

[b]Metal infiltration performed by Metal Matrix Cast Composites (MMCC) Inc.

[c]CTEs for reinforced composite with continuous fibers are in-plane isotropic values.

heat-transport capability. Such a figure of merit, normalized to that of aluminum, is given in Table 8.14.

Doublers for use under electronics boxes or as heat-conduction planes behind circuit cards can be made of composite materials having conductivities greater than that of copper, with a density of 2–3 g/cm^3 and a CTE value near to that of silicon. These characteristics allow the design of doublers with mass, size, and performance resulting in effective technical solutions to some heat-spreading problems. Of course, some effort is required to match mounting interfaces between the doubler and heat source to account for the layout of holes and insets, contact-conductance adjustment, and so on.

A different kind of composite, pyrolytic graphite encased in aluminum, copper, graphite epoxy, or AlSiC, is available under the trade name TC1050. This material, properties of which are shown in Table 8.15, has been used in aircraft applications. It provides an in-plane conductivity of 1700 W/m·K and a through-thickness conductivity of 10 W/m·K. Additional experimental work has been done with pyrolytic graphite encased in AlSiC.[8.64] In an application with two heat sources of 128 W mounted on a square (15 × 15 cm) spreader of such a composite, an effective conductivity of 860 W/m·K, a CTE of 8.1 ppm/K, and an effective density of 2.6 g/cm^3 were achieved. A similar disk-shaped doubler (diameter about 10 cm) had effective conductivities of 740 W/m·K (x/y) and 360 W/m·K (z) with a CTE of 8.1 ppm/K and an effective density of 2.6 g/cm^3. Some spacecraft programs have been hesitant to use encased pyrolytic graphite because of concerns that in-plane cleavage of the graphite could reduce through-thickness conductivity. Proper design, however, can minimize this risk.

Thermal Doubler/Heat-Pipe Synergy

Another way to further improve the efficiency of a doubler is to exploit the very high conductance of a heat pipe to spread heat over the doubler's surface. The heat pipe can be manufactured as a "flat plate,"[8.65,8.66] replacing the doubler structure

Table 8.15. Encapsulated Graphite Properties

Case Material	Core Material	Thermal Conductivity	Density	Relative Performance[a]	CTE	Ref.
AlSiC	Annealed pyrolytic graphite	740(*x*,*y*) W/ m·K	2.6 g/cm^3	3.6 (*x*,*y*)	6.8 ppm/K	8.64
Aluminum 6061, OFHC copper, graphite fiber/Polymer, or AlSiC	Pyrolytic graphite	1700(*x*,*y*), 10(*z*)	< 2.8 (unless copper casing used)	7.7 (*x*,*y*), 0.05 (*z*)	−1 to 24, depending on encapsulant	8.63

[a]Conductivity/density, relative to aluminum.

entirely, or as a conventional cylindrical pipe that can supplement the doubler by virtue of very high longitudinal conductance along the heat pipe's axis. To illustrate the synergy of heat-pipe/doubler combinations, parametric studies were performed using the configuration and boundary conditions of Fig. 8.45 as the baseline case. The four configurations studied were (Fig. 8.49): (1) the baseline case with a doubler conductivity of 220 W/m·K; (2) a case in which the conductivity of the doubler was increased to 1000 W/m·K; (3) a case where the doubler is a flat-plate heat pipe (inner heat-transfer coefficient is 2000W/m^2·K); and (4) a study where a heat pipe with a 1-cm width was embedded in the doubler material. Temperatures on the doubler external side, predicted by finite-element analysis, are plotted against x-axis position in Fig. 8.49. The figure shows that configurations (2), (3), and (4) reduce the maximum temperature by more than 40°C. The most effective configuration is the flat-plate heat pipe, case (3), which produces a nearly uniform temperature over the doubler surface.

Combined Thermal and Structural Analysis

An example of a combined thermal and structural analysis was previously discussed with regard to the work of Roca and Mikic.[8.28,8.29] More recently, finite-element codes have been used to conduct such analyses. Layton[8.68] conducted a thermal/structural study of a traveling wave tube (TWT) using ABACUS and NASTRAN, with PATRAN used for graphical display. As part of that analysis, local heat-transfer coefficients were determined between the TWT baseplate and the cold plate to which it was mounted. Fastening was accomplished by the use of two screws through a flange on one side of the TWT. Both surfaces were assumed to be perfectly flat and smooth. Computed pressure profiles and heat-transfer coefficients (W/cm^2·K) are shown in Figs. 8.50(a) and (b). The highest pressures are observed nearest each of the bolts, while pressure decreases to nearly zero at some

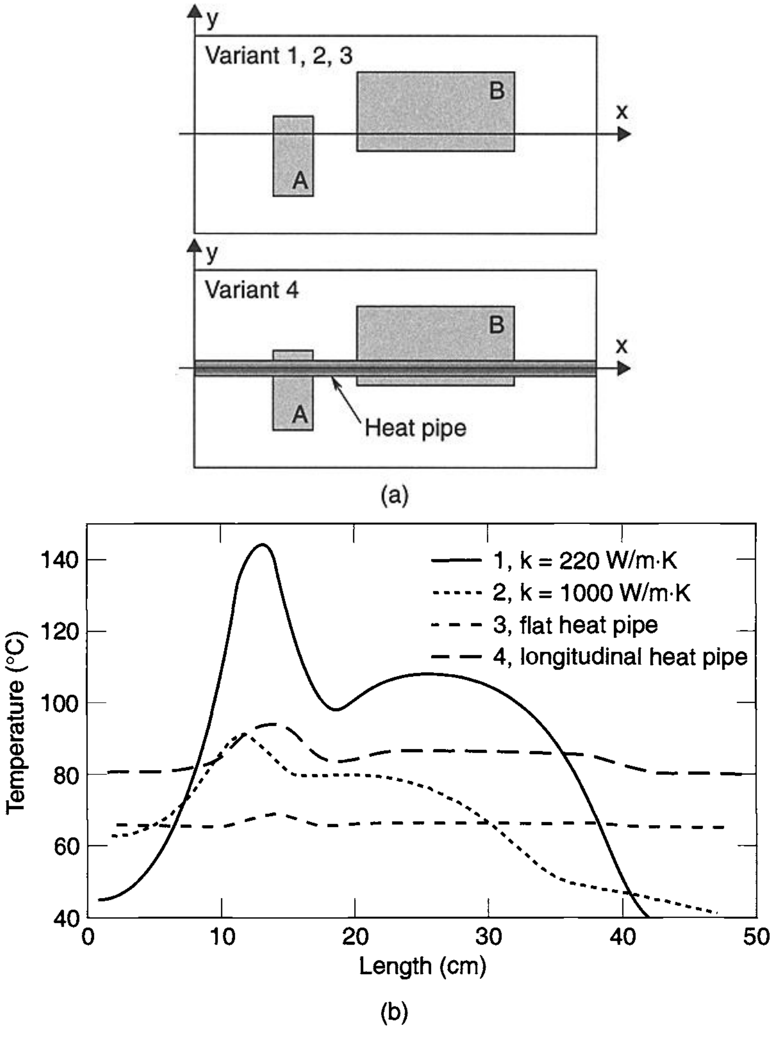

Fig. 8.49. Comparison of several doubler–heat pipe configurations/technologies: (a) schematics of doubler–heat pipe with two heat sources, A and B; (b) temperature profiles along x-axis for design variants 1, 2, 3, 4.

distance away. Layton characterized the local heat-transfer coefficient as a function of pressure from the work of Swartz[8.24] (Fig. 8.11) and others. He used the integration method of Goit[8.69] and a multivariable interpolation routine to determine from the pressure profile average heat-transfer coefficients for each element. Welch and Hamada[8.70] have compared heat-transfer coefficients using ABACUS finite-element analysis with those determined from finite-difference analysis and from experimental results. The basis for the comparison was the study by Welch

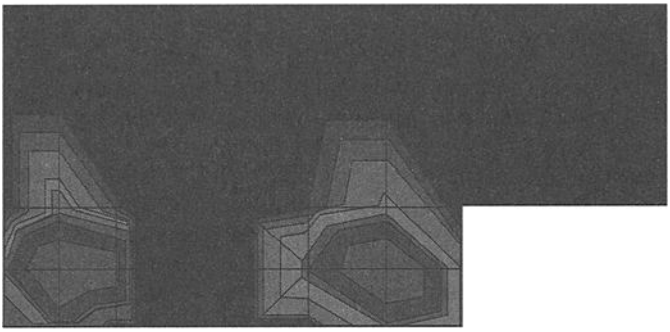

(a) Pressure profiles

0.073	0.071	0.074	0.070	0.067	0.070	0.074	0.070	0.069	0.065	0.065
0.149	0.159	0.076	0.078	0.076	0.070	0.143	0.137	0.070	0.070	0.065
0.84	1.12	0.47	0.082	0.083	0.22	0.79	0.66			
1.00	1.17					0.80	0.64			

(b) Local heat-transfer coefficients ($W/cm^2 \cdot K$)

Fig. 8.50. Finite-element thermal/structural analysis result from Layton.[8.68]

and Ruttner[8.41] as reported here (Figs. 8.23 and 8.30; Tables 8.8, 8.12, and 8.13). Figure 8.51 shows pressure profiles for a preloaded (torque applied to screws) plate at ambient temperature. Welch and Hamada analytically confirmed the previously noted[8.42,8.43] effect of plate temperature on a bolted-joint heat-transfer coefficient. As expected, the different CTEs of the aluminum alloy plates and stainless-steel screws increased or decreased contact pressure as plate temperature was, respectively, above or below ambient temperature. At the lowest torque used, 1.13 N·m, the predicted contact pressure was 393, 1965, and 3378 kN/m^2 for temperatures of –34°C, ambient, and 71°C.

Heat-transfer coefficients in the screw region differed greatly depending upon whether they were determined from finite-element analysis, finite-difference analysis, or test data. They were greatest from finite-element analysis and least from test data, with the difference as much as a factor of 15. However, these differences were largely a result of the different contact-region area used in the three methods. The finite-element analysis, which arguably uses the most correct contact area (because the area is determined from pressure profiles), used the smallest contact area—roughly three times the screw diameter. The test data was reduced using "region" areas—relatively large (and unverifiable) contact areas. A fairer comparison of the finite-element and finite-difference analyses is based on conductance (heat-transfer coefficient multiplied by the applicable area for each analytic or data-reduction method). The conductances so obtained showed relatively good agreement.

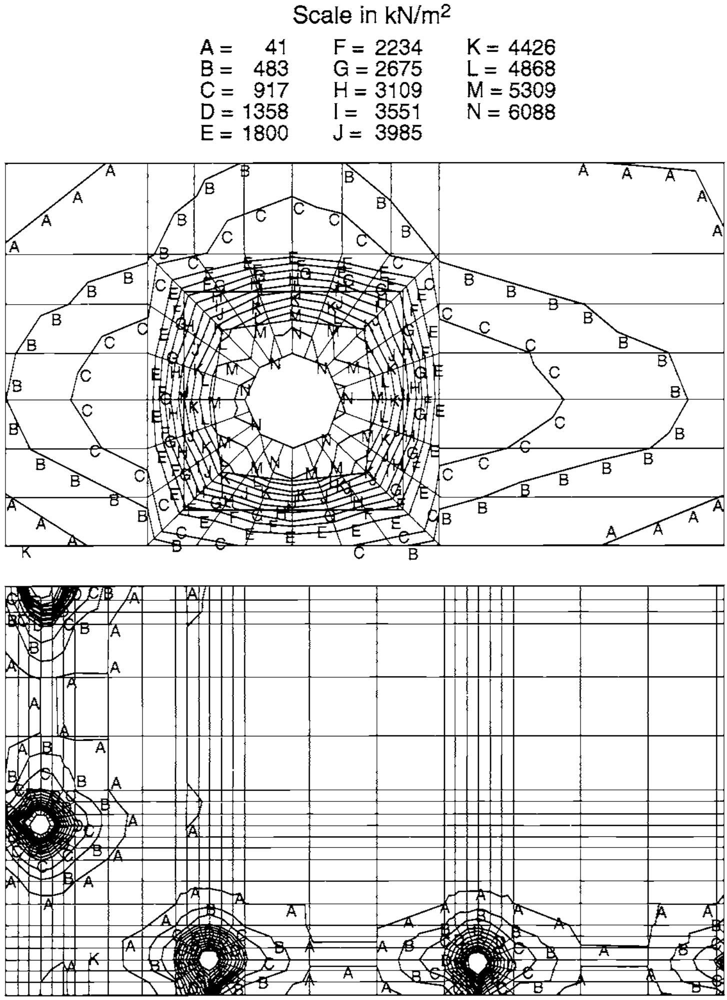

Fig. 8.51. Pressure profiles in kN/m^2 (kPa) for preloaded plates at ambient pressure.[8.70] (Reprinted with permission from SAE Paper No. 961504 © 1996 Society of Automotive Engineers, Inc.)

Mechanically Compliant Joints

In general, joints provide a mechanical attachment and a thermal path with specific heat-flow and temperature requirements. In many cases the thermal path must have mechanical flexibility to connect in three dimensions to coupling points or surfaces; such thermal paths may also require high thermal conductance with minimal mechanical loads and torque on the device. Such flexible or compliant joints are often used to provide vibration isolation, relieve stress caused by CTE mismatches, or accommodate sliding applications. They are often found in CCD modules, heat-storage modules, and sensors and focal-plane assemblies for optical cameras and telescopes. These compliant thermal paths can be manufactured from a variety of high-conductivity materials such as copper, aluminum, beryllium, silver, or carbon fibers. The choice of material is dictated by thermal conductivity, geometrical flexibility, and workability of the soldering/welding/gluing process. Properties of candidate materials are presented in Table 8.16.

Flexible Straps

A typical flexible thermal strap consists of flexible strips, cable braid, or several braids in parallel, with lugs at each end for attachment. One of these attachments can be to a device sensitive to mechanical loads. In Fig. 8.52 is the flexible strap used in the VEGA Project[8.50,8.75] (Soviet Union, 1986), which connected a CCD matrix cooling finger with a heat pipe. This thermal strap conducted 0.5 to 1.0 W with an overall resistance of 14°C/W. It had a mass of 40 g, a length of 120 mm (the length of the flexible part was 80 mm), an external-braid diameter of 8 mm, a 180-deg bend capability, a force to bend 90 deg of 2 N, and a twist range along longitudinal axes of 20 deg.

Figure 8.53 presents two variants of flexible interfaces having an overall thermal resistance of 0.7°C/W and intended for heat transfer at higher power (up to 10 W). The heat-absorbing flange is attached to the device being cooled, and the heat-removal flange is connected to the cooling system. The variant on the right is characterized by

Table 8.16.[a] Typical Properties of Materials for Fabrication of Flexible Thermal Straps[8.71–8.74]

Material	Density (kg/m^3 at 20°C)	Conductivity (W/m·K at −100 and 20°C)	Heat Capacity (J/kg·K at −100 and 20°C)	Typical Forms	Enlongation/ narrowing (%)	Strap Resistance/ mass[b] [(K/W)/g]
Copper	8920	413/398	340/385	fibers, strands, strips	53/46 74/65	2.5/90
Aluminum, >99.75% pure	2700	220/218	500/885	strips	43/44 84/90	4.5/27
Beryllium	1840	—/157	—/1674	strips	-	6.5/19
Silver	10,493	389/376	219/230	strips	-	2.4/100
Amoco P100 carbon fiber	2160	—/550	—/—	strands, strips		1.8/22

[a]

[b]Calculated values for a 10-cm-long strap with an effective cross section 1 cm^2, without end clamps.

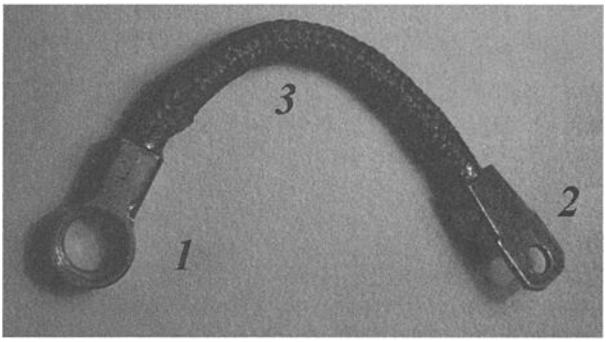

Fig. 8.52. Photo of flexible strap: (1), (2) connectors; (3) flexible copper braid.[8.50,8.75]

brazing of the braid strap to the cooling-system heat pipe to minimize the overall thermal resistance.[8.76] This design, which has a mass of about 60 g and distance between heat-exchanging surfaces of 25 mm, consists of 32 braids, each with a 3-mm diameter. The movement of the heat-absorbing flange is ±5 mm, and the allowable rotation along the longitudinal axis is about 20 deg. An important note is that the seepage of liquid solder into the gaps between fibers must be prevented during manufacture in order to assure flexibility.

The thermal resistance, R, of a flexible strap can be estimated based on the one-dimension conduction equation:

$$R = \Delta L^{*}\eta/(A^{*}k), \tag{8.32}$$

where ΔL is the measured length of the braid, η is a coefficient relating the real heat-transfer length of threads with ΔL, A is the area, and k is the thermal conductivity. The coefficient, η, should be defined experimentally.

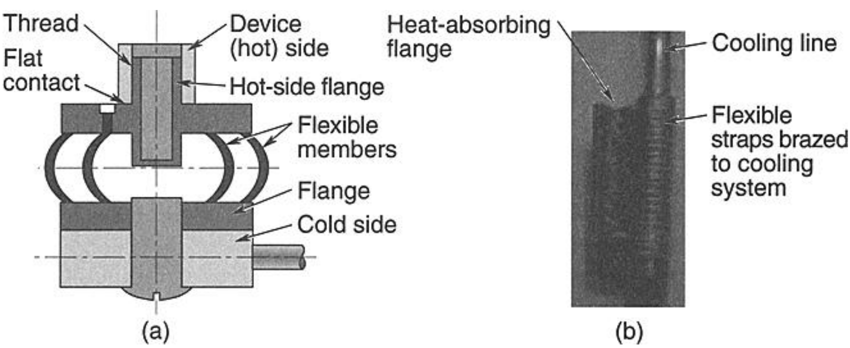

Fig. 8.53. Two variants of flexible interfaces.[8.76] (Courtesy of National Technical University of Ukraine NTUU, formerly Kyiv Polytechnic Institute).

Figure 8.54 shows two examples of cascaded flexible heat-transfer straps[8.77] with a thermal resistance of about 3°C/W. The schematic drawing shows the two flexible straps in series fabricated as copper braids and copper strips, while in the photo only the copper braids can be seen. With these straps, the optical device is controlled over the narrow temperature band of 7 to 17°C. The use of a solid stiff thermal interface in this case was unacceptable because of the inability to adjust the focal-plane location relative to the optics.

Some other thermal-strap variants, developed by Dornier GmbH (Germany) for the Mars 94/96 mission, are presented in Fig. 8.55.[8.78] Variant (a) enabled easy joining of the front-end focal-plane electronics with a heat sink over a distance of about 100 mm. This variant had a heat-transport capacity of several watts. Variant (b) was intended for higher-power heat transfer over a distance of 120 mm.

Gap Fillers

The mounting of some electronic devices results in large gaps. A special class of interface fillers has been developed for such mountings (Fig. 8.56). Known as gap fillers, they are very soft and compressible. Alfatec GmbH provides gap fillers made of ceramically loaded elastomers in their KERATHERM Softtherm product line. A generic analysis[8.79] has shown that thermal resistance of such elastomers reaches minimal values at pressures of 2.1 to 3.4 MPa. At lower pressures, 0.07 to 0.35 MPa, the thermal resistance is three times as much. The Bergquest Company[8.80] gives the range of gap-filler thicknesses as 0.51 to 4.1 mm, conductivity as 0.8 W/m·K, and thermal resistance of a 2.5-mm-thick pad as 0.0032 K·m^2/W at a pressure of 0.069 MPa.

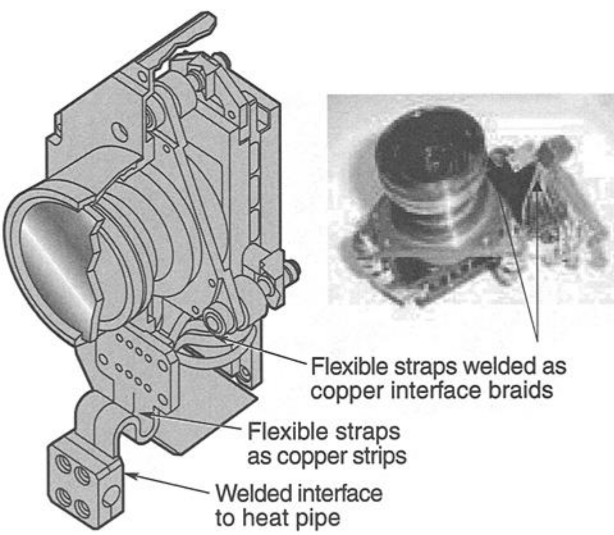

Fig. 8.54. Cascaded flexible thermal interfaces in WAOSS camera.[8.77] (Courtesy of DLR)

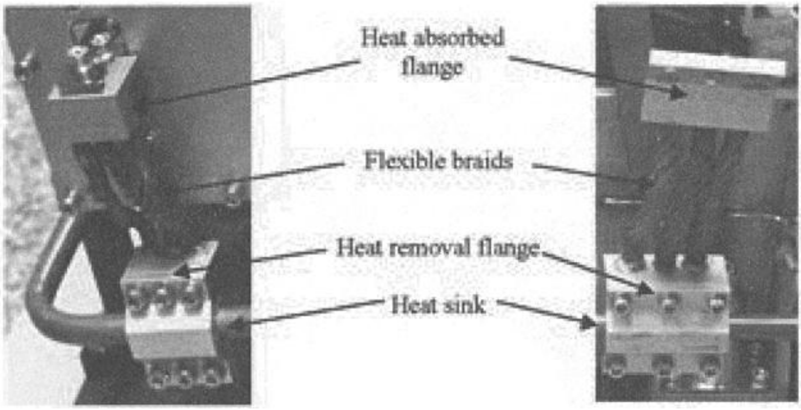

Fig. 8.55. Variant of extremely flexible strap, DLR/Dornier GmbH (now part of Astrium).[8.78] (Courtesy of DLR)

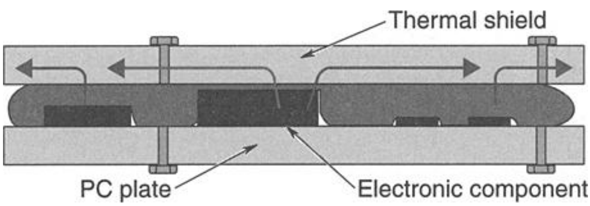

Fig. 8.56. Schematic of conformable pad application for cooling of microelectronics.

Carbon-Velvet Gaskets

Another type of flexible joint is provided by the carbon-velvet thermal-interface gaskets under development by Energy Science Laboratories, Inc. (ESLI)[8.81] These gaskets have not yet been used in space applications. They are made of a soft velvet consisting of numerous carbon fibers aligned perpendicularly to the substrate and anchored in a thin layer of adhesive (Fig. 8.57). The velvets are fabricated by precision-cutting continuous tows of carbon fiber and electrostatically "flocking" the fibers into uncured adhesive. Fiber diameter, length, and packing fraction typically vary from 5 to 12 μm, 0.25 to 3 mm, and 0.1 to 24%, respectively. Two velvets can be meshed together (like the surfaces in Velcro) to create a compliant joint between planar or curved surfaces. Various types of tailoring can improve this gasket's range of applicability.

Engineers must trade off the thermal and mechanical performance of the ESLI gasket. Highest thermal conductivity occurs with short, stiff velvets, while greatest compliance occurs with long, low-modulus velvets of low thermal conductivity. Table 8.17 shows the properties of three velvets as given by ESLI, with the most conductive, least compliant specimen in the top row, and the least conductive, most compliant specimen in the bottom row.

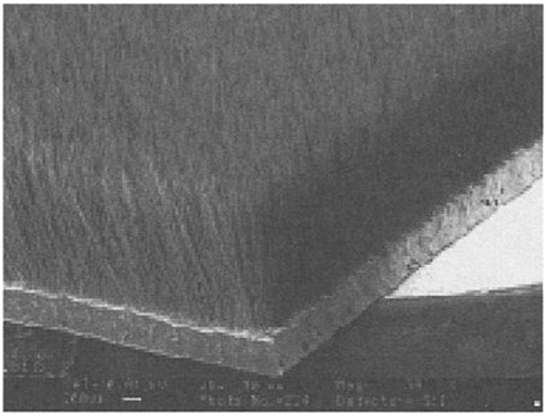

Fig. 8.57. SEM of ESLI[8.81] carbon-fiber velvet in vinyl substrate. Fibers are ~1 mm long. (© 2001 American Institute of Aeronautics and Astronautics, Inc. Reprinted with permission.)

Figure 8.58 shows the overall conductance of the intermediate specimen of Table 8.17 as measured in air by ESLI. The maximum value of 700 W/m^2·K is a factor of two less than that given in the table. In vacuum, the overall conductance is expected to be less than 300 W/m^2·K.

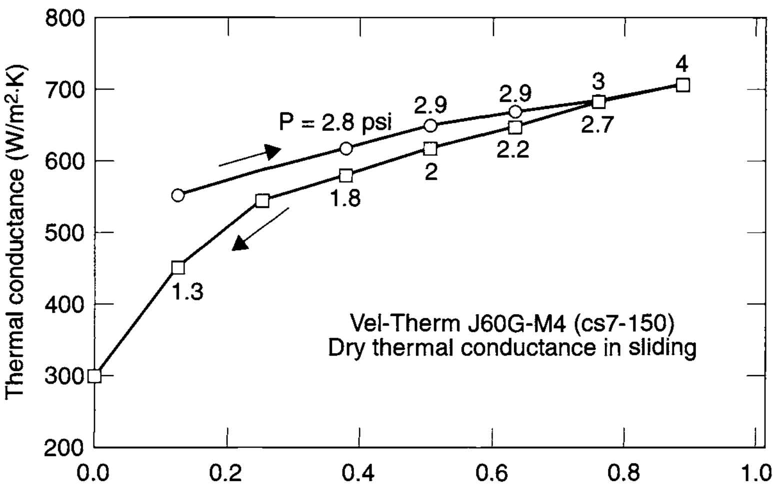

Fig. 8.58. Heat-transfer coefficient of intermediate test specimen of Table 8.16, as a function of compression and decompression.[8.81] (© 2001 American Institute of Aeronautics and Astronautics, Inc. Reprinted with permission.)

Table 8.17. Properties of Selected Carbon-Fiber Velvets[8.81]

Fiber	Fiber Length (mm)	Fiber Diam (μm)	Packing Fraction (%)	Fiber Conductivity (W/m·K)	Fiber Modulus (GPa)	Velvet Critical Buckling Stress (Pa)	Velvet Thermal Conductivity (W/m·K)	Velvet Thermal Conductance ($W/m^2 \cdot K$)
A20	0.5	10	10	1000	896	5.52×10^6	100	15,500
J60	1.5	7	3	100 to 200	434	34,500	3 to 6	1550
F100	2.5	6	2	20	234	4140	0.4	155

Figure 8.59 shows the overall thermal conductance for three pitch fiber velvets as measured in air by ESLI. The fibers were applied directly into the thermally loaded adhesive spread onto the lower aluminum bar. Much of the heat is conducted from the fiber to aluminum through air, which has a low thermal conductivity. Conductance improves with pressure and by biasing the fibers at an angle or by lapping the fiber tips so they are all the same height. Overall conductance values approaching 12,000 $W/m^2 \cdot K$ can be achieved in air by encapsulating the fibers in silicone gel.

While high thermal conductance can be achieved in some configurations by special measures, the most compelling applications of the carbon-velvet thermal-interface gaskets are expected to involve low-to-moderate conductance with the ability to accommodate sliding interfaces, applications with large or uneven gaps,

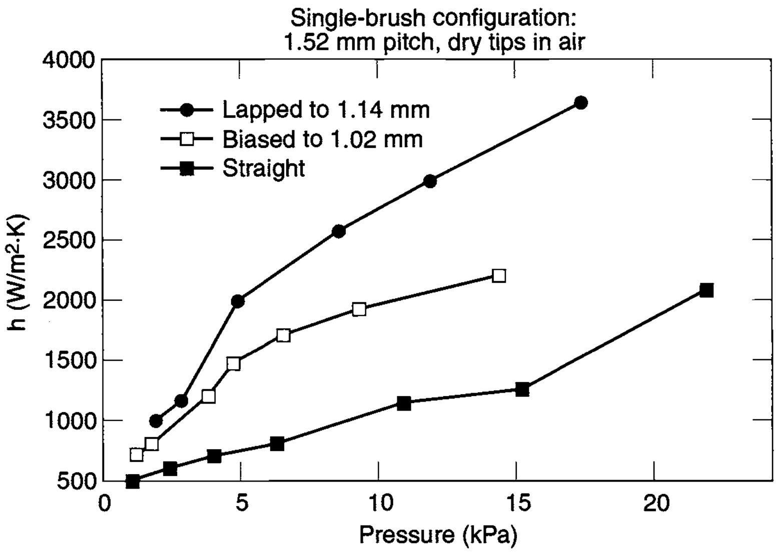

Fig. 8.59. Heat-transfer coefficient plotted against pressure for three pitch carbon-fiber velvets.[8.81] (© 2001 American Institute of Aeronautics and Astronautics, Inc., Reprinted with permission.)

and vibration isolation. An extremely important note is that this material can shed electrically conductive carbon fibers and should therefore be used only in applications where the fibers can be contained. Stray fibers in electrical connectors, electronics boxes, or moving mechanical assemblies can cause electrical shorts or mechanical jamming.

Thermal Isolation

Thermal isolators limit conductive heat transfer through a mechanical connection and provide temperature gradients between elements of a component. Typical applications include solar-panel and propellant-line supports, isolation under the mounting feet of instruments, coolant transport line and radiator isolation, battery mounting, and hydrazine-thruster catalyst-bed supports. Isolators can also be used to thermally decouple the spacecraft body from heat-storage units and optical devices, such as baffles and lenses.

These isolators can be made of a wide variety of low-conductivity materials, including fiberglass, stainless steel, titanium, and plastics. The choice of material is dictated by the conductivity, temperature range, thermal expansion, and mechanical properties required for the particular application. Properties of candidate isolator materials are presented in Table 8.18.

Table 8.18.[a] Typical Properties of Materials for Isolating Supports[8.82–8.85]

Material	Density (kg/m^3)	Young's Modulus (GPa)	Strength (MPa)	Coeff. of Thermal Expansion (μm/m/K)	Thermal Conductivity (W/m·K)	Thermal Resistance of Column[b] (K/W)
Titanium alloy Ti-6Al-4V	4400	110	825[c]	9.4	6–8	125–170
Stainless steel 304L	7800	193	170[c]	17.2	12–16	60–80
Graphite epoxy (Generic)	1580	190[d] 8[e]	525[d,f] 60[e,f]	–0.5[d] 29[e]	53[d] 2[e]	18.9[d] 500[e]
Polyether-etherketone (PEEK)	1320	3.6	92[c]	47	0.25	4000
Fiberglass-epoxy (CCO-BL)	2000	—	900[f]	—	< 1–2	> 500–1000
S-glass epoxy	1860	54	1450[f]	10.8[d] 36[e]	0.42	2380

[a]© 2001 American Institute of Aeronautics and Astronautics. Reprinted with permission.
[b]Calculated value for sample column with height 10 cm and cross section 1 cm^2
[c]Yield strength
[d]Longitudinal
[e]Transverse
[f]Ultimate strength

In the design of a thermal isolator that supports a significant mass, the efforts of thermal engineers should be coordinated with those of mechanical and structural designers. The idealized thermal requirements of minimum cross-sectional area and maximum length are generally the opposite of what is needed for structural stability. A typical simple isolator, shown in Fig. 8.60, includes isolation both between the components being bolted together and under the bolt head and nut to avoid a thermal "short" through the bolt. Contact resistances at the interfaces are generally ignored because they are small compared to the resistance through the isolator material itself. The resistance down the bolt can be increased by using titanium or, for very small devices, plastic bolts. In addition, the isolators should have a "lip" to prevent the bolt from shifting under launch vibration and contacting the isolated component. This type of isolator requires careful control of tolerances on hole diameters and locations so that all the pieces come together without interference for all of the "feet" on the device.

Additional thermal-isolator designs, verified in spaceflight applications, are presented in Fig. 8.61. The straightforward approach to realizing high thermal resistance via fiberglass rods is illustrated in Fig. 8.61(a).[8.50,8.85] By proper choice of rod height and diameter, a 2-kg mass was supported by four rod assemblies having an overall resistance greater than 400 K/W in this particular design. For heavier devices, with masses between 5 and 20 kg, rods long enough to meet thermal-isolation requirements will often not have sufficient structural strength to withstand launch vibration loads. In such cases, solid rods may be replaced with larger-diameter hollow tubes that have the same conductive cross-sectional area but are much stronger. Figure 8.61(b) shows an example of an instrument supported on six fiberglass tubes that achieved a thermal isolation of 218 K/W. Another alternative means of achieving thermal isolation is to use a conical tube to reduce the effective cross section and required standoff height. In one application,[8.86] illustrated in Fig. 8.61(c), four fiberglass/epoxy conical standoffs (total mass 0.1 kg) supported a mass of 8.4 kg; thermal resistance greater than 300 K/W was achieved.

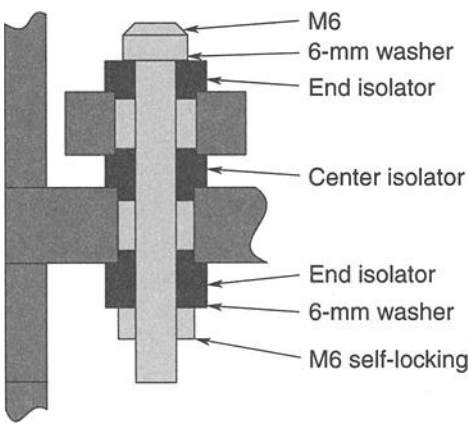

Fig. 8.60. Thermal isolation at bolted-joint interface.

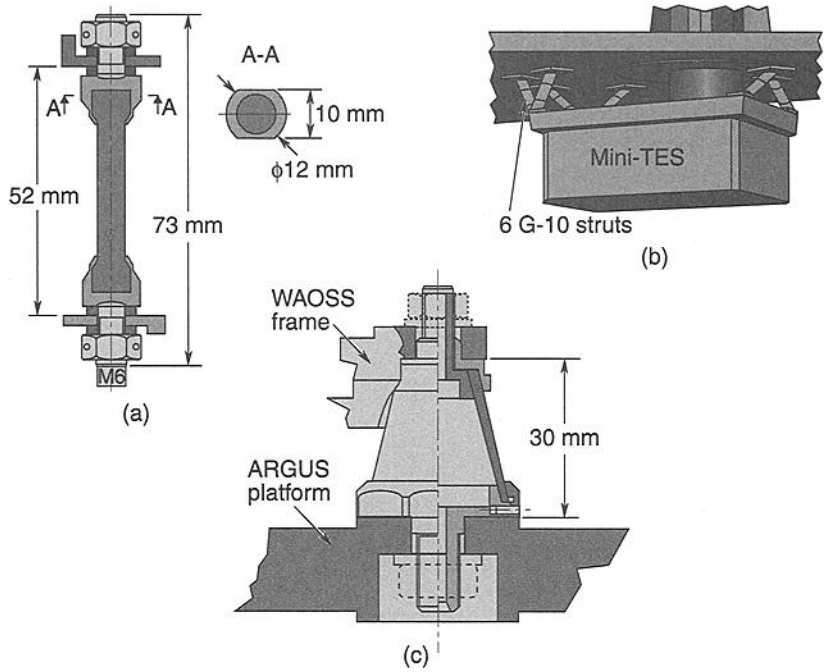

Fig. 8.61. Designs of thermal isolating standoffs. (a) Fiberglass rod. Courtesy of NTUU (KPI); (b) Courtesy NASA/JPL; (c) Courtesy of DLR.

The design can resist static loads of 3.5 kN in tension and 10 kN in compression. Devices heavier than 20 kg often do not require supports with very high thermal resistance because heat leaks through MLI and cables may dominate the thermal balance. In this regime, diverse support designs, having typical values of thermal resistance of 50 to 400 K/W, can be applied. One such design, presented in Fig. 8.62, increases the heat-transfer length between closely spaced plates through the use of

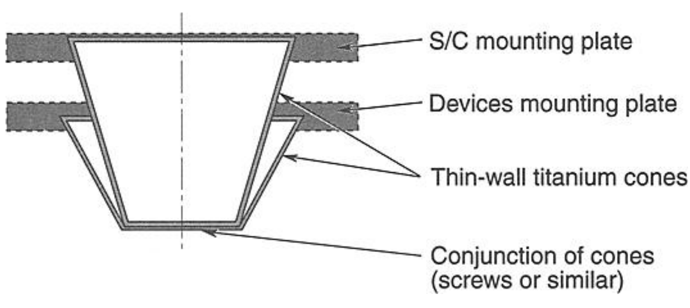

Fig. 8.62. Low-conductance support design using embedded titanium cones.

embedded cones. This design was used by DLR/Dornier GmbH for the high-resolution stereo camera flown on the Russian Mars 94/96 mission.[8.87]

Low-conductance mechanical attachment of large-area units such as solar arrays can be accomplished without the use of local standoffs like those discussed above. A schematic of a solar array attached to the Champ spacecraft with an open-cell Kapton foam[8.88] is presented in Fig. 8.63. In this design, the Kapton foam is glued to the honeycomb-panel satellite structure and covered with a graphite-epoxy facesheet to which the solar cells are attached. The thermal resistance of this isolation was not reported, although the response of the inner honeycomb panel to a solar-cell temperature range of −120 to +120°C was only 20°C.

Composite and Polymeric Interfaces

Modern spacecraft are making greater use of composite and nonmetallic materials for weight saving and CTE reduction, and in some cases for thermal conductivity and strength enhancement. Not much information has been published on joints made of these materials. What is available concerns uniformly applied pressure, not joints that use bolts or screws.

Rhoads and Moses[8.89] studied carbon fiber/epoxy resin composites in air. Samples had unidirectional continuous fibers oriented at 0 and 90 deg to the heat flow, with 0/0, 90/90, and 0/90 pairs investigated. Pressure was varied from 200 to 500 kPa. Best conductance was obtained with the 0/0 deg pair, although heat-transfer coefficients changed greatly (from 1000 to 3200 $W/m^2{\cdot}K$) as the samples were rotated 15 deg with respect to each other between tests. Results were poor with the 90/90 and 0/90 pairs with heat-transfer coefficient varying from 200 to 800 $W/m^2{\cdot}K$. The effect of pressure was very small for the 90/90 and 0/90 pairs, the 0/0 pair showing a slight increase with pressure. The authors attribute the better performance of the 0/0 pair, where the fibers are perpendicular to the contact surface, to the proximity of fiber ends at the contact surface. They attribute the variability to the change in relative fiber position at the contact surface resulting from the differential rotation of the samples between tests. They believe the poor performance of the 90/90 and 0/90 pairs was a result of the insulating effect of the resin, and the low transverse thermal conductivity of the carbon fibers that are parallel to the contact surface for the 90-deg samples.

The other relevant studies are all by the group at Texas A&M University led by L. S. Fletcher.[8.90–8.93] These studies all had mixed interfaces—a metal in contact with a composite or a polymer. Mirmira *et al.*[8.90] studied contact conductance of discontinuous and misoriented graphite fiber-reinforced composites at temperatures of 20 and 60°C over pressures from 172 to 1720 kPa. Three different fiber types

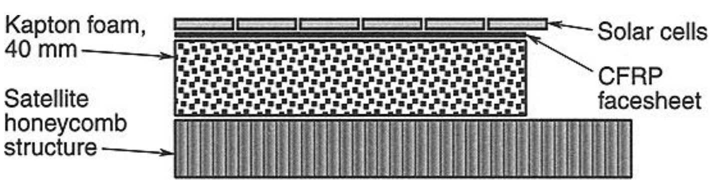

Fig. 8.63. Mechanical/thermal interface for spacecraft solar arrays.[8.88]

(Amoco supplied DKEX and DKAX, and Mitsubishi supplied K22XX) and three fiber-volume fractions (55, 65, and 75%) in a cyanate-ester matrix were studied. Composites so formed were in contact with an aluminum 6061-T6 surface. Heat-transfer coefficients varied from 100 to 1150 $W/m^2 \cdot K$, with temperature having little influence. Results were correlated by the empirical equation

$$(htV_f/k_h)^{1/3} = 3.03(P/H_{C,h})^{0.0703}, \tag{8.33}$$

which, when solved directly for heat-transfer coefficient, yields

$$h = 28.0(k_h/tV_f)(P/H_{C,h})^{0.211}. \tag{8.34}$$

The harmonic-mean thermal conductivity and hardness are based on fiber and matrix. The properties of the aluminum surface do not enter into the correlation.

Mirmira and Fletcher[8.91] tested a variety of fiber-resin formulations and configurations as described in Tables 8.19 and 8.20. The mating surface in this case was that of an electrolytic iron heat-flux meter. Heat-transfer coefficients as a function of pressure are shown in Fig. 8.64. The three neat (pure) resins have the lowest

Table 8.19. Characteristics of Cured Carbon and Glass Fiber-Reinforced Composites[a]

Sample Number, Resin	Fiber	Weave	Orientation	Fiber Volume (%)
Resin 1 (amine-cured epoxy)	none	none	Neat resin	0
Resin 2 (amine-cured epoxy)	none	none	Neat resin	0
1, resin 1	IM7	Plain weave	[0]	51.3
2, resin 1	E-glass	Style 7781	[(0/90)]	50.5
3, resin 1	AS4	Plain weave	[0]	58.0
4, resin 1	Carbon	Uniweave	[0]	50.7
5, resin 1	AS4	5 harness satin	[0]	51.1
6, resin 1	E-glass	Style 7781	[(0/90)]	49.7
7, resin 1	AS4	5 harness satin	[(0/90)]	48.5
8, resin 2	E-glass	Style 7781	[(0/90)]	50.5
9, resin 2	Carbon	Uniweave	[0]	47.3
10, resin 2	IM7	Uniweave	[0]	52.1
11, resin 2	AS4	Uniweave	[0]	57.1
12, resin 2	IM7	Uniweave	[0]	62.1
13, resin 2	AS4	Plain weave	[(0/90)]	52.3
14, resin 2	E-glass	Uniweave	[(0/90)]	47.0

Table 8.20. Characteristics of Cured Pitch Graphite Fiber-Reinforced Composites

Sample Number, Resin	Fiber	Manufacturer of Fiber	Thermal Conductivity, Parallel to Axis (W/m·K)	Fiber Volume (%)
Resin 3 (cyanate ester)	none	—	—	0
15, resin 3	DKAX	Amoco	900	55
15, resin 3	DKAX	—	—	65
15, resin 3	DKEX	—	617	55
15, resin 3	DKEX	—	—	65
15, resin 3	K22XX	Mitsubishi	600	55
15, resin 3	K22XX	—	—	65

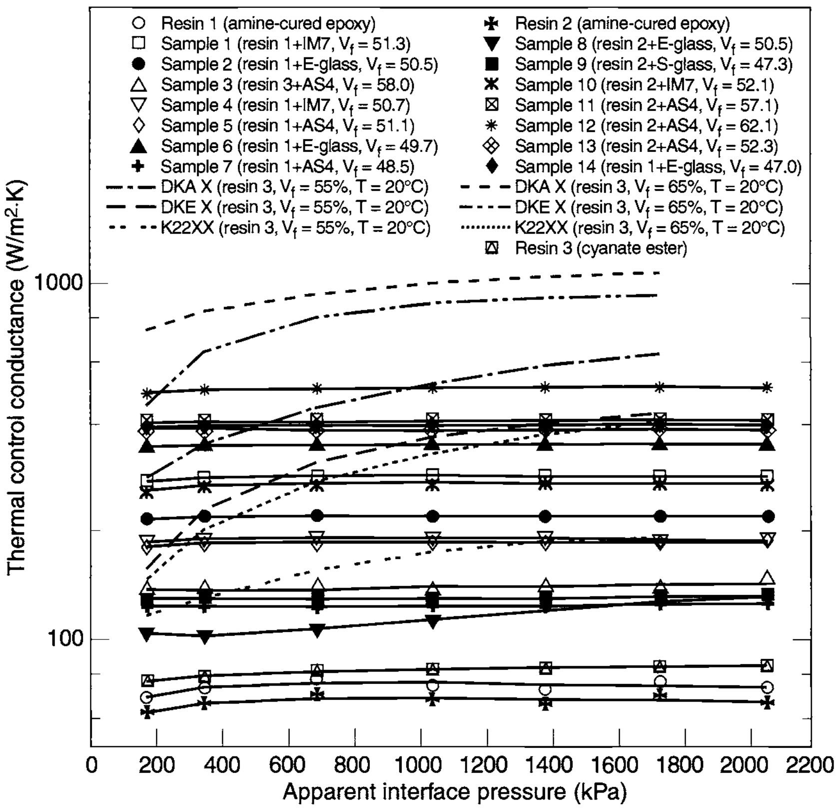

Fig. 8.64. Heat-transfer coefficient of composites as a function of apparent interface pressure.[8.91] (© 1999 American Institute of Aeronautics and Astronautics. Reprinted with permission.)

coefficients (30 to 75 W/m^2·K), each independent of pressure. The heat-transfer coefficients for the composites of the amine-cured epoxy resins (resins 1 and 2) are invariant with pressure. The authors attribute this to absence of sample thinning with pressure. The pitch graphite resin composites have moderately high coefficients (110 to 710 W/m^2·K) at 180 kPa pressure, with coefficients increasing to 200–1050 W/m^2·K as pressure increases to 1700 kPa. Mirmira and Fletcher attribute this to the observed sample thinning and reduction in interface resistance between fiber and matrix with pressure.

Marotta and Fletcher[8.92] studied the contact conductance of thermosetting and thermoplastic polymers: ABS, Delrin, Teflon, Nylon 6,6, LE phenolic, polycarbonate, UHMW polyethylene, polypropylene, and polyvinyl chloride. The mating surface was aluminum 6061-T6. Results are shown in Fig. 8.65. UHMW polyethylene showed the highest heat-transfer coefficients; both UHMW polyethylene and polycarbonate showed an increase in coefficient with temperature. Results were compared to the Cooper-Mikic-Yovanovich (CMY) plastic model[8.4] in Fig. 8.66. Here k_S is the harmonic-mean thermal conductivity of the polymer and Al 6061, H is the microcontact hardness of the softer of the mating materials, and *s/m*

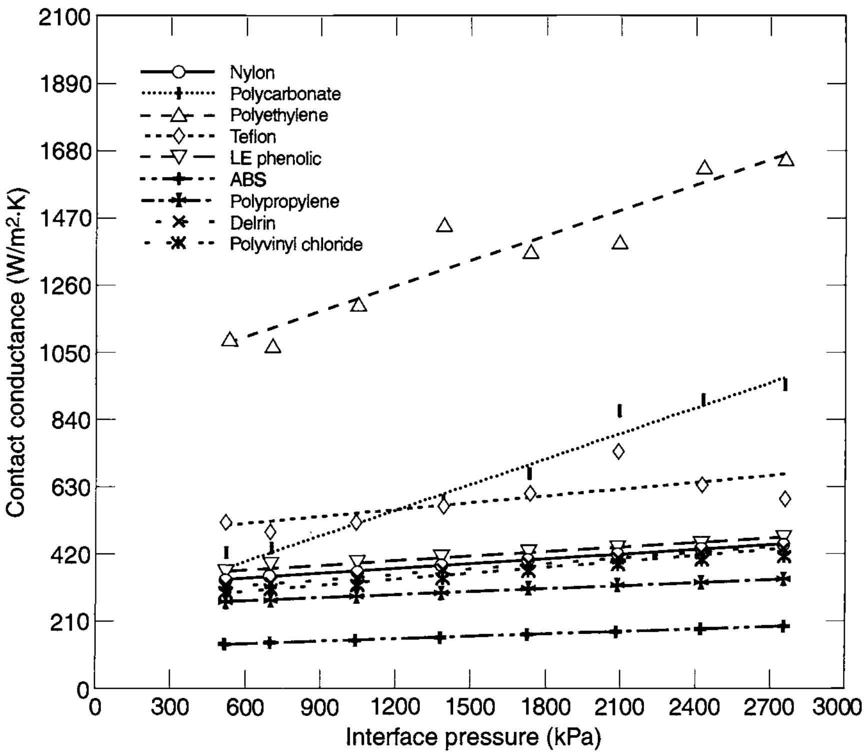

Fig. 8.65. Heat-transfer coefficient of polymers as a function of apparent interface pressure.[8.92]

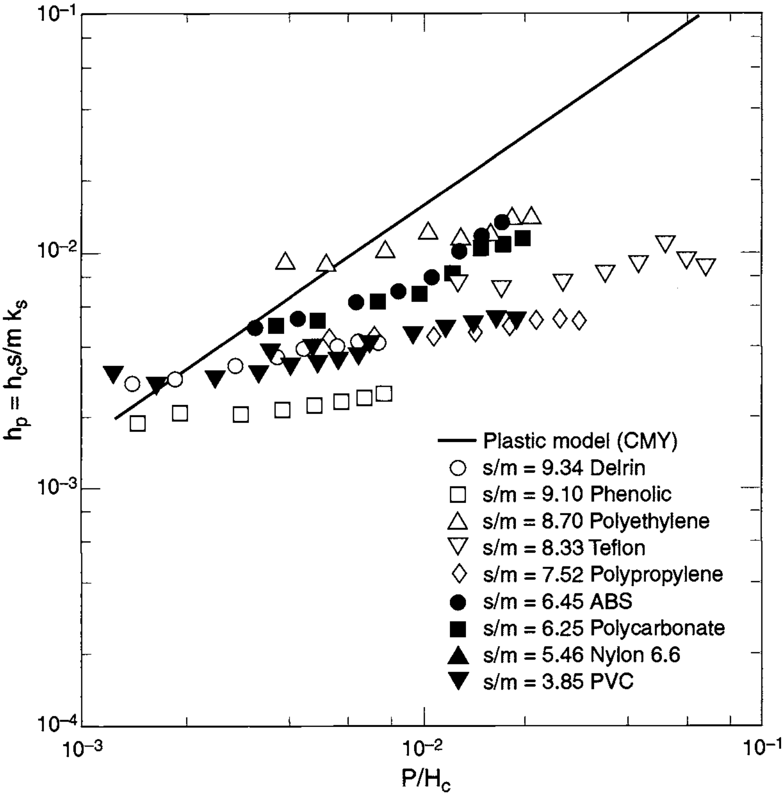

Fig. 8.66. Comparison of dimensionless contact heat-transfer coefficient for various polymers with CMY[8.4] plastic model.[8.92] (©1996 American Institute of Aeronautics and Astronautics, Inc. Reprinted by permission.)

in the legend is rms roughness divided by asperity slope with units μm. For the various polymers the plot of dimensionless heat-transfer coefficient against dimensionless pressure shows slopes much lower than that of the CMY model. Marotta and Fletcher attribute this difference to the softness of the polymers.

Lambert and Fletcher[8.93] determined heat-transfer coefficients for bare and electroplated silver-coated continuous-K1100-graphite reinforced aluminum 6063 in contact with aluminum A356-T61 at 20, 60, and 100°C. The silver coating is needed in marine or corrosive environments to prevent galvanic corrosion. For a pressure at 180 to 3000 kPa, heat-transfer coefficients for the former pair varied from 750 to 23,000 W/m·K, and for the latter pair they varied from 1000 to 4400 W/m·K.

Bearing Conduction

Conductance across bearings is one of the most uncertain parameters in spacecraft thermal analysis. The large dependence of the conductivity upon factors such as bearing design, speed, lubricant type and quantity, load, and temperature gradients from inner to outer race make identifying "generic" conductivities for bearings impossible.

The bearing cross section shown in Fig. 8.67 illustrates the conduction mechanisms for a ball bearing in vacuum. A conduction path runs through the ball/race contact regions as well as through the lubricant. The contact conductance is affected by lubrication and the load, which is itself driven by preload, gravity effects, speeds, and temperature differences between the races. The conduction through the lubricant is complex and highly dependent upon the type and amount of lubricant and the rotational speed. Figures 8.68 through 8.70 contain measured

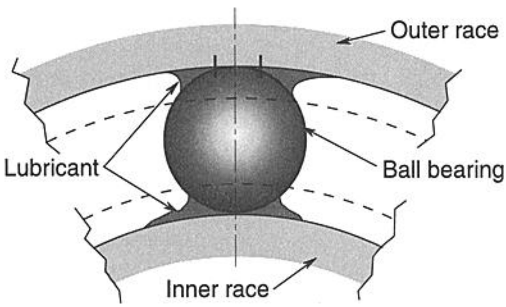

Fig. 8.67. Bearing cross section.

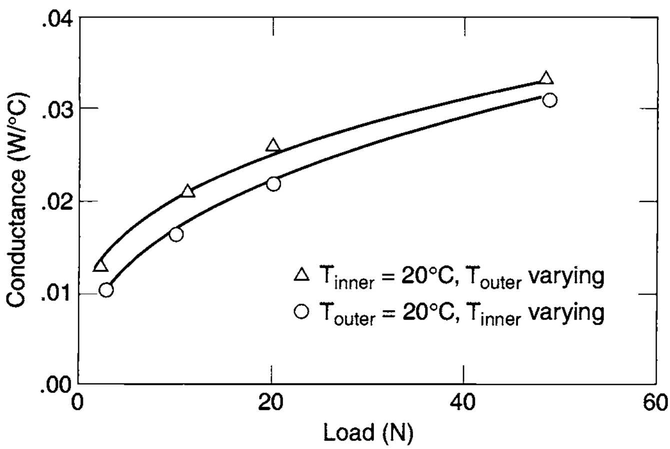

Fig. 8.68. Mean conductance as a function of load for lead-lubricated, nonrotating 42-mm O/D bearing.[8.94]

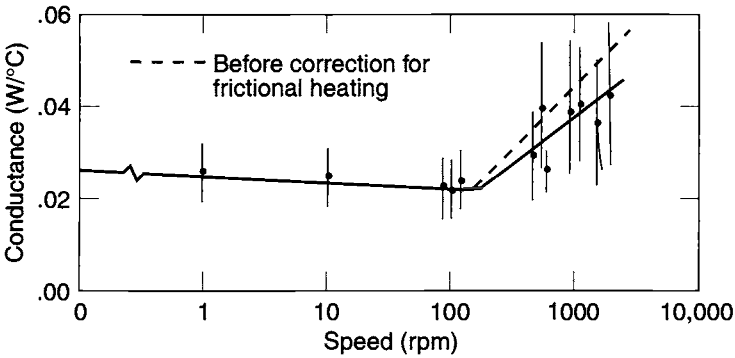

Fig. 8.69. Conductance versus speed for 42-mm O/D lead-lubricated bearing.[8.94] Load = 20 N; T_i = 40°C; T_o = 20°C.

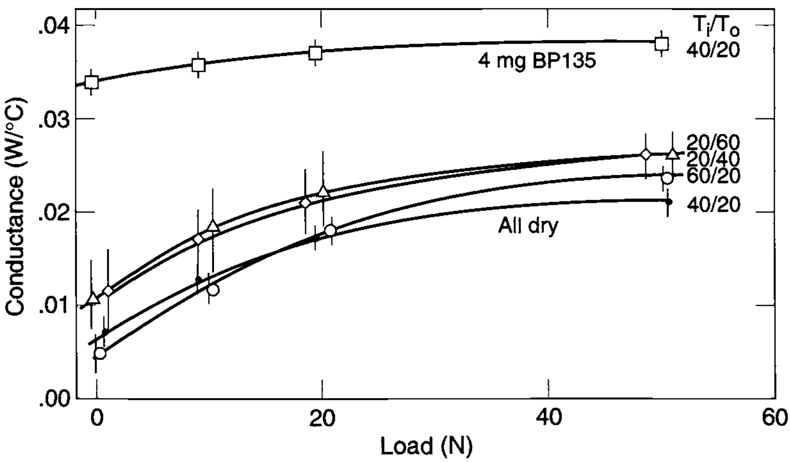

Fig. 8.70. Conductance as a function of load for nonrotating 16-mm O/D bearing.[8.94]

data for a particular set of bearings,[8.94] which illustrate the considerable effect of some of these factors on bearing conductance. The reader may wish to consult Yovanovich[8.94] for additional discussions on this subject. Other reports and papers[8.95,8.96] have discussed the theoretical and experimental evaluation of the factors affecting bearing conduction.

Despite the considerable research done in this area, a generalized set of conduction values for thermal analysis involving bearings cannot be provided. The analyst has the options of performing tests[8.94–8.96] to measure the conductivities of the bearings in question, or bounding the problem by looking at a wide range of conductance values. Any test must accurately simulate the lubrication, load, speed, vacuum-temperature ranges, and gradients expected in flight, while ensuring that any gravity effects are accounted for. If a bounding analysis is conducted, a suitably wide range of conductances must be considered, e.g., from zero to a fairly high contact conductance across the entire area of the races. If the analysis shows a considerable sensitivity to bearing conductance, test measurements on the bearings early in the program are recommended. Do not rely on system-level thermal tests that may not provide the right conditions and that will usually occur too late in the program for practical design changes.

Classical Contact-Conductance References from the Former USSR

Considerable work was performed in the former USSR in the field of contact-conductance heat transfer. Two references are particularly useful.[8.97,8.98] Popov[8.97] presents a survey of experimental and theoretical work on contact heat exchange, with description of physical and mechanical interaction in the contacting zone of solid bodies. A special chapter of the work is devoted to analysis of contact heat exchange for flat surfaces, for surfaces with waviness and macroroughness, and for surfaces in contact at high static pressure loading (109 literature sources). The author depicts methods of experimental study of thermal contact and includes a section with original data. The essential part of the book is devoted to analysis of experimental data for contact of flat surfaces under initial and sequent loading; nonsteady heat transfer; and the influences of waviness, roughness, time of loading, and oxide layer. Also contained within are recommendations for regulating contact conductance (in particular, with the use of glues) and practical examples of technical solutions.

Shlykov *et al.*[8.98] analyze steady and unsteady methods of thermal-contact experimentation. They present a vast survey of experimental and theoretical works on contact heat exchange (175 sources) including heat contact transfer in nuclear technology, energy converters, cryogenic technology, and electronics. One chapter of this work presents a theoretical model of contact conductance with different boundary conditions. The correlations obtained have been adapted to conditions of real contact: contact of rough bodies, conductivity via gas gap, and conductivity in the contact zone. The authors have proposed a generalized equation for contact heat exchange that complies well with experiments.

Nomenclature

a	contact radius; outer radius in Roca and Mikic mechanical model; heat-flux radius at top of doubler, Gluck and Young (m)
A	area (m^2)
A_b	area of contact region near bolt or screw (m^2)
A_N	area divided by number of bolts or screws (m^2)
b	component radius; doubler radius, Gluck and Young (m)
C	conductance (W/K)
C_b	bolt region conductance (W/K)
CCD	charge-coupled device
CTE	coefficient of thermal expansion (K^{-1})

d	height of waviness represented as spherical crown; gas gap between parallel plates; distance between bolt centers (m)
d^*	normalized distance between bolt centers, $d^* = d/(2r_O)$
D_s	bolt-shaft diameter (m)
DLR	Deutsches Zentrum für Luft- und Raumfahrt e.V. /German Aerospace Center
E	elastic modulus; effective elastic modulus, Roca and Mikic (N/m^2)
E'	effective elastic modulus (N/m^2), $E' = [(1-\upsilon_1^2)/E_1 + (1-\upsilon_2^2)/E_2]^{-1}$
f	factor from Song representing Integral model of Yovanovich, $f = 0.304/[(R_p/\sigma)(1+M/R_p)] - 2.29/[(R_p/\sigma)(1+M/R_p)]^2$
F	heat flux (W/m^2)
F_O	average heat flux through doubler, Gluck and Young (W/m^2)
F_S	heat flux over radius, a, at top of doubler, Gluck and Young (W/m^2)
F^*	dimensionless heat flux, Ayres *et al.*, $F^* = (F\beta_E R_E/k_E)(E_E/H_E)(\beta_i/\beta_o)^3[0.5(1 + P_{amb}/P_{atm})]^2$
G	dimensionless gap resistance, $G = k_g/h_g R_p$
h	heat-transfer coefficient ($W/m^2{\cdot}K$)
h_b	bolt region heat-transfer coefficient, Bevans *et al.* ($W/m^2{\cdot}K$)
h_C	contact region heat-transfer coefficient, Roca and Mikic ($W/m^2{\cdot}K$)
h_p	plate region heat-transfer coefficient, Bevans *et al.* ($W/m^2{\cdot}K$)
h_r	linear radiation heat-transfer coefficient, Bobco and Starkovs ($W/m^2{\cdot}K$)
h^*	dimensionless heat-transfer coefficient, Ayres *et al.*, $h^* = h\sigma_E/k_E m_E$
H	bulk hardness (N/m^2)
H_C	microcontact hardness (N/m^2)
$H_{C,h}$	microcontact hardness, harmonic mean of fiber and matrix, Mirmira *et al.* (N/m^2)
H_L	macrocontact hardness (N/m^2)
I	geometric term, Bevans *et al.*, $I = \eta_O^2 - \eta_O^4/4 - ln(\eta_O) - 3/4$
k	thermal conductivity; harmonic-mean thermal conductivity, Roca and Mikic ($W/m{\cdot}K$)
k_h	harmonic-mean thermal conductivity ($W/m{\cdot}K$), $k_h = 2k_1k_2/(1/k_1 + 1/k_2)$
k_S	harmonic-mean thermal conductivity, Cooper-Mikic-Yovanovich model ($W/m{\cdot}K$)
Kn	Knudsen number, $Kn = \Lambda/d$
KPI	Kyiv Polytechnic Institute, Ukraine
l	length in x direction, Bobco and Starkovs (m)
L	length; doubler height, Gluck and Young (m)
m	combined mean absolute profile slope (m/m), $m = (m_1^2 + m_2^2)^{1/2}$
M	gas parameter (m), $M = [(2 - TAC_1)/TAC_1 + (2 - TAC_2)/TAC_2] \times [2\gamma/(\gamma + 1)][1/Pr]$
M^*	gas rarefaction parameter, $M^* = M/Rp$
N	bolted plate contact parameter
NTUU	National Technical University of Ukraine
p	pressure (N/m^2)
P	uniform or apparent pressure; applied pressure, Roca and Mikic (N/m^2)

P_{amb}	local pressure, e.g., vacuum, Ayres *et al.* (N/m^2)
P_{atm}	atmospheric pressure at sea level, Ayres *et al.* (N/m^2)
PSA	pressure-sensitive adhesive
Pr	Prandtl number
q, Q	heat flow rate (W)
q	heat flux, Bobco and Starkovs (W/m^2)
q_o	thermal doubler heat flux, Bobco and Starkovs (W/m^2)
r	radial coordinate (m)
r_C	radius of contact region (m)
r_O	radius of applied load (m)
R	outer radius, Roca and Mikic, Bevans *et al.* (m)
R	thermal resistance, Roca and Mikic (Km^2/W)
R	thermal resistance, Compliant Interfaces-flexible braid (K/W)
R_o	radius of contact region near bolt, Bevans *et al.* (m)
R_P	maximum peak height of the rougher surface of the plate pair in contact, Song (m)
RTV	room-temperature vulcanized
s	rms roughness, Cooper-Mikic-Yovanovich model (m)
s/m	rms roughness divided by asperity slope, Cooper-Mikic-Yovanovich model (μm)
t	thickness; thickness of plate (m)
t_t	thickness of thinnest of two plates in contact (m)
T	temperature (K)
T_i	boundary-condition sink temperature, Roca and Mikic (K)
TAC	thermal-accommodation coefficient
TIR	total included reading, i.e., flatness deviation (m), $TIR = TIR_1 + TIR_2$
T_o	baseplate temperature, Gluck and Young (K)
T_∞	equivalent sink temperature, Bobco and Starkovs (K)
V_f	volume fraction of fiber
w, W	width (m)
x	coordinate (m)
y	coordinate (m)
Y	effective gap thickness (m)
z, Z	vertical coordinate (m)
a	coefficient of thermal expansion
b	Biot-like group, $\beta = k/hb$, Gluck and Young
g	deformation mode parameter, $\gamma = H_c/(Em)$; ratio of specific heats
d	ratio of heat-source radius to doubler radius, $\delta = a/b$, Gluck and Young
δ_O	thermal doubler thickness, Bobco and Starkovs, (m)
h	dimensionless radius, Bevans *et al.*, $\eta = r/R$
η	coefficient relating the real heat-transfer length of threads with L, Compliant Interfaces section
η_O	dimensionless radius at end of contact region, Bevans *et al.*, $\eta_O = R_O/R$
L	molecular mean free path (m)

u	Poisson ratio
σ	combined root mean square (rms) roughness (m), $\sigma = (\sigma_1{}^2 + \sigma_2{}^2)^{1/2}$
σ_Z	normal stress, Roca and Mikic (N/m^2)
t	torque (N·m)
f	temperature difference, $T - T_o$, Gluck and Young (K)
y	dimensionless temperature difference, $k\phi/(2aF_s)$, Gluck and Young

Superscripts

'	effective

Subscripts

al	aluminum
b	bolt
C	contact
e	elastic
E	effective, Ayres *et al.*
g	gas
h	harmonic mean
i	inside
L	large-scale, macroscopic
m	arithmetic mean
o	outside
p	plastic, plate
ss	stainless steel
S	small-scale, microscopic
1	surface or plate 1
2	surface or plate 2

References

8.1. A. N. Tabenkin, "Use Surface Finish to Get Optimum Production," *Modern Machine Shop* **62**, 52–62 (February 1990).

8.2. M. A. Lambert and L. S. Fletcher, "A Correlation for the Thermal Contact Conductance of Metallic Coated Metals," AIAA 93-2778, presented at the *AIAA 28th Thermophysics Conference* (July 1993).

8.3. M. B. H. Mantelli and M. M. Yovanovich, "Thermal Contact Resistance," Chapter 16 in *Spacecraft Thermal Control Handbook*, 2nd ed., edited by D. G. Gilmore (The Aerospace Press, El Segundo, California, 2002).

8.4. M. G. Cooper, B. B. Mikic, and M. M. Yovanovich, "Thermal Contact Conductance," *Int. J. Heat Mass Transfer* **12**, 279–300 (1969).

8.5. B. B. Mikic, "Analytic Studies of Contact of Nominally Flat Surfaces; Effect of Previous Loading," ASME Paper 71-Lub-M, 1971.

8.6. B. B. Mikic, "Thermal Contact Conductance: Theoretical Considerations," *Int. J. Heat Mass Transfer* **17**, 205–214 (1974).

8.7. M. A. Lambert and L. S. Fletcher, "Review of Models for Thermal Contact Conductance of Metals," *AIAA Journal of Thermophysics and Heat Transfer* **11** (2), 129–140 (April–June 1997).

8.8. A. A. Hegazy, "Thermal Joint Conductance of Conforming Rough Surfaces," Ph. D. thesis, University of Waterloo, Waterloo, ON, Canada, 1985.

8.9. S. Song and M. M. Yovanovich, "Relative Contact Pressure: Dependence on Surface Roughness and Vickers Microhardness," *AIAA Journal of Thermophysics and Heat Transfer* **2** (1), 43–47 (January 1988).

8.10. M. R. Sridhar and M. M. Yovanovich, "Elastoplastic Contact Conductance Model for Isotropic Conforming Rough Surfaces and Comparison with Experiments," Thermal Phenomena at Molecular and Microscales and in Cryogenic Infrared Detectors, *ASME HTD* **277**, 43–56 (1994).

8.11. A. M. Clausing and B. T. Chao, "Thermal Contact Resistance in a Vacuum Environment," *Journal of Heat Transfer* **87** (3), 243–251 (May 1965).

8.12. H. R. Hertz, *Miscellaneous Papers*, English translation (MacMillan and Co., London, 1896).

8.13. M. A. Lambert and L. S. Fletcher, "Thermal Contact Conductance of Spherical, Rough Metals," HTD-Vol. 327, *National Heat Transfer Conference*, Vol. 5, ASME (1996), pp. 169–175.

8.14. M. A. Lambert and L. S. Fletcher, "Thermal Contact Conductance of Spherical, Rough Metals," ASME Transactions, *Journal of Heat Transfer* **119** (4), 684–690 (November 1997).

8.15. G. S. Springer, "Heat Transfer in Rarefied Gases," in *Advances in Heat Transfer*, Vol. 7, edited by T. F. Irvine and J. P. Hartnett (Academic Press, New York, 1971) pp. 163–218.

8.16. S. Song, M. M. Yovanovich, and F. O. Goodman, "Thermal Gap Conductance of Conforming Surfaces in Contact, Part I: Theory," *10th Symposium on Thermophysical Properties* (Gaithersburg, MD, 20–23 June 1988).

8.17. S. Song and M. M. Yovanovich, "Thermal Gap Conductance of Conforming Surfaces in Contact, Part II: Experimental Results," *10th Symposium on Thermophysical Properties* (Gaithersburg, MD, 20–23 June 1988).

8.18. S. Song, M. M. Yovanovich, and K. Nho, "Thermal Gap Conductance: Effect of Gas Pressure and Mechanical Load," AIAA-89-0429, 1989.

8.19. P. J. Schneider, "Conduction" in *Handbook of Heat Transfer*, edited by W. M. Rohsenow and J. P. Hartnett (McGraw-Hill, New York, 1973).

8.20. E. Fried and F. A. Costello, "Interface Thermal Contact Resistance Problem in Space Vehicles," *ARS Journal* **32**, 237–24 (1962).

8.21. M. E. Barzelay *et al.*, "Effect of Pressure on Thermal Conductance of Contact Joints," NACA TN 3295, Washington, D. C., 1955.

8.22. E. Fried, "Study of Interface Thermal Contact Conductance," General Electric Co. 64SD652, May 1964 (also ARS Paper No. 1690-61, April 1961).

8.23. H. Fenech and W. H. Rohsenow, "Prediction of Thermal Conductance of Metallic Surfaces in Contact," *J. Heat Transfer, Trans. ASME* **85**, 15–24 (1963).

8.24. C. Swartz, "Thermal Conductance in Aluminum Bolted Joints," The Aerospace Corporation ATM 82(9975)-29, 19 January 1982.

8.25. E. Fried and M. J. Kelley, "Thermal Conductance of Metallic Contacts in a Vacuum" in *Thermophysics and Temperature Control*, edited by G. Heller (Academic Press, New York, 1966).

8.26. E. Fried and H. L. Atkins, "Thermal Joint Conductance in Vacuum," ASME Paper 63-AHGT-18, 1963.

8.27. S. Timoshenko and J. N. Goodier, *Theory of Elasticity*, 2nd ed. (McGraw-Hill, New York, 1951).

8.28. R. T. Roca and R. E. Mikic, "Thermal Contact Resistance in a Non-Ideal Joint," Massachusetts Institute of Technology, Report No. DSR 71821-77, Nov. 1971.

8.29. R. T. Roca and R. E. Mikic, "Thermal Conductance in a Bolted Joint," AIAA Paper No. 72-282, April 1972.

8.30. I. Fernlund, "A Method to Calculate the Pressure Between Bolted or Riveted Plates," Report No. 17, Chalmers University of Technology, Gothenberg, Sweden, 1961.

8.31. J. A. Greenwood, "The Elastic Stresses Produced in the Mid-Plane of a Slab by Pressures Applied Symmetrically at its Surface," *Proc. Camb. Phil. Soc.* **60**, 159–169 (1964).

8.32. E. H. Coker and L. N. G. Filon, *A Treatise on Photo-Elasticity*, 2nd ed. (Cambridge University Press, Cambridge, 1957).

8.33. W. Aron and G. Colombo, "Controlling Factors of Thermal Conductance across Bolted Joints in a Vacuum Environment," ASME Paper 63-WA-196, 1963.

8.34. H. H. Gould and B. B. Mikic, "Areas of Contact and Pressure Distribution in Bolted Joints," M.I.T. Heat Transfer Report DSR 71821-68, June 1970.

8.35. J. T. Bevans, T. Ishimoto, B. R. Loya, and E. E. Luedke, "Prediction of Space Vehicle Thermal Characteristics," Air Force Flight Dynamic Laboratory Technical Report AFFDL-TR-65-139, August 1965.

8.36. Anon., "Thermal Environments," in TRW, Inc. Project MILSTAR Engineering Design Standards, Section 2.2, March 1984.

8.37. G. D. Rhoads, informal data transmittal, 1990.

8.38. E. Veilleux and M. Mark, "Thermal Resistance of Bolted of Screwed Metal Joints in Vacuum," *J. Spacecraft* **6** (3) (March 1969).

8.39. C. A. Baumgartner to R. L. MacGregor, "Interface Resistance—Aluminum to Aluminum Test Report Project ROARS," TRW Inc. interoffice correspondence 7415.1-467, June 1969.

8.40. P. F. Taylor to W. A. Hagemeyer, Jr., "TWT Collector Thermal Interface Test," Hughes Inc. interdepartmental correspondence 72261/0042, December 1985.

8.41. J. W. Welch and L. E. Ruttner, "An Experimental and Computational Analysis of the Thermal Interface Filler Material Calgraph," Paper AIAA-89-1658 presented at the *AIAA 24th Thermophysics Conference* (June 1989).

8.42. T. F. Bratkovich, "Correlations for Contact Region Bolted Joint Conductance in Vacuum," The Aerospace Corporation, ATM No. 91(9975)-15, 10 April 1991.

8.43. M. B. H. Mantelli and M. M. Yovanovich, "Experimental Determination of the Overall Thermal Resistance of Satellite Bolted Joints," Paper AIAA 94-0123 presented at *32nd Aerospace Sciences Meeting and Exhibit* (January 1994).

8.44. M. B. H. Mantelli and C. J. Goncalves, "Thermal Resistance of Parallel Plate-Washer Bolted Joints: Model and Experimental Verification" Paper AIAA 99-3489 presented at *33rd Thermophysics Conference* (June–July 1999).

8.45. L. S. Fletcher, P. A. Smuda, and D. A. Gyorog, "Thermal Contact Resistance of Selected Low-Conductance Interstitial Materials," *AIAA Journal* 7 (7), 1302–1309 (1969).

8.46. P. Brennan and E. Kroliczek, NASA Report N81-70113, Heat Pipe Design Handbook, National Aeronautics and Space Administration, Goddard Space Flight Center, June 1979.

8.47. F. Lura, B. Biering, and V. Baturkin, "Heat Pipe Application for Thermal Stable Bench Arrangement in Small Satellite Design," Rep. No. 2000-01-2460, *Proceedings of the 30th Int. Conference on Environmental Systems (ICES)* and *7th European Symposium on Space Environmental Control Systems* (Toulouse, France, 10–13 July 2000).

8.48. V. Baturkin and D. Olefirenko, "Research on Axially Grooved Heat Pipe Heat Transfer Characteristics in Ground Tests," Rep. No. 2001-01-2237, *Proceedings of the 31th Int. Conference on Environmental Systems (ICES)* (Orlando, 9–12 July 2001).

8.49. B. Lehmann, B. Biering, V. Baturkin, *et al.*, "Cooling of Electronic Unit Elements with Application of Heat Pipes," *Proceedings of the Int. Symposium on Heat Pipe Research and Application*, Japan Association for Heat Pipes (Shanghai, China, 24–27 April 1991), pp.192–197.

8.50. M. G. Semena., V. M. Baturkin, N. K. Gretchina, *et al.*, "Working Out of the Cryogenic Cooling System on the Base of Heat Pipes for VEGA Television Camera," Paper N 1072 presented at Space Research Institute of USSR AS, 1986.

8.51. F. Lura, B. Biering, *et al.*, "TCS Design of the Microsatellite BIRD for Infrared Earth Observation," Rep. No. 981639, *Proceedings of the 28th Int. Conference on Environmental Systems* (Danvers, MA, 13–16 July 1998).

8.52. V. Baturkin and K. Shkoda, "Heat Transfer in Zones of Heat Supply and Removal of Heat Pipes," *Proceedings of the Int. Symposium on Heat Pipe Research and Application*, Japan Association for Heat Pipes (Shanghai, China, 24–27 April 1991), pp. 89–95.

8.53. V. Baturkin V., L. Bondar, and K. Shkoda, "Thermal Regimes Simulation of Ramified Heat Pipes Communications by Finite Element Method," Rep. No. 951553, *Proc. of 25th International Conference on Environmental Systems* (San Diego, CA, 10–13 July 1995).

8.54. D. Gluck, C. Gerhart, and S. Stanley, "Characterization of a High Capacity, Dual Compensation Chamber Loop Heat Pipe," presented at *Space Tech. & Applications International Forum (STAIF-99)* (Albuquerque, NM, Jan.–Feb., 1999).

8.55. G. H. Ayers, L. S. Fletcher, and C. V. Madhusudana, "Thermal Contact Conductance of Composite Cylinders," *Journal of Thermophysics and Heat Transfer* **11** (1), 72–81 (January–March 1997).

8.56. R. P. Bobco and R. P. Starkovs, "Rectangular Thermal Doublers of Uniform Thickness," *AIAA Journal* **23** (12), 1970–1977 (December 1985).

8.57. R. P. Starkovs, "Rectangular Thermal Doublers with Two Heated Footprints," AIAA-87-1612, June 1987.

8.58. R. P. Bobco, "Thermal Doublers: Closed Form Solution for Three Single Terrace Categories and a Partial Double Terrace," Hughes Aircraft, Space and Communications Report 4132.15/2594, 25 January 1984.

8.59. D. F. Gluck and P. H. Young, "Performance and Optimization of an Axisymetric Thermal Doubler," *Proceedings, 1988 Summer Computer Simulation Conference* (Seattle, WA, 25–28 July 1988).

8.60. M. Ryals, technical brief: "Graphite Fiber Reinforced Al and Cu Alloys for Thermal Management Application," *Electronic Cooling* **5** (1), 42 (January 1999).

8.61. C. Zweben, "High Performance Thermal Management Materials," *Electronic Cooling* **5** (3), 36–42 (September 1999).

8.62. Carbon Base Heat Spreaders, On website: http://www.enertron-inc.com (2001).

8.63. Thermal Management Materials, On website: http://www.advceramics.com (2001).

8.64. M. Montesano. "Thermal Management for Advance 3D Packaging of Payload Electronics," *11th Spacecraft Thermal Control Technology Workshop*, The Aerospace Corporation (El Segundo, CA, 1–3 March 2000).

8.65. V. Baturkin, K. Shkoda, N. Gudkova, *et al.*, "Study of Thermal Performance of Isothermal Electronic Plate with Regulated Temperature," In *Digest: Design and Technology of Manufacture of Space Apparatus* (Nauka Publisher, Moscow, 1988), pp. 92–105.

8.66. Integrated Plate Heat Pipe. Technical note by Showa Aluminum Corp., Japan, 1999.

8.67. V. Baturkin, S. Zhuik, N. Grechina, *et al.*, Rep. No. 961603, "Working out of Heat Pipes for Low Temperature Radiative Cooling Systems for Space Optic Sensors," *Proc. of 26th International Conference on Environmental Systems* (Monterey, CA, 8–11 July 1996).

8.68. W. C. Layton, "Traveling Wave Tube Thermal/Structural Study," Report No. TOR-0088(9975)-1, The Aerospace Corporation, 1 August 1988.

8.69. E. H. Goit, "Third Degree Integration Formulas with Four Points in Two Dimensions," M. S. thesis, State University of New York at Buffalo, February 1969.

8.70. J. W. Welch and B. T. Hamada, "Calculation of Heat Transfer Coefficients Across an Electronic Box Bare Interface Using a Finite Element Approach," presented at *26th Int. Conf. on Envir. Sys.* (Monterey, CA, July 1996).

8.71. S. Bogdanov, O. Ivanov, A. Kuprianova, "Material Properties," in *Refrigeration Engineering Handbook*, 3rd ed. (Agropromizdat, Moscow, 1985), p. 208.

8.72. *Satellite Thermal Control Handbook*, 1st ed., edited by D. G. Gilmore (The Aerospace Press, El Segundo, California, 1994).

8.73. L. Novitskiy and I. Kozhevnikov, *Thermal Properties of Materials at Low Temperatures Handbook* (Mashinostroenie, Moscow, 1975) 216 pages.

8.74. K. Buesking and B. Sullivan (MSNW, Inc.) "Composite Properties for Thermal-Structural Materials Solutions for Spacecraft," Prepared for Lockheed-Martin Missiles and Space Division, Feb. 1996.

8.75. G. Avanesov, Y. Ziman, V. Tarnopolsky, *et al.*, TV Survey of Comet Halley (Nauka, Moscow, 1989).

8.76. V. M. Baturkin and N. K. Gretchina, "Investigation of Thermocontrol Behavior of the Cooling System Based on Heat Pipes with Thermodiode Properties," Report N 922-Uk-89, 31.03, Deposited in Ukrainian Scientific Information Institute, Kyiv (1989).

8.77. I. Walter, F. Schrandt, and U. Grote, "Konstruktion und Technologie eines Optoelektronischen Weitwinkelscanners fur den Tiefraumeinsatz – WAOSS," Report Jt98_117 in Jahrbuch der Deutschen Gesellschaft für Luft- und Raumfahrt (Lilienthal-Oberth e.V., DGLR, 1998).

8.78. G. Neucum, R. Jaumann, H. Hoffmann, *et al.*, "A High Resolution Space Camera (HRSC) for Earth Observation in Regional Scales," *Proceedings of ESA Symposium on Space Station Utilization*, SP-385 (Darmstadt, Germany, December 1996), pp. 609–614.

8.79. M. de Sorga, "Thermal Interface Materials," *Electronic Cooling* **2** (3) (September 1996).

8.80. Sil-Pad Design Guide, Rev.030397, The Bergquest Company, 1997–1998.

8.81. C. L. Seaman and T. R. Knowles, "Carbon Velvet Thermal Interface Gaskets," Paper AIAA-2001-0217, presented at the *AIAA Aerospace Sciences Meeting* (Reno, NV, 8–11 January 2001).

8.82. *Spacecraft System Engineering*, P. Fortescue and J. Stark, eds. (John Wiley & Sons Ltd., 1995), p. 242.

8.83. Technical information on http://www.ensinger-online.com, 2001.

8.84. ASM Committee, "High-Strength Medium-Temperature Thermoset Matrix Composite," in *Composites, Engineered Materials Handbook*, Vol. 1 (ASM International, Metals Park, OH, 1987), pp. 399-415.

8.85. V. M. Baturkin, N. K. Grechina, V. I. Kostenko, *et al.*, "Cryogenic System for the Videospectrometric Complex (VSC) Cooling in Project 'FOBOS'," Paper Pr-1409 presented at Space Research Institute AS USSR, 1988.

8.86. Anon., "Weitwinkel Stereoscanner WAOSS fur die Mission Mars 96," Deutsche Hochschulschriften 1146, Deutsches Zentrum fur Luft- und Raumfahrt e.V., 1998, pp. 222–223.

8.87. G. Neukum, U. Carsenty, K. Eichentopf, *et al.*, "The Experiments HRSC and WAOSS on the Russian MARS 94/96 Missions," *Acta Astronautica* **38** (9), 713–720 (1996).

8.88. A. Zaglauer, W. Pitz, "Champ—the First Flexbus in Orbit," Digest of the 3rd Int. Symposium (Small Satellite for Earth Observation) of the Int. Academy of Astronautics, Berlin, 2–6 April 2001, edited by H. P. Roser, R. Sandau, A. Valenzuella (Wissenschaft und Technic Verl., Berlin, 2001) pp.105–109.

8.89. M. Rhoads and W. Moses, "Thermal Contact Conductance between Aligned Unidirectional Carbon/Epoxy Resin Composites," Paper AIAA 90-0540, presented at the *28th Aerospace Sciences Meeting* (January 1990).

8.90. S. R. Mirmira, M. C. Jackson, and L. S. Fletcher, "Effective Thermal Conductivity and Thermal Contact Conductance of Graphite Fiber Composites," *J. Thermophysics* **15** (1), 18–26 (2001).

8.91. S. R. Mirmira and L. S. Fletcher, "Comparison of Effective Thermal Conductivity and Contact Conductance of Fibrous Composites," *J. Thermophysics* **13** (2), 272–276 (1999).

8.92. E. E. Marotta and L. S. Fletcher, "Thermal Contact Conductance of Selected Polymeric Materials," *J. Thermophysics* **10** (2), 334–342 (1996).

8.93. M. A. Lambert and L. S. Fletcher, "Experimental Thermal Contact Conductance of Continuous Fiber Metal Matrix Composites," Paper AIAA 94-0122, presented at the *32nd Aerospace Sciences Meeting* (January 1994).

8.94. M. Yovanovich, "Analytical and Experimental Investigation on the Thermal Resistance of Angular Contact Instrument Bearings," Report No. E-2215, MIT Instrumentation Laboratory, December 1967.

8.95. H. J. Deacon, "Thermal Conductance of ASAT Bearing," The Aerospace Corporation, ATM 87(2426-02)-3, 20 November 1986.

8.96. K. T. Stevens and M. J. Todd, "Thermal Conductance Across Ball Bearings in Vacuum," European Space Tribology Laboratory, Report No. ESA (ESTL), 25 February 1977.

8.97. V. Popov, *Heat Exchange in Zone of Contact of Split and Nondetachable Connections* (ENERGIYA, Moscow, 1971).

8.98. Y. Shlykov, E. Ganin, and S. Zarevsky, *Contact Thermal Resistance* (ENERGIYA, Moscow, 1977).